

# Four-Fermi Theories

## On The Lattice And In The Continuum



**FRIEDRICH-SCHILLER-  
UNIVERSITÄT  
JENA**

Dissertation zur Erlangung des akademischen Grades  
*doctor rerum naturalis (Dr. rer. nat.)*

vorgelegt dem Rat der  
Physikalisch-Astronomischen Fakultät  
der Friedrich-Schiller-Universität Jena

von **M.Sc. Julian Johannes Lenz**  
geboren am 30. Juli 1994 in Elmshorn

**Gutachter:**

1. Prof. Dr. Andreas Wipf (Friedrich-Schiller Universität Jena)
2. Prof. Dr. Urs Wenger (Universität Bern)
3. Prof. Dr. Simon Hands (University of Liverpool)

**Tag der Disputation:** 14.05.2024



# Abstract

In this thesis, we study properties of four-FERMI theories (4FTs) in low-dimensional EUCLIDEAN spacetimes. Such models are often employed as effective theories or toy models to study phenomena from particle physics and condensed-matter systems and they are distinguished by their symmetries and interacting degrees of freedom (DOFs).

Concretely, we focus on 1+1D GROSS-NEVEU (GN) models which share certain properties, such as asymptotic freedom and some form of chiral symmetry, with quantum chromodynamics (QCD). As such they can serve as a testbed to discuss questions that cannot be answered in full QCD and we do so by investigating spontaneous breakdown of translational invariance at finite density which has been conjectured to be a feature of the QCD phase diagram (PD). From a condensed-matter perspective, similar theories are, e.g., of interest for the description of polymer chains.

We present strong evidence in favor of the theoretical predictions of quasi-long-range order in these models. Our study reveals a number of similarities with mean-field (MF) phenomena, in which however pertinent no-go theorems can be circumvented and inhomogeneous condensates are found. As such quantum-spin liquid (QSL) behavior is conjectured to be a general phenomenon when dealing with spontaneous breakdown of translational invariance, these insights could prepare for investigations of more realistic models up to QCD itself.

At the end of this thesis, we turn to 1+2D THIRRING (TH) models at small flavor numbers, models that have served as a starting point for many conceptual and technical advances. They are often studied for their close relation to quantum electrodynamics.

We provide multiple evidence that there is no spontaneous symmetry breaking (SSB) of chiral symmetry in these models formulated with SLAC fermions. Instead, we find hints on a new exotic phase transition (PT) that seems to be unrelated to any form of symmetry breaking. While other modern methods agree on the general trend, the fate of the single-flavor reducible model is still disputed in the literature and numerous open questions with their possible answers are discussed.

# Zusammenfassung

In der vorliegenden Dissertationsschrift werden verschiedene Eigenschaften von vier-FERMI-Theorien in niederdimensionalen EUKLIDISCHEN Raumzeiten diskutiert. Solche Modelle werden oftmals als effektive Theorien oder Spielzeugmodelle verwendet, um Phänomene aus der Teilchen- und Festkörperphysik zu studieren. Sie werden anhand ihrer Symmetrien und wechselwirkenden Freiheitsgrade unterschieden.

Konkret fokussieren wir uns auf 1+1-dimensionale GROSS-NEVEU-Modelle (GN), welche gewisse Eigenschaften, wie z. B. asymptotische Freiheit und chirale Symmetrie, mit der Quantenchromodynamik (QCD) teilen. In diesem Sinne können sie dazu verwendet werden, Fragen zu diskutieren, die derzeit in voller Quantenchromodynamik nicht beantwortet werden können. Dies werden wir in Form einer Untersuchung von spontaner Brechung der Translationsinvarianz bei endlicher Dichte tun. Es gibt Mutmaßungen, dass diese im Phasendiagramm der QCD vorkommen könnte. Aus der Perspektive der Festkörperphysik können diese und ähnliche Theorien z. B. Polymerketten beschreiben.

Wir präsentieren starke Indizien, die die theoretische Vorhersage von quasi-langreichweitiger Ordnung stützen. Unsere Untersuchungen haben dabei eine Reihe von Ähnlichkeiten mit der Molekularfeldnäherung zutage gefördert, wobei letztere allerdings einschlägige No-Go-Theoreme umgehen und echte inhomogene Kondensate erzeugen kann. Kürzlich publizierte Argumente, dass dieses sogenannte Quantenspinflüssigkeitsverhalten universell anstelle von spontaner Brechung der Translationsinvarianz auftreten könnte, eröffnen die Möglichkeit, dass unsere Erkenntnisse die in realistischeren Modellen bis hin zu QCD zu erwartenden Phänomene gut widerspiegeln.

Am Ende dieser Dissertationsschrift wenden wir uns den 1+2-dimensionalen THIRRING-Modellen (TH) bei kleinen Flavorzahlen zu; Modelle, welche bereits vielfach Ausgangspunkt von konzeptionellen und technischen Fortschritten waren und häufig aufgrund ihrer Nähe zur Quantenelektrodynamik studiert werden.

Unsere Studien liefern vielfache Hinweise, dass es in der Formulierung dieser Theorie mit SLAC-Fermionen niemals zu spontaner Brechung der chiralen Symmetrie kommt. Stattdessen deutet sich ein neuer exotischer Phasenübergang an, der mit keiner Symmetriebrechung in Verbindung zu stehen scheint. Während sich moderne Methoden in der allgemeinen Tendenz durchaus einig sind, ist gerade das Schicksal des reduzierbaren Ein-Flavor-Modells in der Literatur noch umstritten und die offenen Fragen werden mit ihren möglichen Antworten diskutiert.

# Conventions and Symbols

This preamble summarizes conventions and provides a reference for the symbols used throughout this thesis. They apply if not stated otherwise in the main text. A glossary for the abbreviations can be found at the end of the text.

**Mathematics:** We use EINSTEIN’S SUM CONVENTION without special meaning of the position (upper or lower) of an index because in EUCLIDEAN spacetime the metric is  $\delta_{\mu\nu}$ . For example,  $a^\mu b^\mu c_\nu = \sum_\mu a^\mu b^\mu c_\nu$ . We work in natural units where  $\hbar = c = k_B = 1$ .

**Statistics:** Monte Carlo (MC) ensembles are analyzed using a binned jackknife approach [1] in which autocorrelations (ACs) are accounted for by a manually chosen bin size that well includes the AC time (ACT). The latter is usually analyzed in detail for representative parameters either by fits to AC functions (ACFs) or by the use of approximation formulae [1], if sufficient statistics are available, and otherwise estimated by manual inspection of MC timelines. Statistical uncertainties are given as one- $\sigma$  intervals, i.e. we are about 68% sure that the given errorbars, etc., include the correct value. Without further knowledge, we assume that all statistical distributions are normal distributions. In case of fitting some model to our data, we use the least-squares method provided by `scipy`’s function `optimize.curve_fit` [2] taking into account the statistical uncertainties, if available, and estimate the confidence intervals by sampling the model’s prediction with randomly drawn normal-distributed parameters according to their covariance matrix. For fitted parameter values, we report their standard deviation as uncertainties. This might underestimate their true uncertainties in cases where the underlying statistics do not allow for high-precision inference and we will make sure to correct for that by hand in final results, if necessary.

**Plots:** Plots will include transparent lines connecting the data points in order to guide the eye, emphasize trends and distinguish different data sets. They are not meant as interpolations or the like unless explicitly stated. Fits always include a shaded region showing the 68% confidence interval as described above. This region might be invisibly small. Phase diagrams will usually be color-encoded scatter plots. Color mappings must necessarily include reasonable choices to illustrate the qualitatively different regions of such phase diagrams, in particular thresholds when noisy zero values are to be distinguished. These choices are made in all conscience with the intent to accurately and faithfully present the data, but they are *arbitrary*! In such cases, the precise location of a color transition cannot be given any meaning and only qualitative claims can be made. These cases are clearly labeled as such in the corresponding captions.

**Quantum fields**

- $\psi$  Fermion field  
 $\bar{\psi}$  Anti-Fermion field  
 $\Delta$  Complex scalar field, see Eq. (2.32)  
 $\sigma$  Real (pseudo)scalar field, see Eq. (2.27)  
 $\pi$  Real pseudoscalar field, see Eq. (2.33)  
 $\rho$  Absolute value field of  $\Delta$   
 $\theta$  Complex phase field of  $\Delta$   
 $J$  Fermionic current, see Eq. (2.20)

**Lattice parameters**

- $a$  Lattice spacing  
 $L$  Linear lattice size in physical units  
 $d$  Spacetime dimension  
 $\Lambda$  Spacetime lattice  
 $\Lambda_s$  Spatial lattice  
 $N_s, N_t$  Number of spatial/temporal points  
 $t, x, y, \dots$  Spacetime coordinates  
 $\mu, \nu, \xi, \dots$  Spacetime indices

**Mathematics and Symmetries**

- $\mathbb{C}$  Complex numbers  
 $\mathbb{N}$  Natural numbers  
 $\mathbb{R}$  Real numbers  
 $\mathbb{Z}$  Integers  
 $\mathcal{C}$  Charge conjugation operator  
 $\mathbb{Z}_2^{\mathcal{C}}$  Charge conjugation group  
 $\mathcal{P}$  Parity transformation operator  
 $\mathbb{Z}_2^{\mathcal{P}}$  Parity group  
 $\mathcal{T}$  Time reversal operator  
 $\mathbb{Z}_2^{\mathcal{T}}$  Time reversal group  
 $\not{D}$  Free DIRAC operator, see below Eq. (2.6)  
 $e$  EULER'S number  $e = 271828 \dots$   
 $\gamma$  EULER-MASCHERONI constant  
 $\tau$  Generators of  $SU(N_f)$   
 $\gamma^\mu$   $\gamma$ -matrices  
 $\gamma_*$  Generalization of  $\gamma_5$  to arbitrary  $d$   
 $\mathbb{1}$  Identity matrix  
 $\mathcal{D}$  Functional integral measure

- $O(N)$  Orthogonal group  
 $\mathcal{O}$  Order of magnitude or big- $O$  notation  
 $\sigma_i$  Pauli matrices including  $\sigma_0 = \mathbb{1}$   
 $U(N)$  Unitary group

**Observables**

- $\Sigma$  Chiral condensate  $\Sigma = \langle \bar{\psi}\psi \rangle$   
 $n_B$  Baryon density  
 $C$  Spatial correlator, see Eq. (6.1)  
 $C_{\text{long}}$  Order parameter, see Eq. (6.5)  
 $C_{n_B}$  Spatial  $n_B - \sigma^2$  correlator, see Eq. (6.2)  
 $C_{\text{short}}$  Order parameter, see Eq. (6.4)  
 $k_{\text{max}}$  Dominant wave number, see Eq. (6.3)  
 $\lambda_{\chi S}$  Wavelength of chiral spirals, see Eq. (3.7)  
 $\xi_\beta$  Thermal correlation length, see Eq. (3.14)

**Parameters**

- $g_{\chi\text{GN}}^2$   $\chi$ GN coupling  
 $g_{\text{NJL}}^2$  NJL coupling  
 $g_{\mathbb{Z}_2\text{-GN}}^2$   $\mathbb{Z}_2$ -GN coupling  
 $g_{\text{TH}}^2$  TH coupling  
 $g_{\text{TH,LAP}}^2$  TH coupling at LAP transition  
 $g_{\text{TH,t}}^2$  TH coupling at triple point  
 $D$  Full DIRAC operator, see Eq. (2.26), ...  
 $m$  Mass  
 $\mu$  Chemical potential  
 $\mu_c$  Critical chemical potential  
 $\mu_t$  Chemical potential at the triple point  
 $N_f$  Number of irreducible flavors  
 $a, b, \dots$  Flavor indices  
 $N_r$  Number of reducible flavors in 1+2D  
 $N_{r,c}$  Critical (reducible) flavor number  
 $N_{r,t}$  Triple point (reducible) flavor number  
 $N_{\text{spin}}$  Number of spinor components  
 $\rho_0$   $\chi$ GN scale parameter, see Eq. (4.11)  
 $\sigma_0$   $\mathbb{Z}_2$ -GN scale parameter, see Eq. (4.10)  
 $T$  Temperature  
 $T_c$  Critical temperature  
 $\beta$  Inverse temperature  $\beta = \frac{1}{k_B T}$   
 $T_t$  Triple point temperature

# Contents

<b>Conventions and Symbols</b>	<b>vi</b>
<b>1 Introduction</b>	<b>1</b>
<b>2 Four-FERMI Theories in the Continuum</b>	<b>5</b>
2.1 Excerpts From Quantum Field Theory . . . . .	5
2.2 Free Fermions . . . . .	6
2.3 Symmetries . . . . .	7
2.4 EUCLIDEAN and Flavor Bilinears and FIERZ Transformations . . . . .	10
2.5 Reducible Representations of the CLIFFORD Algebra . . . . .	11
2.6 Four-FERMI Theories . . . . .	12
2.7 External Parameters . . . . .	17
<b>3 Analytical Precursors</b>	<b>19</b>
3.1 Mean-Field Results in GROSS-NEVEU-like Models . . . . .	19
3.1.1 Homogeneous GROSS-NEVEU-like Phase Diagrams . . . . .	20
3.1.2 Inhomogeneities in Chiral GROSS-NEVEU Models . . . . .	21
3.1.3 Inhomogeneities in Discrete GROSS-NEVEU Models . . . . .	22
3.2 Inhomogeneities in (Closer-To) Real-World Systems . . . . .	23
3.3 Beyond Mean Field and No-Go Theorems . . . . .	25
3.4 Applicability and Quantum-Spin-Liquid Conjecture . . . . .	28
<b>4 Lattice Quantum Field Theory</b>	<b>29</b>
4.1 Lattice Quantum Field Theory and Monte Carlo Techniques . . . . .	29
4.2 The Lattice Artifact Phase . . . . .	32
4.3 Notation . . . . .	33
4.4 Scalesetting . . . . .	33
<b>5 The DIRAC Operator and its Discretizations</b>	<b>35</b>
5.1 Properties of the Continuum DIRAC Operator . . . . .	35
5.2 Ultralocal Discretizations . . . . .	36
5.3 Nonlocal Discretizations . . . . .	38
5.4 Local Discretizations . . . . .	39

5.5	Chemical Potential on the Lattice . . . . .	40
5.6	The Sign Problem . . . . .	40
<b>6</b>	<b>GROSS-NEVEU Models in 1+1 Dimensions</b>	<b>43</b>
6.1	Technical Overview . . . . .	43
6.1.1	Observables . . . . .	43
6.1.2	Further Stumbling Blocks . . . . .	45
6.2	Chiral GROSS-NEVEU Models . . . . .	46
6.2.1	The Finite-Volume Phase Diagram for Two Flavors . . . . .	47
6.2.2	$C_{\text{short}}$ and the Competition of Scales . . . . .	49
6.2.3	Physical Limits . . . . .	53
6.2.4	Temporal Correlators . . . . .	55
6.2.5	Notes on Eight Flavors . . . . .	57
6.3	Discrete GROSS-NEVEU Models . . . . .	57
6.3.1	The Finite-Volume Phase Diagram for Eight Flavors . . . . .	58
6.3.2	Baryonic Liquids . . . . .	60
6.3.3	A Detailed Study of the Infrared Behavior . . . . .	62
<b>7</b>	<b>THIRRING Models in 1+2 Dimensions</b>	<b>67</b>
7.1	Precursors About Other Flavor Numbers . . . . .	67
7.2	Absence of Chiral Symmetry Breaking . . . . .	70
7.2.1	The Chiral Condensate . . . . .	70
7.2.2	Spectral Investigations for $N_r = 0.80$ and $N_r = 1.00$ . . . . .	73
7.3	The New Phase Transition . . . . .	75
7.4	The Phase Diagram . . . . .	78
7.5	On the Discrepancies of Modern Lattice Approaches . . . . .	80
<b>8</b>	<b>Conclusions</b>	<b>83</b>
<b>A</b>	<b>Numerical Differentiation</b>	<b>89</b>
<b>B</b>	<b>Parameters and Ensembles</b>	<b>91</b>
B.1	Chiral GROSS-NEVEU Models . . . . .	91
B.2	Discrete GROSS-NEVEU Models . . . . .	94
B.3	THIRRING Models . . . . .	96
<b>C</b>	<b>Data Availability Statement and Technical Acknowledgements</b>	<b>99</b>
	<b>Acronyms</b>	<b>101</b>
	<b>List of Figures and List of Tables</b>	<b>102</b>
	<b>Bibliography</b>	<b>106</b>



# Chapter 1

## Introduction

Physicists strive to describe the world by its most fundamental principles – and they are very successful in that respect: Despite the fact that we are not yet able to unify the fundamental concepts of general relativity and quantum theory, either one is capable of predictions of astounding precision in their respective range of applicability, i.e., for astronomically large and microscopically small scales, respectively.

Unfortunately, on scales much more relevant to our daily experience both theories are way too complicated to be applied successfully due to a phenomenon called *emergence*. It basically says that the relevant degrees of freedom (DOFs) on one scale of interest might be very different from our description of the same system on a different scale. They *emerge* from a microscopic description without being apparent in the latter.

One of its consequences is that very different physical systems can have very similar descriptions *on a certain scale of interest*. Four-FERMI theories (4FTs) are one such description being equally applicable to many condensed matter systems, e.g., the famous graphene, and particle physics scenarios, most prominently quantum chromodynamics (QCD) but also the electroweak sector. In both use cases, we (nowadays) know that 4FTs are not a description of the microscopic DOFs but instead yield results in a low-energy regime where one can describe, e.g., conductance and magnetism of solids [3, 4] or the  $\beta$ -decay [5] and the equilibrium properties of neutron stars [6].

As early as 1933, FERMI invented an ad-hoc description of the  $\beta$ -decay which can be seen as the first instance of a 4FT [7]. Even though, it was later replaced by the gauge theory of electroweak interactions, it was highly successful and influential at that time. He was followed by THIRRING in 1958 who studied the famous 1+1D single-flavor THIRRING (TH) model with its conformal symmetry as an instance of a completely solvable quantum field theory (QFT) [8]. At around the same time (1961), NAMBU and JONA-LASINIO (NJL) used a similar formulation [9, 10] in 1+3 dimensions to describe nucleons and mesons in analogy to the recently discovered BARDEEN-COOPER-SCHRIEFFER (BCS) mechanism of superconductivity [11]. While its original idea is concerned with an electron-phonon interaction, the latter is effectively described as a 4FT.

This last instance not only shows the parallel evolution of 4FTs in particle and condensed matter physics but at the same time beautifully illustrates their cross-fertilization. Unfortunately, this cross-fertilization did not always happen that promptly in later times: For example, the phase diagram of the HUBBARD model [12] – a tight-binding approximation for valence electrons hopping on a crystal lattice – and its lower-dimensional companions [13] has been known for a long time to exhibit interesting regions of spatially modulated order parameters known as LARKIN-OVCHINNIKOV-FULDE-FERRELL (LOFF) phases [14, 15]. The corresponding discovery in GROSS-NEVEU (GN) models – their continuum counterparts – was made as late as the early 2000s [16–18]. That is despite the fact that the invention of GN models as examples of dynamical symmetry breaking [19] succeeded the HUBBARD model by only ten years.

In more recent times, 4FTs are studied systematically as effective theories in particle physics [6, 20–23], tight-binding models in condensed matter theory [3, 4, 24–28] and generally as a testbed for conceptual and technical advances [29, 30]. Beyond the traditional TH, NJL and GN interactions (and their combinations) more exotic formulations are continuously developed, ranging from more involved couplings between the different copies of fermions [31–34], coupling to dynamical and static gauge fields [35–38] and higher-dimensional fermion representations [39, 40].

The most common way of analyzing 4FTs is by means of mean-field (MF) theory which becomes exact in the limit of an infinite number  $N_f$  of identical fermion copies. We will call these copies *flavors* although – depending on the context – they could also be thought of as color DOFs in QCD or even spin components in solid-state physics. The predictions of MF theory yield a first intuition for the system’s behavior but on various occasions [37, 41–43] the MF approximation turns out to show partly or fully different physics from the full quantum theory at realistically small flavor numbers  $N_f$ . These changes might be accounted for by a perturbative analysis around the MF solution (as is, for example, successfully done in [44]) but more often fully non-perturbative methods are needed.

Successful non-perturbative methods beyond MF include the functional renormalization group (FRG) [30, 45–50], various tensor network (TN) methods [51–53] and Monte Carlo (MC) simulations, the latter of which will be the main tool in this thesis. The MC method approximates the partition function of a system by an average over a finite number of sampled configurations generated by a computer. In order to do so, the system must be broken down to a finite number of DOFs, most commonly by discretizing the theory on a finite spacetime lattice. A notion of "importance" of a configuration is then defined from the functional integral measure in a stochastic sense. This necessitates the measure to be real and positive – a condition that on failure entails the infamous sign problem (SP), more precisely called *complex action problem*. The SP is probably one of the most notorious problem in modern high-energy physics and the only hindrance for first-principles simulations of QCD at finite density. As it is NP-hard [54], there is little hope for a generic solution but a highly active community is concerned with its elevation for specific (classes of) models [55–57].

Concretely, this thesis applies the above method to a number of (conjectured) instances of

spontaneous symmetry breaking (SSB). Symmetries themselves are a notion of utmost importance for statistical physics and QFT as they allow to categorize theories and particle spectra, constrain the form of fundamental equations and simplify computations. According to NOETHER’S theorem, continuous symmetries even lead to conserved quantities [58]. Their spontaneous breakdown – i.e. the realization of a ground state or equilibrium which does not respect such symmetries – again entails important consequences like dynamical mass generation and the existence of massless modes, known as NAMBU-GOLDSTONE bosons (NGBs) [59–61].

While from a particle physics point of view the chiral symmetry is of main interest, odd dimensions lack a notion of chirality and fermionic systems instead tend to break parity invariance. Only in a reducible fermion representation, obtained from pairing two irreducible fermion species from inequivalent representations, chirality can be studied. I will show examples of chiral symmetry breaking ( $\chi$ SB) in 1+1D GN models (in MF) and discuss its absence for 1+2D TH models. Instead spontaneous parity breaking can be observed in such systems. Additionally, fueled by conjectures from 1+3D [6, 62] and analytical findings in 1+1D [16, 17] a large part of this thesis will focus on the possibility of a combined breakdown of chiral and translational invariance.

This thesis is organized as follows: I will first discuss 4FTs in the continuum in Chapter 2 including their symmetries and fundamental properties. I will then in Chapter 3 review the analytical precursors to the later numerical studies. A number of results motivating or complementing this thesis will be reviewed and important no-go theorems established. Chapter 4 focuses on general techniques used in this thesis, followed by a dedicated Chapter 5 for a careful study of DIRAC operators and their discretizations. Turning to the numerical results of this thesis, I will start with 1+1D GN models in Chapter 6. After a more focused discussion of model-specific technical aspects in Section 6.1, I will discuss the somewhat easier chiral GROSS-NEVEU ( $\chi$ GN) case in Section 6.2 before turning to discrete GROSS-NEVEU ( $\mathbb{Z}_2$ -GN) models in Section 6.3. Finally, I will discuss 1+2D TH models in Chapter 7 and conclude in Chapter 8.

Appendix A contains some technical details around numerical differentiation which was used in Chapter 7. In Appendix B an overview of the generated ensembles and some technical parameters is provided. The analysis and visualization code for this thesis containing references to corresponding data releases is publicly available under [63] but for reference and acknowledgment, Appendix C summarizes the software used.

The results that I compiled in this thesis have been published in [42, 43, 64–69]. But I will not present exactly reproduced results in this thesis. I will present a reanalysis of the data that was at some points slightly refined due to the larger experience and broader perspective I can bring into the projects in retrospection.<sup>1</sup> That is why the reader might find slightly different numbers or minor reinterpretations of the results compared to [42, 43, 64–69]. Of course, the main results stay untouched. The results of further research during my doctoral studies are not part of this thesis but are published in [37, 38].

---

<sup>1</sup>For crosschecking, I was able to exactly reproduce all the results.



# Chapter 2

## Four-FERMI Theories in the Continuum

The current state-of-the-art description of the microscopic properties of our universe uses the language of QFT and matter is then described by fermionic DOFs. This chapter will start off by summarizing the relevant aspects of QFT (Section 2.1) quickly narrowing down to fermions (Section 2.2) and their symmetries (Section 2.3). The chapter culminates in a list of interacting fermionic theories in Section 2.6 that are – directly or indirectly – relevant to this thesis but does so only after establishing some notation and facts around fermionic bilinears (Section 2.4) and reducible representations (Section 2.5). This chapter is rounded off by a short mentioning and discussion of external parameters in Section 2.7 the influence of which on above 4FTs will be studied in this thesis. This part can be found in any pertinent textbook and the presentation is mostly guided by the exhaustive review in [70].

### 2.1 Excerpts From Quantum Field Theory

In our everyday experience, the behavior of physical objects is governed by a single deterministic behavior that is distinguished by being an extremum of the action of the system. Quantum theory, then, broadens the perspective understanding this as a limiting case of considering *all possible realizations* in a weighted manner. In EUCLIDEAN field theory describing the ground-state and thermodynamic equilibrium properties of quantum systems, the partition function and expectation values of observables  $\mathcal{X}$  are realized as a weighted average:

$$Z = \int \mathcal{D}\phi e^{-S[\phi]}, \quad \langle \mathcal{X} \rangle = \frac{1}{Z} \int \mathcal{D}\phi \mathcal{X}[\phi] e^{-S[\phi]}. \quad (2.1)$$

In these equations,  $\phi$  represents a collection of all DOFs (to be specified later on) that are averaged over according to the respective EUCLIDEAN action  $S$  of each concrete realization of  $\phi$ . All equilibrium properties of the system can now be inferred from (derivatives of) the partition function  $Z$ .

The number of DOFs is often infinite, e.g., when  $\phi$  describes fields that are defined in continuous or infinite spacetimes, rendering the above integral infinite-dimensional. In such cases,

Eq. (2.1) is meant to convey a physical idea, the mathematical implementation of which is a delicate issue involving some form of *regularization* and *renormalization*.

A convenient scheme of regularization is approximating the continuum spacetime by a finite spacetime lattice such that  $\phi$  is defined on finitely many points in spacetime. This idea is also the basis for many kinds of numerical treatment of such integrals and is devoted an own Chapter 4. Other approaches use cutoff functions in momentum space<sup>2</sup>, analytic continuation (in form of dimensional or  $\zeta$ -function regularization) or the addition of fictitious further systems counteracting divergences in the original one, known as PAULI-VILLARS regularization.

The procedures described above will change the result of the integral and, if it was necessary to introduce a regularization in the first place, naively removing it will again lead to divergences. This is tackled by renormalization. Renormalization refers to the process of redefining coupling constants in dependence of parameters of the regularization. In a properly renormalized expression, one can then undo the changes introduced by the regularization in a systematic manner in order to assign meaningful values to functional integrals like Eq. (2.1). These values will be independent of the regularization that was used.

## 2.2 Free Fermions

In  $d$ -dimensional spacetime, fermions (which we will usually denote as  $\psi$ ) are described by GRASSMANN-valued fields of multiple components. For fermions over the field of complex numbers  $\mathbb{C}$ , the BEREZIN integral over exponentiated bilinears yields

$$\int \mathcal{D}\psi \mathcal{D}\bar{\psi} e^{-\bar{\psi} D \psi} = \det D \quad (2.2)$$

where  $D$  is a linear operator and  $\bar{\psi} = \psi^\dagger$  is the EUCLIDEAN version of the DIRAC conjugate.<sup>3</sup>

In order to describe fermionic systems, we attach  $N_{\text{spin}}$  fermion components to each spacetime point and associate with such tuples the action of a representation of the CLIFFORD algebra  $\text{Cl}_d(\mathbb{C})$ , i.e. the algebra generated by  $d$  matrices  $\gamma_\mu$  obeying

$$\frac{1}{2} \{\gamma_\mu, \gamma_\nu\} = \delta_{\mu\nu} \mathbb{1}. \quad (2.3)$$

This relation implies that all EUCLIDEAN  $\gamma$ -matrices are HERMITIAN. Irreducible representations of the latter consist of  $2^{\lfloor \frac{d}{2} \rfloor}$  dimensional matrices. In even spacetime dimensions, all such representations are unitarily equivalent and there exists a non-trivial matrix

$$\gamma_* = -i^{\lfloor d/2 \rfloor} \gamma_0 \cdots \gamma_{d-1} \quad (2.4)$$

<sup>2</sup>Depending on their form, they can have effects similar to spacetime lattices.

<sup>3</sup>One should note the difference to the LORENTZIAN version  $\bar{\psi} = \psi^\dagger \gamma^0$ . We follow [70] while there are much more detailed discussions of that matter describing several possibilities [71].

anti-commuting with all  $\gamma$ -matrices and defining a notion of chirality via the chiral projectors

$$P_{\pm} = \frac{1}{2} (\mathbb{1} \pm \gamma_*) . \quad (2.5)$$

In odd dimensions, there exist two inequivalent representations related via  $\gamma_{\mu} \mapsto -\gamma_{\mu}$  and the would-be  $\gamma_* \propto \mathbb{1}$  is trivial. It follows that we cannot define a notion of chirality of irreducible fermions in odd-dimensional spacetimes.

From these building blocks, we can define the free fermion LAGRANGIAN

$$\mathcal{L} = \sum_{a=1}^{N_f} \bar{\psi}_a (\not{\partial} + m) \psi_a . \quad (2.6)$$

It includes the CLIFFORD structure in the abbreviation  $\not{\partial} = \gamma^{\mu} \partial_{\mu}$  and we further added a mass  $m$  coupling to  $\bar{\psi}\psi$  that will be discussed in Section 2.4. The formula implies a contraction over the spinor indices. We furthermore introduced  $N_f$  copies of identical fermions that we will call *flavors*. Their actual meaning depends on the real world system under consideration: In QCD they describe different flavors or colors depending on the context; in graphene, these are usually identified as the different spin components of the valence electrons; and so on.

## 2.3 Symmetries

Free fermions in equilibrium allow for a number of transformations of  $\psi, \bar{\psi}$  such that the action takes the same form with respect to the new variables. Such *symmetries* are important for a number of reasons, e.g., to organize the particle spectrum and simplify computations. In an attempt to model the equilibrium properties of relativistic QFTs, a careful analytic continuation from MINKOWSKI spacetime is in order and, particularly for fermions, this intricate issue was discussed a lot in the literature, e.g. [71–73]. This section closely follows the discussions in [69, 70] but includes some more details from [71].

**(Continuous) EUCLIDEAN Spacetime Symmetries.** Spacetime symmetries are one of the most fundamental concepts in QFT. They allow for a classification of DOFs into bosonic/fermionic<sup>4</sup> and (pseudo)scalar, (pseudo)vector, etc. They include rotations  $SO(d)$  and translations  $\mathbb{R}^d$ . The discrete subgroups of parity and time reversal will be discussed separately.

**Parity  $\mathbb{Z}_2^{\mathcal{P}}$ .** In even spacetime dimensions, parity is typically defined as a simultaneous sign flip of all spatial coordinates. It is, however, more convenient to define it as  $x^{\mu} \mapsto \mathcal{P}^{\mu}_{\nu} x^{\nu}$  where  $\mathcal{P}^{\mu}_{\nu} = \text{diag}(1, \dots, 1, -1)$  on the spacetime coordinates, i.e. flipping only the last component,

---

<sup>4</sup>or anyonic, depending on the dimension [74]

because this is a parity transformation in all spacetime dimensions. The fermions transform as

$$\psi(x^\mu) \mapsto \mathcal{P}\psi(\mathcal{P}^\mu{}_\nu x^\nu), \quad \bar{\psi}(x^\mu) \mapsto \alpha\bar{\psi}(\mathcal{P}^\mu{}_\nu x^\nu)\mathcal{P}^{-1} \quad (2.7)$$

for some yet-to-be-determined  $\alpha \in \mathbb{R}$  where  $\mathcal{P}$  (without EUCLIDEAN indices) is a matrix acting in spinor space (as opposed to  $\mathcal{P}^\mu{}_\nu$  acting on the spacetime coordinates). We will adopt this convention for the following paragraphs. For consistency, we need to ensure that

$$\mathcal{P}^{-1}\gamma^\mu\mathcal{P} = \alpha^{-1}\mathcal{P}^\mu{}_\nu\gamma^\nu. \quad (2.8)$$

By squaring this relation and using Eq. (2.3), we find  $\alpha^2 = 1$ . For  $\gamma_*$ , it follows that

$$\mathcal{P}^{-1}\gamma_*\mathcal{P} = -\alpha^d\gamma_*. \quad (2.9)$$

In even dimensions, we can choose  $\alpha = +1$  while in odd dimensions  $\alpha = -1$ .

The latter is reminiscent of the fact that, coming from the even-dimensional spacetime of dimension  $d - 1$ , we can construct an irreducible representation of the CLIFFORD algebra by reusing the same  $\gamma$ -matrices adding  $\gamma_{(d)}^{\mu=d-1} = \gamma_*^{(d-1)}$ . This directly entails that  $\mathcal{P} \propto \gamma_*^{(d-1)}$  inherits a lot of properties of the chiral structure from the spacetime of one spatial dimension less. It is also an intuitive picture that can explain why 1+2D irreducible mass terms and condensates break parity instead of chirality (see below).

**Charge Conjugation  $\mathbb{Z}_2^{\mathcal{C}}$ .** Charge conjugation  $\mathcal{C}$  maps

$$\psi \mapsto \mathcal{C}\bar{\psi}^\top, \quad \gamma^{\mu\top} = \eta\mathcal{C}^{-1}\gamma^\mu\mathcal{C}, \quad \eta \in \{\pm 1\}. \quad (2.10)$$

In even dimensions, both signs of  $\eta$  can be realized while in odd dimensions only one of them can be found in an alternating fashion, i.e.  $\eta = -1$  for  $1 + 4n$  dimensions and  $\eta = +1$  in  $3 + 4n$  dimensions,  $n \in \mathbb{N}_0$ . As can be seen, charge conjugation is intimately related to the complex structure of the GRASSMANN algebra the fermions live in. It is important to note that this is not unique and that the complex structures compatible with EUCLIDEAN and LORENTZIAN spacetime symmetries are not the same [71]. We choose the above convention for simplicity as it is of minor importance for this thesis but one should be aware its behavior after analytic continuation to LORENTZIAN spacetime could look unfamiliar to the reader.

**Time reversal  $\mathbb{Z}_2^{\mathcal{T}}$ .** In EUCLIDEAN spacetimes, one might be tempted to discard the time reversal symmetry carelessly as "just a rotated parity transformation". However, time is still intimately related to the notion of particles and anti-particles which generally are to be distinguished for fermionic DOFs. The above intuition is therefore only correct up to an additional interchange of fermions and anti-fermions. In fact, this notion is known as  $\mathcal{CPT}$ -symmetry [75] where the charge conjugation exactly implements this additional swap.

Time reversal symmetry  $\mathcal{T}$  acts as  $x^\mu \mapsto \mathcal{T}^\mu{}_\nu x^\nu$  where  $\mathcal{T}^\mu{}_\nu = \text{diag}(-1, 1, \dots, 1)$ , i.e.  $(t, x) \mapsto (-t, x)$ , on the spacetime coordinates. The fermions transform as

$$\psi(x^\mu) \mapsto \mathcal{T} \bar{\psi}^\top(\mathcal{T}^\mu{}_\nu x^\nu), \quad \bar{\psi}(x^\mu) \mapsto \beta \psi^\top(\mathcal{T}^\mu{}_\nu x^\nu) \mathcal{T}^{-1}. \quad (2.11)$$

The coefficient  $\beta$  can be worked out from  $\mathcal{CPT}$ -symmetry and one finds  $\beta = -1$  in  $3 + 4n$  spacetime dimensions,  $n \in \mathbb{N}_0$ , and  $\beta = +1$  otherwise [71].

**Flavor-Vector Symmetry.** The  $N_f$  copies of fermions are treated identically in the free-fermion LAGRANGIAN from Eq. (2.6). We can therefore rotate them into each other via any  $U \in U(N_f)$

$$\psi_a \mapsto U_{ab} \psi_b, \quad \bar{\psi}_a \mapsto \bar{\psi}_b U_{ba}^\dagger \quad (2.12)$$

where  $U$  is trivial in spinor space.

**Flavor-Axial/Chiral Symmetry.** Whenever we can define a notion of chirality, the chiral components of free massless fermions can actually be rotated among each other independently. This full flavor-chiral symmetry  $U(N_f) \times U(N_f)$  consists of the flavor-vector part above and the flavor-axial part rotating chiral components oppositely. It is again implemented via a  $U \in U(N_f)$

$$\psi_a \mapsto U_{ab} \psi_b, \quad \bar{\psi}_a \mapsto \bar{\psi}_b U_{ba}^\dagger \quad (2.13)$$

where, however,  $U = \exp(i\gamma_* \otimes u)$  acts non-trivially in spinor space,  $u \in \mathfrak{su}(N_f)$ . A mass term or a condensation of  $\bar{\psi}\psi$  breaks this symmetry. An important subgroup of the axial transformations is the discrete  $\mathbb{Z}_2$

$$\psi_a \mapsto \gamma_* \psi_a, \quad \bar{\psi}_a \mapsto -\bar{\psi}_a \gamma_*. \quad (2.14)$$

**PAULI-GÜRSEY Symmetry.** The above symmetries are manifest and straightforward to recognize in the formulation Eq. (2.6). It turns out, however, that sometimes there is the significantly larger freedom of mixing particle and anti-particle for the chiral components separately. PAULI [76] and GÜRSEY [77] were the first to formulate this for four-component DIRAC spinors. The general transformation reads

$$\psi \mapsto \alpha \psi + \beta \gamma_* \mathcal{C} \bar{\psi}^\top, \quad |\alpha|^2 + |\beta|^2 = 1 \quad (2.15)$$

for each flavor and can be combined with the other internal and external symmetries. It becomes particularly transparent in 1+1D where one can find a chiral MAJORANA representation, namely

$$\gamma_0 = \sigma_2, \quad \gamma_1 = i\sigma_1, \quad (2.16)$$

which is capable of decoupling chiral components as well as particles from their anti-partners manifestly. In the kinetic term, the  $2N_f$  MAJORANA components denoted as  $\xi$

$$\psi_a = \frac{1}{\sqrt{2}} (\xi_{2a} + i\xi_{2a+1}) \quad (2.17)$$

rearrange into an  $O(2N_f)$  scalar under

$$\xi_a \mapsto O_{ab}\xi_b, \quad O \in O(2N_f) \quad (2.18)$$

which includes charge conjugation and flavor-vector transformations as subgroups.

## 2.4 EUCLIDEAN and Flavor Bilinears and FIERZ Transformations

The EUCLIDEAN spacetime symmetry dictates that only expressions with a well-defined transformation behavior under the  $SO(d)$  rotational symmetry can be physically meaningful. In the following, we will define and discuss flavor-singlet and -multiplet bilinears that have this property. They will be building blocks for interaction terms, interpolating operators, and condensates later on.

Some relevant EUCLIDEAN-singlet bilinears are

$$S(x) = (\bar{\psi}\psi)(x), \quad P(x) = (\bar{\psi}\gamma_*\psi)(x), \quad P_a(x) = (\bar{\psi}\gamma_*\tau_a\psi)(x) \quad (2.19)$$

where the latter two are, of course, only defined when a  $\gamma_*$  is available. In there,  $\tau_a$  denotes the generators of the  $SU(N_f)$  flavor-vector symmetry. In even dimensions,  $S$  is a (pseudo)scalar with respect to EUCLIDEAN (chiral) symmetry and  $P$  vice versa. Thus, an explicit term proportional to  $S$  ( $P$ ) or a respective condensate breaks chiral (parity) symmetry. The flavor-vector  $P_a$  is pseudoscalar with respect to EUCLIDEAN transformations. In odd dimensions, only  $S$  exists and it turns out to be pseudoscalar. This implies that the irreducible mass term  $m\bar{\psi}\psi$  or a respective condensate breaks parity invariance.

Analogously, EUCLIDEAN (pseudo)vectors can be defined as

$$J^\mu(x) = (\bar{\psi}\gamma^\mu\psi)(x), \quad \Pi^\mu(x) = (\bar{\psi}\gamma^\mu\gamma_*\psi)(x), \quad \Pi_a^\mu(x) = (\bar{\psi}\gamma^\mu\gamma_*\tau_a\psi)(x). \quad (2.20)$$

Whenever they can be defined,  $\Pi_{(a)}^\mu$  are again pseudovectors. In even dimensions, all of these are EUCLIDEAN-rotated under (single-flavor) chiral transformations and, thus, they do not break chiral symmetry if found in EUCLIDEAN-invariant contractions. In odd dimensions, only  $J^\mu$  is defined and it is a pseudovector.

Higher-order bilinears in EUCLIDEAN and flavor indices can be written down analogously but concerning the construction of fermion interactions, even at this point we have introduced some

redundancy<sup>5</sup>: FIERZ transformations exploit the completeness relations of the CLIFFORD algebra to rearrange expressions of the form<sup>6</sup>

$$(\bar{\psi}_a M \psi_b) (\bar{\psi}_c N \psi_d). \quad (2.21)$$

In fact, they can be used to transform all combinations of four-Fermi terms into EUCLIDEAN or flavor singlets at one's own discretion.

## 2.5 Reducible Representations of the CLIFFORD Algebra

Irreducible fermions in odd spacetime dimensions do not feature chirality and the corresponding symmetry. However, in many scenarios where odd-dimensional spacetimes are considered, irreducible fermions are not the natural choice. For example, in graphene – to a very good approximation a material of only two spatial dimensions – one can organize the low-energy electron modes into four-component DIRAC spinors despite the fact that irreducible representations in this dimension are two-dimensional. Also, when modeling the chiral properties of QCD or the electroweak sector by lower-dimensional models one is interested in exactly the chiral properties.

In such cases, the representation of the CLIFFORD algebra can be chosen reducible by combining two irreducible flavors from inequivalent irreducible representations into one reducible flavor with twice the number of DOFs. Given one irreducible odd-dimensional representation, this reducible representation can be constructed explicitly as

$$\gamma^\mu_{\text{red}} = \sigma_3 \otimes \gamma^\mu_{\text{irred}} \quad (2.22)$$

where  $\sigma_3$  acts on pairs of irreducible flavors in flavor space. It turns out that the generated algebra is exactly the same that one would get from the irreducible representation in one dimension higher by discarding one of the  $\gamma$ -matrices.

This immediately implies that it contains at least two matrices that would qualify as  $\gamma_*$ : either the discarded  $\gamma_*^{(d)} = \gamma_{(d+1)}^{\mu=d}$  or  $\gamma_{**}^{(d)} = \gamma_*^{(d+1)}$ . Both are valid choices and, additionally, their product yields another non-trivial matrix commuting with all  $\gamma$ -matrices. These three further matrices enlarge the flavor-chiral  $U(N_r) \times U(N_r)$  to a  $U(2N_r)$  extended chiral symmetry for reducible representations, where we have chosen  $N_r$  to denote the number of *reducible* flavors as opposed to  $N_f$  reserved for irreducible flavors.

This enlargement of the symmetry group can be understood from the perspective of the irreducible representations: The construction of each reducible flavor introduced two irreducible flavors,  $N_f = 2N_r$ . Thus, the flavor-vector symmetry alone is a  $U(N_f) = U(2N_r)$  symmetry. It was, however, slightly redefined into a staggered formulation to account for the alternation of inequivalent irreducible representations  $\pm\gamma^\mu$ .

---

<sup>5</sup>in the low dimensions we work in

<sup>6</sup> $M, N$  are appropriate matrices.

The two inequivalent irreducible representations behave exactly the same, so we can redefine

$$\psi \mapsto \gamma_* \gamma_{**} \psi, \quad \bar{\psi} \mapsto \bar{\psi} \quad (2.23)$$

to align their relative signs. This is necessary for the consistency of the theory<sup>7</sup> but affects fermionic bilinears. In particular, the reducible bilinear  $\bar{\psi}\psi$  translates into a flavor-staggered bilinear in the irreducible representations. In fact, the naive reducible mass matrix that one can write down is not proportional to the identity in *irreducible*-flavor space. That is why all parity-breaking contributions from the individual irreducible mass terms or condensates cancel between the flavors, leaving us with a flavor-vector breaking pattern (from the irreducible perspective) instead.

## 2.6 Four-FERMI Theories

From the bilinears discussed in the previous sections, one can systematically construct fermionic interaction terms. By power counting, one can expect that four-Fermi terms, i.e. terms of the form Eq. (2.21), are the most relevant<sup>8</sup> terms. One can further deduce that 1+1D 4FT are generally asymptotically free. In 1+2D, they are no longer perturbatively renormalizable but still asymptotically safe [45]. In higher dimensions, they are non-renormalizable but can nonetheless be of interest as effective theories as is discussed in Chapter 1 and Section 3.2.

The various possible interactions are typically constructed from symmetry considerations and the desired DOFs. The resulting models are then named after their inventors.<sup>9</sup> Some properties of the various models are summarized in Table 2.1.

**Discrete GROSS-NEVEU ( $\mathbb{Z}_2$ -GN) models.** The arguably simplest 4FTs are discrete GN models. In addition to the free-fermion LAGRANGIAN Eq. (2.6), they feature an interaction of the form

$$\mathcal{L}_{\mathbb{Z}_2\text{-GN}} = \frac{g_{\mathbb{Z}_2\text{-GN}}^2}{2N_f} S^2 \quad (2.24)$$

where  $g_{\mathbb{Z}_2\text{-GN}}^2$  is a real-valued coupling constant. In even dimensions,  $S \mapsto -S$  under discrete chiral transformations such that this theory generically features a discrete chiral symmetry while general chiral transformations lead to non-vanishing phase factors. In odd dimensions,  $S$  is pseudoscalar and parity takes over the role of discrete chiral symmetry. It was first described in [19] as an example of an asymptotically free theory of interacting fermions.

<sup>7</sup>Otherwise, EUCLIDEAN correlators could violate positivity constraints [64].

<sup>8</sup>in the renormalization-group sense

<sup>9</sup>This, however, does not yield a one-to-one mapping providing some room for arbitrary choices. We will use a naming scheme that associates a specific form of the interaction term with a model's name irrespective of dimensionality or representation as opposed to other conventions. Expert readers should therefore check if the following naming scheme matches their expectations.

**Table 2.1:** Summary of some 4FTs and their properties (inspired by a similar table in [70]).

		TH	$\mathbb{Z}_2$ -GN	$\chi$ GN
Interaction		$J_\mu J^\mu$	$S^2$	$S^2 - P^2$
Auxiliary Boson		$A^\mu$	$\sigma$	$\Delta = \rho e^{i\theta} = \sigma + i\pi$
1+1D	Symmetry	$O(2N_f) \times U(N_f)$	$O(2N_f) \times \mathbb{Z}_2$	$U(N_f) \times U(1)$
	$m$ breaks	axial $U(N_f)$	chiral $\mathbb{Z}_2$	axial $U(1)$
1+2D	Symmetry	$U(N_f) \times \mathbb{Z}_2^P$	$U(N_f) \times \mathbb{Z}_2^P$	-
	$m$ breaks	parity $\mathbb{Z}_2^P$	parity $\mathbb{Z}_2^P$	-
1+2D (red.)	Symmetry	$U(2N_f)$	$U(N_f) \times U(N_f) \times \mathbb{Z}_2$	$U(N_f) \times U(N_f) \times U(1)$
	$m$ breaks	axial $U(N_f)$	chiral $\mathbb{Z}_2$	axial $U(1)$

The fermionic interaction is conveniently handled by a HUBBARD-STRATONOVICH (HS) transformation that introduces an auxiliary bosonic DOF in order to remove the explicit four-fermion term. By this means, it can be shown that the partition function of GN models is proportional to partition functions of the following model<sup>10</sup>

$$\mathcal{L}_{\mathbb{Z}_2\text{-GN,HS}} = \bar{\psi} D[\sigma] \psi + \frac{N_f}{2g_{\mathbb{Z}_2\text{-GN}}^2} \sigma^2 \quad (2.25)$$

where

$$D[\sigma] = \not{\partial} + m + \sigma. \quad (2.26)$$

The equivalence follows from the equations of motion (EOMs) on the classical level but is directly lifted to the quantum level because  $\sigma$  appears at most quadratically in Eq. (2.25) and can, hence, be integrated out exactly. It turns out that DYSON-SCHWINGER equations (DSEs) can be used to assign a meaning to  $\sigma$  that goes beyond its original "auxiliary" character because

$$\langle \sigma \rangle = -\frac{g_{\mathbb{Z}_2\text{-GN}}^2}{N_f} \langle S \rangle. \quad (2.27)$$

It is, thus, an order parameter field for chiral (parity) SSB in even (odd) dimensions and transforms according to  $\sigma \mapsto -\sigma$  under the pertinent transformation. Higher-order DSEs relate higher-order expectation values of  $\sigma$  and  $S$  with each other such that, for example, correlators of  $\sigma$  are directly related to correlators of  $S$  representing a (pseudo)scalar meson in this setting.

<sup>10</sup>In the rest of the text we will not explicitly distinguish between 4FTs and their HS transformed counterparts. In particular, we will drop the HS subscript after its first appearance.

**Chiral Gross-Neveu ( $\chi$ GN) models.** A small modification of the  $\mathbb{Z}_2$ -GN interaction term allows one to study a larger continuous  $U(1)$  chiral symmetry,

$$\mathcal{L}_{\chi\text{GN}} = \frac{g_{\chi\text{GN}}^2}{2N_f} (S^2 - P^2). \quad (2.28)$$

This LAGRANGIAN was actually first discussed in [10, 78] but due to its close relation to  $\mathbb{Z}_2$ -GN models and the naming conflict with the next model, we will name it after [19] where it was studied in 1+1 dimensions first. It is invariant under the  $U(1)$  chiral symmetry of simultaneous phase rotations of all flavors due to an intricate cancellation of the transformation behaviors of  $S^2$  and  $P^2$  separately. It can be formulated FIERZ-equivalently as [10]

$$\mathcal{L}_{\chi\text{GN}} = -\frac{g_{\chi\text{GN}}^2}{4N_f} (J^\mu J^\mu - \Pi_a^\mu \Pi_a^\mu). \quad (2.29)$$

where, oppositely, the full symmetry of  $J^\mu J^\mu$  is *reduced* by the addition of  $\Pi_a^\mu \Pi_a^\mu$ . The generalization to independent couplings is also studied, recently for example in [79]. But all such models feature only a discrete symmetry as in  $\mathbb{Z}_2$ -GN models, the realization of which gets "rotated" between purely chiral and purely parity transformations.

The HS transformed version of the purely fermionic LAGRANGIAN is

$$\mathcal{L}_{\chi\text{GN,HS}} = \bar{\psi} D[\Delta] \psi + \frac{N_f}{2g_{\chi\text{GN}}^2} |\Delta|^2 \quad (2.30)$$

where (using  $P_\pm$  from Eq. (2.5))

$$D[\Delta] = \not{\partial} + m + P_+ \Delta + P_- \Delta^*. \quad (2.31)$$

The complex boson  $\Delta$  is again an order parameter for  $\chi$ SB in the sense that

$$\langle \Delta^* \rangle = -\frac{g_{\chi\text{GN}}^2}{N_f} \langle \bar{\psi} P_+ \psi \rangle, \quad \langle \Delta \rangle = -\frac{g_{\chi\text{GN}}^2}{N_f} \langle \bar{\psi} P_- \psi \rangle \quad (2.32)$$

and transforms as  $\Delta \rightarrow e^{-2i\alpha} \Delta$  under chiral rotations  $e^{i\alpha\gamma^*}$ .

In this formulation, the order parameter  $\Delta$  is the particle-physics translation of the superconductor's gap parameter from solid-state physics [62]. Its magnitude  $\rho = |\Delta|$  is the superconducting gap while its phase  $\theta$  in  $e^{i\theta} = \frac{\Delta}{\rho}$  corresponds to the NGB modes responsible for the perfect conductivity.

With QCD in mind, one would rather split the order parameter  $\Delta = \sigma + i\pi$  into a  $\sigma$  and a (single)  $\pi$  meson, crudely modeling the corresponding low-energy DOFs in particle physics. We will use all three formulations

$$\Delta = \sigma + i\pi = \rho e^{i\theta} \quad (2.33)$$

interchangeably as is convenient in the respective situation. One should note, however, that the functional measure is not invariant under  $\sigma, \pi \leftrightarrow \rho, \theta$ , so special care is in order if these are used as fundamental DOFs in calculations (as opposed to observables as in our case).

**NAMBU-JONA-LASINIO (NJL) models.** NJL models further generalize  $\chi$ GN models to feature the full flavor-chiral symmetry. This was achieved originally by replacing the flavor-singlet pseudoscalar with the flavor-vector interaction term

$$\mathcal{L}_{\text{NJL}} = \frac{g_{\text{NJL}}^2}{2N_f} (S^2 - P_a P_a) \quad (2.34)$$

for  $N_f = 2$ . From a symmetry perspective, a further term  $\propto J^\mu J^\mu$  could be added and is, e.g., included in [70], but historically [9] as well as physically such a term is usually discussed separately. The technical argument for this was originally that in the often considered large- $N_f$  limit this term decouples [70].

From a physical perspective, the NJL interaction is usually meant to model the low-energy behavior of QCD as is best seen in the HS language,<sup>11</sup>

$$\mathcal{L}_{\text{NJL,HS}} = \bar{\psi} D[\sigma, \vec{\pi}] \psi + \frac{N_f}{2g_{\text{NJL}}^2} (\sigma^2 + |\vec{\pi}|^2). \quad (2.35)$$

One can see that the NJL model can describe three pions and a  $\sigma$  meson (nowadays known as  $f_0(500)$  [80]) – the lightest particles relevant for  $\chi$ SB in QCD [81] – as composite particles.

Nowadays, the term (generalized) NJL model is used for a variety of different models featuring scalar and pseudoscalar interactions usually pertaining a large part of, if not the full, flavor-chiral symmetry [82].

**THIRRING (TH) models.** The chronologically first 4FT formulated in a modern language featured an interaction [8]

$$\mathcal{L}_{\text{TH}} = \frac{g_{\text{TH}}^2}{2N_f} J^\mu J^\mu. \quad (2.36)$$

It also preserves the full chiral symmetry and was originally discussed as a completely soluble QFT in 1+1 dimensions (with a single flavor). This is due to the large conformal symmetry in this specific setup. It can be regarded as a gauge-fixed gauge theory [83] and is closely related to (massive) quantum electrodynamics (QED) [84].<sup>12</sup> This is best seen in the HS formulation

$$\mathcal{L}_{\text{TH,HS}} = \bar{\psi} \not{D}[A] \psi + \frac{N_f}{2g_{\text{TH}}^2} A_\mu A^\mu \quad (2.37)$$

<sup>11</sup>The precise form of  $D[\sigma, \vec{\pi}]$  is not of particular interest for this thesis but can be found in [20].

<sup>12</sup>Even though QED is *not* the said hidden gauge theory.

where

$$\mathcal{D}[A] = \not{\partial} + i\not{A} + m. \quad (2.38)$$

One should stress that – while  $A^\mu$  obeys a similar DSE

$$\langle A^\mu \rangle = -\frac{g_{\text{TH}}^2}{N_f} \langle J^\mu \rangle \quad (2.39)$$

as the GN models – it is not an order parameter because (appropriately contracted)  $J^\mu$  are invariant under chiral/parity transformations.

**The single-flavor model.** In 1+1 and 1+2 dimensions, which are predominantly considered in this thesis, a peculiarity occurs: For a single irreducible flavor, i.e. two complex (or four real) DOFs, there exists only a single non-vanishing combination of four fermion components  $\propto \psi^0 \psi^1 \psi^{0*} \psi^{1*}$ . Thus, all irreducible single-flavor 4FTs must be equivalent up to a rescaling of the coupling constant and, in fact, the aforementioned FIERZ transformations boil down to

$$(\bar{\psi} M \psi)^2 = \det M \cdot (\bar{\psi} \psi)^2 \quad (2.40)$$

for this special case. This implies that *all* (or better "the one") irreducible single-flavor 4FTs are conformal in 1+1 dimensions (because TH is) and spontaneously parity-breaking for sufficiently strong coupling in 1+2 dimensions (because  $\mathbb{Z}_2$ -GN is) [70]. Supplemented with MF results that become exact for infinite flavor number, this provides first plausible expectations for other finite flavor numbers.

**Reducible models.** In 1+2 dimensions, one is often led to consider reducible fermion representations. We will apply the above naming scheme to LAGRANGIANS of the same form regardless of the representation of the spinors. One should note, however, that the irreducible and reducible theories with the same name generally differ, even if they contain the same number of DOFs (i.e.  $N_f = 2N_r$ ). This is best seen in the (non-)existence of chiral symmetry (and its potential spontaneous breakdown) as opposed to parity symmetry, but also in the technical detail that in reducible models the SP tends to cancel between the fermions of opposite irreducible representations. This will be of major interest in Chapter 7.

**YUKAWA models.** The HS formulations reveal a strong similarity to YUKAWA models which consist of coupled fermions and bosons that are both dynamical DOFs (as opposed to 4FT where only the fermions have an explicit kinetic term). Despite this apparent difference, these models are usually governed by the same fixed points (FPs) [85] and oftentimes discussed in terms of one another. Their connection is most direct in the limit  $N_f \rightarrow \infty$  which translates to an infinite mass for the bosons such that their kinetic term can be neglected.

This thesis will be mostly concerned with  $\chi$ GN and  $\mathbb{Z}_2$ -GN models in 1+1D (in Chapter 6) and TH models in 1+2D (in Chapter 7). But the other models described here play an important role as extensions or relatives and will be also discussed in Chapter 3.

## 2.7 External Parameters

We close this chapter with a short description of the thermodynamic control parameters we consider. In EUCLIDEAN field theory, temperature  $T$  is realized by a finite temporal extent of spacetime with (anti-)periodic boundary conditions for (fermions) bosons [70]. More precisely,

$$T = \frac{1}{k_B \beta} \quad (2.41)$$

where  $\beta$  is the temporal extent of the system and  $k_B$  is the BOLTZMANN constant (which is 1 in our units). A large temperature prefers entropic contributions to the free energy over energetic contributions which typically increases disorder and tends to destroy long-range order and restores broken symmetries.<sup>13</sup> A finite temperature is quite naturally realized in a lattice setup as we will use it in the following and we will vary the temporal extent of our system to change the temperature.

The average particle number is a conserved quantity due to the  $U(1)$  subgroup of the flavor-vector symmetry. Its density

$$n_B = \bar{\psi} \gamma_0 \psi \quad (2.42)$$

is often called baryon density in the literature (e.g. [88]) as fermionic bound states in our models could be seen as a simple model of QCD's baryons. We will adopt this nomenclature throughout this work. We can encourage the system to increase the average baryon number by adding a term  $\mu n_B$  to the LAGRANGIAN. The coefficient  $\mu$  is known as *chemical potential* and is the other thermodynamic control parameter we will vary in this thesis.

In addition to the above, the literature considers the dependency on a wide range of further internal and external parameters. Depending on the dimension and representation, one or even multiple mass terms can be introduced that usually break explicitly one of the previously discussed symmetries.<sup>14</sup> Isospin chemical potential and imaginary chemical potential are popular parameters to consider in lattice QCD because they mitigate the infamous sign problem [70] but at least the former has direct applications in heavy ion collisions [90]. An external magnetic field can lead to a rich and interesting phase diagram [86, 87] and is found in neutron stars [6], heavy ion collisions [91] and the early universe [92].

---

<sup>13</sup>Interestingly, there are exotic scenarios where moderate temperatures were shown to trigger SSB while it was not present at low temperatures. The corresponding effective potential was first given in [86] but [87] seems to be the first to explicitly plot this.

<sup>14</sup>See e.g. [88] for a discussion of the massive phase diagram in some  $\mathbb{Z}_2$ -GN models and [89] for a discussion of the various mass terms in 1+2D TH models.



# Chapter 3

## Analytical Precursors

Compared to the fundamentally realized QFTs in nature, like QCD, 4FTs are relatively simple and oftentimes results of reasonable quality can be obtained even by analytical means. This chapter will collect pertinent analytical precursors to our numerical work. It summarizes common knowledge as well as recent developments both of which were most recently reviewed in [70]. We will start out from the simplest case, viz. the homogeneous MF solution in Section 3.1.1, and discuss successively more involved scenarios by dropping homogeneity in  $\chi$ GN (Section 3.1.2) and  $\mathbb{Z}_2$ -GN (Section 3.1.3) models in 1+1D. Afterwards, we will turn to more realistic scenarios in higher dimensions in Section 3.2 and finally drop the MF approximation, too, in Section 3.3. We will conclude with a short review on the interpretation of the discussed facts in the literature in Section 3.4.

### 3.1 Mean-Field Results in GROSS-NEVEU-like Models

Schematically, integrating the HS form of a 4FT using Eq. (2.2) one arrives at

$$Z = \int \mathcal{D}\phi e^{-N_f S_{\text{eff}}}, \quad S_{\text{eff}}[\phi] = \int \frac{|\phi|^2}{2g^2} - \ln \det D \quad (3.1)$$

wherein  $\phi$  collects all auxiliary bosons (e.g.  $\phi = (\sigma, \vec{\pi})$  for NJL),  $D$  is the DIRAC operator including the appropriate YUKAWA couplings (e.g.  $D = D[\sigma, \vec{\pi}]$ ),  $g^2$  is to be replaced by the pertinent 4FT coupling constant and  $|\phi|^2$  is to be expanded appropriately. The purely bosonic effective action  $S_{\text{eff}}$  describes the behavior of the auxiliary field governed by the interaction with the fermions.

This form is the starting point for most approaches to 4FTs. One of the simplest of such is the MF approximation or large- $N_f$  limit:<sup>15</sup> It starts by expanding the integral around minima of the effective action. Assuming that there is only a single (global) minimum<sup>16</sup>  $\phi_{\text{min}}$ , one can

---

<sup>15</sup>The following argument would work equally well for approaching the semi-classical limit  $\hbar \rightarrow 0$  due to the (in natural units) implicit prefactor  $\frac{1}{\hbar}$ .

<sup>16</sup>In order to ensure this, one might have introduced a small trigger explicitly breaking symmetries of the system.

approximately compute

$$Z = e^{-N_f S_{\text{eff}}[\phi_{\min}] + \mathcal{O}\left(\frac{1}{N_f}\right)} \approx e^{-N_f S_{\text{eff}}[\phi_{\min}]} \quad (3.2)$$

up to deviations of order  $\frac{1}{N_f}$ . It, hence, becomes exact in the limit  $N_f \rightarrow \infty$ . The absence of a zeroth order term in  $N_f$  is ensured by the extremal condition

$$\left. \frac{\delta S_{\text{eff}}[\phi]}{\delta \phi} \right|_{\phi_{\min}} = 0 \quad (3.3)$$

called the *gap equation*. This reduces the problem to the minimization of  $S_{\text{eff}}$ . Assuming that a non-vanishing, constant minimum exists, we can measure everything in units of the dimensionful  $\phi_0 = \phi_{\min}(T = 0, \mu = 0)$  which yields a consistent renormalization condition.<sup>17</sup>

### 3.1.1 Homogeneous GROSS-NEVEU-like Phase Diagrams

This minimization is still far from trivial and usually not accessible to analytical methods in full generality. Therefore, it is often supplemented with physically sensible assumptions. The most common one is constancy of the boson field(s) which seems to be adequate due to translational symmetry. Under this assumption,  $\mathbb{Z}_2$ -GN,  $\chi$ GN and NJL<sup>18</sup> models become equivalent and a non-vanishing expectation value<sup>19</sup> of the auxiliary field has the same effect as a mass term, except for being constrained by the additional conditions imposed by the gap equation, Eq. (3.3).

The phase diagram (PD) of the large- $N_f$  GN model in 1+1 dimensions was first addressed by [94] from the particle-physics perspective but had already been known in the condensed matter literature for over twenty years at that point [95]. The corresponding PD in the temperature-chemical-potential plane is included in Fig. 3.1a. At vanishing chemical potential and sufficiently strong coupling, the theory allows for a non-vanishing condensate  $\sigma_0$  at vanishing temperature which we will use to set the scale. Increasing temperature, the condensate decreases monotonically until it vanishes continuously at a temperature

$$T_c/\sigma_0 = e^\gamma/\pi \approx 0.567 \quad (3.4)$$

wherein  $\gamma$  is the EULER-MASCHERONI constant. This second-order phase transition (PT) extends to small non-vanishing chemical potentials with monotonically decreasing critical temperature. At

$$T_t/\sigma_0 \approx 0.318, \quad \mu_t/\sigma_0 \approx 0.608, \quad (3.5)$$

<sup>17</sup>Theoretically, one should then measure an experimental value for  $\phi_0$  but in many studies – including this one – the considered scenario is not close enough to any (high-energy physics) real-life system for such a value to be meaningful. So, we will be content with dimensionless numerical values throughout this thesis.

<sup>18</sup>For NJL, one usually assumes further that  $\langle \vec{\pi} \rangle = 0$  in order to comply with QCD phenomenology [93].

<sup>19</sup>In this approximation, the minimizing configuration also constitutes the expectation value.

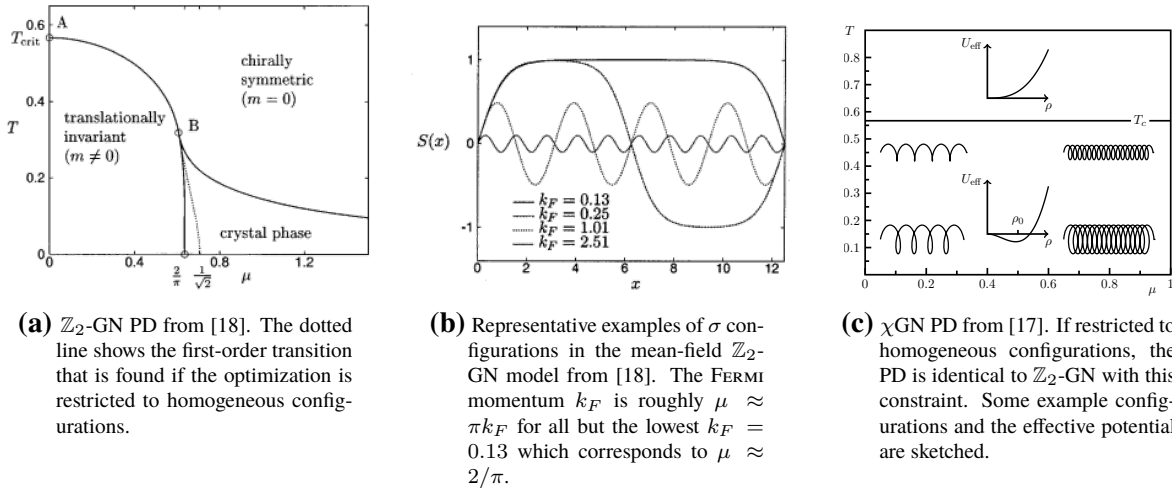


**Figure 3.1:** MF PDs and example configurations of  $\mathbb{Z}_2$ -GN and  $\chi$ GN models in 1+1D.

the transition becomes first order (indicated by the dotted line). This first order transition line reaches vanishing temperature for

$$\mu_c/\sigma_0 = 1/\sqrt{2} \approx 0.707. \quad (3.6)$$

For larger chemical potentials, no condensation takes place. At vanishing temperature, the fermion number density vanishes for chemical potentials below this value and jumps to a finite, monotonically increasing value above it.

In 1+2D systems, the PD looks qualitatively very similar with the notable difference that there is no first-order transition but all finite-temperature transitions are of second order [96]. Only at vanishing temperature, the effective potential degenerates into becoming completely flat between  $\phi = 0$  and  $\phi = \phi_0$  such that it does not fit into the standard classification of first and second order transitions. In 1+3 dimensions, 4FTs are generically not renormalizable but keeping a finite cutoff one can again find qualitatively similar results.

### 3.1.2 Inhomogeneities in Chiral Gross-Neveu Models

The assumption of constant condensate turned out to be an oversimplification that is not justified (at least in 1+1 dimensions): In [18], the PD was revised by numerical minimization (later re-derived by completely analytical means [16]) in a larger subspace of bosonic configurations allowing for some inhomogeneous configurations. It is shown by the solid lines in Fig. 3.1a for  $\mathbb{Z}_2$ -GN and in Fig. 3.1c for  $\chi$ GN. It not only differs for the different models but also features inhomogeneous phases in large parts of the finite-chemical-potential region of the PD.

Despite the additional boson field, it turns out that the large- $N_f$   $\chi$ GN model is analytically easier to handle. In [97], the general (constant-in-time) solution of the necessary condition Eq. (3.3) was found. It consists of a four-parameter family of complex condensates periodically varying in amplitude and complex phase.<sup>20</sup> A minimization in this subspace of boson configura-

<sup>20</sup>Amplitude and phase variations are governed by two of the four parameters. The other two parameters describe

tions reveals that for all chemical potentials, the large- $N_f$   $\chi$ GN model features a so-called chiral spiral ( $\chi$ spiral) equilibrium

$$\Delta(x) = \rho(T)e^{ik(\mu)x}. \quad (3.7)$$

The dependence on temperature and chemical potential completely decouples in the sense that the wave number

$$k(\mu) = -\mu \quad (3.8)$$

is a function of the chemical potential only, while the amplitude  $\rho(T)$  monotonically decreases with the temperature vanishing at  $T_c$  from Eq. (3.4) independent of the chemical potential. The zero-chemical-potential axis is understood as the degenerate limiting case of infinite wavelength, i.e. constant condensate. Some example configurations can be seen in Fig. 3.1c.

It is no coincidence that the critical temperatures of  $\chi$ GN and  $\mathbb{Z}_2$ -GN (the latter at vanishing chemical potential) agree. In fact, the finite wave number enters the partition function only in form of  $(k + \mu)$  which upon minimization not only yields the above linear dependence but also removes the dependence on both from the partition function rendering it equal to the  $(\mu = 0)$  partition function of the  $\mathbb{Z}_2$ -GN model.

Despite the condensates being space-dependent, the overall configuration is still rather homogeneous: Most physical properties, like e.g. the mass gap (given by the amplitude) or the fermion number density, do not depend on the position in space. Intuitively speaking, the system accommodates the additional fermions enforced by the chemical potential in the least intrusive way by slightly twisting the condensate avoiding expensive amplitude variations (in terms of free energy, see Section 3.3).

### 3.1.3 Inhomogeneities in Discrete GROSS-NEVEU Models

In retrospect, the optimal solutions for the  $\mathbb{Z}_2$ -GN model found in [16] can be constructed from the solutions of the  $\chi$ GN model upon constraining to real-valued solutions. While the potential energy of fermions is lowest in strongly varying condensates [88], amplitude variations are massive and therefore costly with respect to their free energy (similar to Section 3.3). This competition cannot be avoided by (massless) phase variations as in the  $\chi$ GN model lifting the degeneracy of the partition function and leading to the much richer phase structure seen in Fig. 3.1a.

The PD features a region of homogeneous condensation not unlike the purely homogeneous PD at low temperature and chemical potential. It does not, however, exhibit any first-order PTs<sup>21</sup>

---

overall amplitude and phase shift.

<sup>21</sup>Interestingly, the assumption of having a first-order PT hindered the first (particle physics) discovery of inhomogeneous structures in this model: Already [98] reports finding inhomogeneous configurations in MC simulations of a  $\mathbb{Z}_2$ -GN model but interprets them as coexistence of phases around what they believed to be a first-order PT.

but instead is separated from the rest of the PD by second-order PTs all the way down to  $T = 0$  where it arrives at

$$\mu_c/\sigma_0 = 2/\pi. \quad (3.9)$$

This value matches the analytically-known baryon mass [99] the mismatch of which was a conundrum in the homogeneous version of the PD.

At low temperature and intermediate chemical potential, a transition into a new inhomogeneous or "crystal" phase replaces the previously found first-order transition and unmasks the latter as an artifact of overconstrained minimization. Close to the transition, the optimal configurations are kink-antikinks (KAKs) exhibiting sharply localized interpolations hosting  $N_f/2$  fermions between large patches of almost constant condensate. Increasing the chemical potential and thereby the number of fermions to accommodate, these so-called baryons<sup>22</sup> are moved together – barely changing their shape – until at sufficient overlap, the KAK structure more and more resembles simple cosine-like waves.

As in the  $\chi$ GN model, the amplitude and wavelength are predominantly governed by temperature and chemical potential respectively but the strict independence is lost and the transition temperature at which the amplitude vanishes decreases monotonically with the chemical potential. Several examples are shown in Fig. 3.1b. The distinguished point  $(T_t, \mu_t)$ , Eq. (3.5), keeps a special meaning as the position where the temperature-driven PT between homogeneously broken and symmetric phase splits up into the homogeneous-inhomogeneous and inhomogeneous-symmetric transitions.

## 3.2 Inhomogeneities in (Closer-To) Real-World Systems

Nowadays, there is no doubt that several 4FTs exhibit inhomogeneous phases in 1+1 dimensions at strictly infinite flavor number. This particular setting is admittedly very restrictive and it is widely known that a tendency to infrared (IR) divergencies in low-dimensional systems can lead to peculiar behavior (see Section 3.3 for more details). In that sense, it has rather served as a proof of principle and spawned research into more realistic variations of the models although [16] beautifully summarizes the significant interest on the condensed matter side from a particle-physics perspective. Before we will drop the MF approximation in Section 3.3 (and all later chapters), we will have a look into higher-dimensional large- $N_f$  results and their applicability.

In terms of particle physics, a 1+3-dimensional model is what to aim for. As an intermediate step there have been several investigations into 1+2D theories [100–103]. As opposed to the 1+1D case, no analytical methods are known that can solve the problem in full generality. Therefore, several ansatz-based approaches were chosen either using educated guesses from the 1+1D blueprints or tractability considerations. Additionally, lattice formulations of the theory were used for less (but still partly) constrained minimizations of the effective action. While none

---

<sup>22</sup>The name is chosen following the corresponding particles in QCD although there is no color DOF in our model.

of the methods so far found inhomogeneous phases in the fully renormalized theory, a small regularization-dependent *inhomogeneous island* near the critical chemical potential  $\mu_c$  at very low temperatures as well as a larger *inhomogeneous continent* for exceedingly large chemical potentials were found [103]. The latter one is strongly intertwined with the cutoff scale<sup>23</sup>, while the former – despite vanishing in the continuum limit – seems to feature an independent scale and is therefore, in addition to its resemblance with other inhomogeneous phases found in 1+1 and 1+3 dimensions, considered more relevant for phenomenology (at least in 1+3 dimensions [104]). However, there are also regularization procedures that do not produce inhomogeneities at all. This result is hardened by stability analyses for a broad class of models.

While these findings are rather disenchanting concerning the possibility of inhomogeneous phases in QCD, one should note that inhomogeneous phases do not only exist (and even preceded) in solid-state physics [105] but are actually experimentally measured these days [106].<sup>24</sup> The crucial difference to particle physics is the fact that there is an inherent cutoff scale, viz. the lattice spacing, that is considered natural in such systems.

In 1+3 dimensions, there has been an ongoing effort exploring inhomogeneities in 4FTs [20, 107, 108] and beyond [104]. As such theories are not renormalizable, they are treated as effective theories with an intrinsic cutoff and in that setup again<sup>25</sup> an inhomogeneous island and continent are found.

However, there are a number of open questions that are actively investigated currently. While the open questions concerning correct scalesetting in the NJL model and its YUKAWA extension, known as the Quark-Meson (QM) model, have been clarified recently [109], these corrections still do not allow for the renormalized limit to be taken in the QM model which from theoretical considerations should be renormalizable [20]. This could be a truncation artifact (as conjectured in [104]) but might also signal an incompatibility of QCD phenomenology with the QM model's FP; after all, QCD is *not* the QM model and there is no reason to believe that the ultraviolet (UV) limit of the QM model could reproduce the low-energy measurements of QCD. This should, of course, not be seen as a major limitation because the QM model is either way only meant as an effective theory; but it prohibits a first proof of principle in 1+3 dimensions.

Furthermore, after the strong regularization dependence was discovered in 1+2 and 1+3 dimensions [103, 108], these results have to be reconsidered. The procedure that is most used, viz. PAULI-VILLARS regularization, is among the ones featuring inhomogeneities while other, e.g. lattice, regularizations feature none or very different inhomogeneous phases. This casts some doubt on the reliability of such predictions even when understood as effective theories. To prefer one result over the other would require a justification in what sense this method is superior.<sup>26</sup>

<sup>23</sup>in the sense that chemical potential and dominant wave numbers are of the same order as the cutoff

<sup>24</sup>In the cited studies a magnetic field, rather than a chemical potential, is used to introduce the necessary imbalance but this is a typical translation to be made between the relativistic field-theoretical formulation and the non-relativistic physical real-life system in condensed matter physics [16].

<sup>25</sup>More precisely, these studies preceded chronologically and motivated the 1+2D ones.

<sup>26</sup>With gratitude I remark that the following paragraphs were strongly influenced by private communication with L. PANNULLO including some helpful pointers to the literature and personal opinions.

There are two lines of reasoning around this in the literature: First, a sharp cutoff (like in lattice formulations) makes momenta of and above the scale of the cutoff inaccessible to the regularized theory. This will spoil the shape of the phase diagram if such momenta are relevant as was, for example, commented in [104, 110]. It seems, however, not quite plausible that such distortions should not be systematically removeable as long as the physically relevant momenta constitute an own scale independent of the cutoff (e.g. given by the chemical potential as above).

The study in [104] additionally finds surface terms arising from sharp momentum cutoffs. It remains to be investigated if they could be removed by other means, e.g., explicit counterterms, and how they affect observables of interest. A similar situation is later discussed in Section 5.5 where an explicit removal was possible but the divergent terms oftentimes did not actually affect observables of interest in the first place (see also [66]).

All in all, this question is actively discussed and no definite answer is known yet. Regularization seems to be even more challenging without the clear expectation that all relevant momenta can be considered small and the missing renormalizability lifts the necessity that different schemes yield the same results.

### 3.3 Beyond Mean Field and No-Go Theorems

Next, we will lift the restriction to infinite flavor numbers and consider perturbations around the MF solution. We will focus on  $\chi$ GN models due to their conceptual simplicity.

The saddle-point approximation Eq. (3.2) immediately gives a way to compute corrections to the MF result. After a rather lengthy, but straightforward, calculation the effective action of small fluctuations  $\delta\rho, \delta\theta$  around the  $\chi$ spiral solution

$$\Delta = (\rho + \delta\rho) e^{ikx+i\delta\theta} \quad (3.10)$$

at vanishing temperature turns out to be

$$\begin{aligned} 2\pi\delta^2 S_{\text{eff}} &= \int \delta\rho K_{\Delta} \operatorname{arsinh}\left(\frac{\sqrt{-\Delta}}{2\rho}\right) \delta\rho \\ &\quad + \int \delta\theta \left( \frac{\rho^2}{K_{\Delta}} \operatorname{arsinh}\left(\frac{\sqrt{-\Delta}}{2\rho}\right) + \frac{\Delta}{8} \right) \delta\theta \end{aligned} \quad (3.11)$$

$$= \int \left( \delta\rho^2 + \frac{1}{12\rho^2} (\nabla\delta\rho)^2 + \frac{1}{8} (\nabla\delta\theta)^2 \right) + \dots \quad (3.12)$$

where, importantly,  $\Delta$  denotes the LAPLACIAN and *not* the complex auxiliary field and the dots denote higher-order terms [42]. In there, we used

$$K_{\Delta} = \left( 1 - \frac{4\rho^2}{\Delta} \right)^{\frac{1}{2}}. \quad (3.13)$$

Before further analyzing the formula, one should note that this result does not depend on

the chemical potential or the underlying  $\chi$ spiral explicitly. In fact, the expansion Eq. (3.11) was already given in [44] which was not concerned with finite chemical potential at all. This is only true if the wave number is allowed to vary freely in order to match the chemical potential exactly. We will see that the constraints of a finite lattice will lift this degeneracy.

As expected, both bosonic DOFs can propagate via fermion loops as seen from the kinetic terms in the expansion. The mass term of the amplitude fluctuations  $\delta\rho$  was already present in the microscopic action Eq. (2.30).

As opposed to  $\delta\rho$ , the compact variable  $\delta\theta$  does not acquire a mass. Thus, concerning the long-range behavior we can safely neglect amplitude fluctuations. Defining the thermal correlation length found in [44]

$$\xi_\beta = \frac{2N_f}{\pi T} \alpha, \quad \alpha = 1 + 2 \sum_{n \in \mathbb{N}} (-1)^n (n\beta\rho) K_1(n\beta\rho), \quad (3.14)$$

wherein  $K_1$  is the modified Bessel function of second kind, we find

$$C(x) \approx \rho^2 e^{-2ikx} \langle e^{i\delta\theta(t,0) - i\delta\theta(t,x)} \rangle \xrightarrow{x \rightarrow \infty} \rho^2 e^{-2ikx} \begin{cases} x^{-\frac{1}{N_f}} & T = 0, \\ e^{-\frac{x}{\xi_\beta}} & T > 0. \end{cases} \quad (3.15)$$

Eq. (3.15) shows that there does not exist any long-range order at finite flavor number in 1+1D  $\chi$ GN models. Instead,  $\chi$ spirals get disordered over large distances by phase fluctuations. Only if the limit  $N_f \rightarrow \infty$  is performed before  $x \rightarrow \infty$ , the MF result of SSB is recovered.

This is in accordance with pertinent no-go theorems. It is common lore by now that IR divergences tend to destroy long-range order in low-dimensional systems. Originally, several authors came to the same conclusion [111–113]:

**Theorem 1 (CHMW).** *Continuous symmetries cannot be broken spontaneously in 1+1 dimensions.*

The theorem can be understood from different perspectives although the underlying mathematical ideas are very similar. [113], for example, proved that the massless boson field has a non-renormalizable IR divergence in 1+1 dimensions. Thus, the would-be NGB necessitated by such a broken symmetry cannot exist. [111] instead provided an upper bound for the magnetization in the prototypical example of the HEISENBERG model.

Either way, the proof of the theorem hinges on the divergences of pertinent integrals. These integrals are intimately related to the nature of the low-energy spectrum of the system (e.g. the relativistic dispersion relation of the NGB). While these particles and their properties are easily identified for the (would-be) breakdown of internal symmetries, it is – to the best of my knowledge – not clear, if physical systems in which external symmetries, like translational invariance, are involved in this breakdown could produce exotic low-energy dispersion relations that are not captured by the above assumption.

In particular, the standard NGB counting from relativistic systems does not apply in non-relativistic systems, like systems at finite density, and even non-standard dispersion relations can occur in such scenarios [114, 115]. For example, in supersolids exhibiting inhomogeneities at least part of the low-energy spectrum does not exhibit a relativistic dispersion relation [116]. It is therefore not clear if the possibility of strict long-range order can be disregarded purely on grounds of Theorem 1 if external symmetries are involved and we were not able to answer this question in  $\mathbb{Z}_2$ -GN models.

One should note that this theorem is circumvented in the large- $N_f$  limit by decoupling the divergent mode from the theory [41]. This explains how the limit of Eq. (3.15) can become a constant at vanishing temperature. Intuitively, one can picture  $N_f$  as acting like a further spacetime dimension in that it provides additional weight to the integrand of the path integral fostering its localization in one of the degenerate minima. This intuitive argument as well as the explicit results in [41] make clear that this mechanism is an artifact of the large- $N_f$  limit. Still, we cannot *a priori* exclude the possibility of decoupling the (would-be) NGB by some other mechanism.

Nevertheless, concerning  $\chi$ GN models overwhelming evidence from multiple sources is now available to support a scenario of *quasi*-long-range order: Besides the abstract application of Theorem 1, Eq. (3.15) from the analytical side and the numerical simulations later on provide multiple ways to arrive at the same conclusion (see Chapter 6). This scenario allows for arbitrarily large, but necessarily finite, correlated regions, in a sense that there is no length scale at all related to the decorrelation over large distances. This BEREZINSKI-KOSTERLITZ-THOULESS (BKT) scenario, named after [117–119], boils down to a competition between the pair-production energy penalty and the growth in phase-space volume associated with the latter. The original work is concerned with 2-(spatial-)dimensional gases at finite temperature but the argument works similarly when replacing the thermal partition function by a functional integral from quantum theory. This competition results in rationally decaying correlations as seen for vanishing temperature in Eq. (3.15).

The general entropy-vs-energy argument is, however, much older. In a short paragraph at the end of [120],<sup>27</sup> it is proven that:

**Theorem 2 (LL).** *There is no SSB at finite temperature in systems of one spatial dimension.*

This stronger statement implies all kinds of symmetries. Its application gives rise to the complete loss of scale-free correlation of (either strict or quasi-)long range at finite temperature. Instead, we find a thermal mass that continuously vanishes for  $T = 0$ . In that sense,  $T = 0$  can be regarded as a critical line.

---

<sup>27</sup>Even that work was preceded by less formal argumentation with the same idea, e.g. [121].

### 3.4 Applicability and Quantum-Spin-Liquid Conjecture

The previous discussion might have raised some doubts about the applicability of these low-dimensional results to full-fledged physical systems. Therefore this final section will highlight two important ideas from the literature.

First, correlated patches of spacetime are probably very large compared to the spatial regions of high density in which our models are applicable. In one of the original works it reads [122]: *"Note that the exact bound [...] may well be so weak as to allow two-dimensional systems of less than astronomic size to display crystalline order."* So, even in case of a neutron star – the prototypical example of a system of high density – correlations might be sufficient to give rise to mostly crystalline behavior.

This is probably also true for most tabletop experiments in solid-state physics where these (or very similar) models are applicable. Although there seems to be experimental evidence for COLEMAN-HOHENBERG-MERMIN-WAGNER (CHMW)-induced disorder [123], for the popular low-dimensional system of graphene the necessary size of the sample is estimated to be of the order of  $10^{30}$  meters and, thus, practically irrelevant [124].

Second, the quasi-long-range behavior discovered in  $\chi$ GN models could be representative for all conjectured crystalline structures in particle physics: [125] analyzed a simple effective model of fluctuations around an inhomogeneous order. Interestingly, they find a double-pole structure that entails IR divergences in arbitrary dimensions. The system, thus, exhibits very similar behavior to what we will find in  $\chi$ GN models; namely, inhomogeneities on (at least) intermediate scales that are damped for large separations. They call this a quantum-spin liquid (QSL) and conjecture that the found double-pole structure could be a generic feature in such systems.

# Chapter 4

## Lattice Quantum Field Theory

Regularizing QFTs on a finite spacetime lattice is a particularly successful approach because it allows to exploit modern computer hardware. Leveraging high-performance computing, first-principle QCD simulations nowadays produce some of the most precise predictions in modern physics. This chapter explains our take on lattice-field theory and MC simulation techniques (Section 4.1) before discussing the lattice-fermion-specific lattice artifact phase (LAP) (Section 4.2) and introducing some notation (Section 4.3). It concludes with some words about scalesetting in Section 4.4.

### 4.1 Lattice Quantum Field Theory and Monte Carlo Techniques

Starting from a  $d$ -dimensional continuum QFT in infinite volume described by its LAGRANGIAN  $\mathcal{L}_{\text{cont}}$ , we can introduce a set of finitely many spacetime points  $\Lambda$  on which we choose to approximate our system. Unless stated otherwise, we will assume  $\Lambda$  to be a regular lattice with  $N_t$  points in temporal direction and  $N_s$  points in each spatial direction amounting to  $|\Lambda| = N_t \times N_s^{d-1}$  points in total separated by an isotropic lattice spacing  $a$ . This is not strictly necessary, and there are interesting alternatives, but such setup is employed in the overwhelming majority of studies in this area due to its simplicity.

In order to describe continuum and infinite-volume physics, we are interested in a lattice LAGRANGIAN  $\mathcal{L}_\Lambda$  formed from fields  $\phi : \Lambda \rightarrow \mathbb{R}$  or  $\mathbb{C}$  that obeys  $\mathcal{L}_\Lambda \rightarrow \mathcal{L}_{\text{cont}}$  in the limiting cases where  $aN_s \rightarrow \infty$  while  $a \rightarrow 0$ . The EUCLIDEAN temporal extent  $aN_t$  plays the role of an inverse temperature that should be kept fixed in order to describe a fixed temperature in these limits. The choice of  $\mathcal{L}_\Lambda$  is, by far, not unique and, while all valid discretizations are required to show the correct limiting results, their approach to this limit can be very different. The particularly intricate issue of choosing an appropriate  $\mathcal{L}_\Lambda$  for fermionic DOFs is devoted a separate Chapter 5.

As in the analytical approaches in Chapter 3, fermionic interactions are usually replaced by auxiliary HS fields such that our lattice studies amount to investigations of the bosonic systems

Eqs. (2.25), (2.30) and (2.37). The corresponding high-dimensional integrals can be evaluated by MC methods, i.e. stochastic sampling, in case that the weight  $\exp(-N_f S_{\text{eff}})$  is real and positive, where

$$S_{\text{eff}} = \ln \det D[\phi] + U(\phi) \quad (4.1)$$

denotes the effective bosonic action wherein  $\phi$  collects all the relevant bosonic DOFs, e.g.,  $\phi = \sigma$  for  $\mathbb{Z}_2$ -GN, and so on, and  $U(\phi)$  is the quadratic potential term, e.g.,  $\propto \sigma^2$  in  $\mathbb{Z}_2$ -GN models.

If  $\exp(-N_f S_{\text{eff}})$  is negative or even complex for some configurations of  $\phi$ , the stochastic interpretation breaks down and all known, generally applicable ways to recover strictly non-negative weights become infeasible in the thermodynamic limit. This is the infamous SP, a general solution of which is likely to not exist [54]. It hinders, for example, simulations of lattice QCD at non-vanishing baryon density but is also a hurdle for many applications in condensed matter physics.

Concretely, the importance sampling MC method draws  $N_{\text{MC}}$  random configurations  $\phi_n, n = 1, \dots, N_{\text{MC}}$ , distributed according to  $\exp(-N_f S_{\text{eff}})$  and approximates the expectation value of an observable as

$$\langle \mathcal{X} \rangle \approx \frac{1}{N_{\text{MC}}} \sum_{n=1}^{N_{\text{MC}}} \mathcal{X}[\phi_n]. \quad (4.2)$$

For the generation of configurations, the method of choice is usually a MARKOV chain for which one generates the next field configuration from the current (and only the current) configuration. Starting from an initial (probability distribution of) configuration(s), a MARKOV chain with transition probability  $p$  is guaranteed to converge to the desired probability distribution  $P_{\text{eq}}(\phi)$  under the following conditions [1]:

**Positivity.** For all configurations  $\phi, \phi'$ :  $p(\phi \rightarrow \phi') \geq 0$ .

**Normalization.** For all configurations  $\phi$ :  $\sum_{\phi'} p(\phi \rightarrow \phi') = 1$ .

**Balance.** For all configurations  $\phi'$ :  $\sum_{\phi} P_{\text{eq}}(\phi) p(\phi \rightarrow \phi') = P_{\text{eq}}(\phi')$ .

The first two basically ensure that  $p(\phi \rightarrow \cdot)$  actually is a probability distribution. The non-trivial condition is *Balance* which ensures that  $P_{\text{eq}}(\phi)$  is a FP of the MARKOV chain. For practical purposes, it is usually replaced by the somewhat simpler sufficient *detailed balance*

$$P_{\text{eq}}(\phi) p(\phi \rightarrow \phi') = p(\phi \rightarrow \phi') P_{\text{eq}}(\phi'). \quad (4.3)$$

For the concrete update step that generates the next configuration, a variety of proposals are available in the literature [1, 90]. State-of-the-art simulations of lattice fermions typically use the hybrid MC (HMC) algorithm. It proposes a global update of the current configuration by solving a fictitious molecular dynamics system that simulates moving the configuration

through a potential-landscape defined by the effective action with randomly drawn initial momentum. This approach significantly reduces the unavoidable autocorrelations (ACs) between successively drawn configurations as long as the effective action is sufficiently well-behaved. In particular cases where the effective action is ragged and contains several (almost) degenerate minima that are separated by high ridges, the HMC struggles because – pictorially speaking – it cannot tunnel through such ridges and instead needs large initial momentum as well as long trajectories to climb them and arrive in the new valley.

As in many other MC algorithms, a METROPOLIS-accept/reject step after a short trajectory ensures convergence to the correct distribution, i.e. we accept the proposed update with probability

$$p(\phi_n \rightarrow \phi_{n+1}) = \begin{cases} 1 & \text{if } S(\phi_n) > S(\phi_{n+1}) \\ e^{-(S(\phi_{n+1})-S(\phi_n))} & \text{else} \end{cases} \quad (4.4)$$

and otherwise revert to the configuration  $\phi_{n+1} = \phi_n$  we started with.

More specifically, we use the rational HMC (rHMC). The "rational" part in rHMC refers to the treatment of the fermion determinant. Given a DIRAC operator (see Chapter 5), we approximate the fermion determinant by so-called *pseudo-fermions*. These are  $N_{\text{pf}}$  bosonic fields the dynamics of which is governed by (some power of) the inverse DIRAC operator

$$(\det D)^{N_f} = (\det D^\dagger D)^{\frac{N_f N_{\text{pf}}}{2N_{\text{pf}}}} \propto \int \mathcal{D}\phi \exp \left[ - \sum_{p=1}^{N_{\text{pf}}} \phi_p^\dagger (D^\dagger D)^{-\frac{N_f}{2N_{\text{pf}}}} \phi_p \right] \quad (4.5)$$

where  $D$  refers to the single-flavor DIRAC operator. The first equality assumes  $\det D$  to be real (and non-negative if  $N_f$  is odd). The proportionality constant drops out in expectation values. An exact computation of the rational power of  $D^\dagger D$  would still be prohibitively expensive, so we approximate this by  $k$  rational functions on an interval via

$$(D^\dagger D)^n \approx r(D^\dagger D, n) = \alpha_0(k) + \sum_{i=1}^k \frac{\alpha_i(n)}{D^\dagger D + \beta_i(n)}. \quad (4.6)$$

The individual terms together can be evaluated with almost no overhead using a multi-shift conjugate-gradient solver [90]. The values of  $\alpha_i(n), \beta_i(n)$  are computed using the REMEZ algorithm in the implementation of [126] to obtain optimal approximations of  $x^n$  over a fixed interval chosen to include the whole spectral range of  $D^\dagger D$  for typical field configurations.

The simulations for this thesis were performed with the code that was also used in [127] and was adapted to the new research questions during the work on this thesis. Many more implementation details can be found there. Tables providing a high-level overview over the parameter sets used during the simulations can be found in Appendix B. More details are available in the code and data releases [63].

## 4.2 The Lattice Artifact Phase

Interacting fermions on the lattice generically feature a strong-coupling phase that is usually not related to continuum physics. It was realized in [22] that this is related to an additive renormalization of the coupling constant that shifts the point of infinite renormalized coupling strength to a strictly positive value of the inverse bare coupling.

In [128], the origin of this phase was explained quite intuitively:<sup>28</sup> On a finite lattice, one can integrate out the fermion interaction directly, thereby trading the path integral for a combinatorial sum over occupation number configurations that indicate if an interaction is happening at some lattice point in this configuration.<sup>29</sup> This divides each configuration into a set of sites at which the fermions move freely and its complement where the fermions take part in the interaction. The typical proportions of free and interacting sites are governed by the coupling strength and increasing the coupling strength will at some point lead to a situation where on average (almost) all sites are occupied by interactions. In such configurations, the dynamical part described by the free moving fermions is no longer represented faithfully.

This problem originates purely from the finite lattice spacing because in a continuum representation we would always have an infinite number of fermion states available such that it is not possible to prohibit all dynamics by PAULI blocking. In fact, reducing the lattice spacing in the above case would be achieved by reducing the bare coupling implying to move out of this artifact region again.

This extremely-strong-coupling region goes under different names in the literature but we will call it the LAP, indicating that we consider it an artifact of the discretization that does not affect the continuum limit. This perspective is, e.g., taken in [22, 89, 128]. In condensed matter theory instead, this is a valid phase in the phase diagram of pertinent models [130, 131] because there, a finite lattice spacing is an intrinsic property of the system.

It is often found to be separated from the continuum phases by a first-order PT, e.g. in [130], that does not allow for a continuum limit to be constructed which again emphasizes the lattice-only character of this phase. However, in [96] data consistent with a second-order percolation transition were presented which would match well with the above explanation and also [131] speculates for this to be of second order. It is not unlikely that the order of this transition is model dependent.

One of the typical consequences of entering this phase in lattice simulations is found to be a (usually rapidly) decreasing condensate with increasing coupling. As this is the opposite to typical behavior in continuum phases, it manifests in a non-monotonic behavior of pertinent condensates. Consequently, some authors locate this transition via the maximum of a measured condensate [89]. In Chapter 7, we will use a more tailor-made approach in line with the above description and will, in fact, find that a maximum in the condensate is *not* related to the entrance into the LAP if the continuum phase from which one is entering the LAP does not feature a

---

<sup>28</sup>The following description is vastly simplified not including multiple flavors or flavor-multiplet interactions.

<sup>29</sup>This procedure is inspired by the fermion-bag algorithm [129].

condensate beyond numerical noise.

For all results in this thesis, we made sure to simulate outside of the LAP unless explicitly stated.

### 4.3 Notation

For the rest of this thesis, we will adopt some common notation: First and most importantly, we will use the same symbol for the expectation value of an observable  $\langle \mathcal{X} \rangle$  and its lattice estimator  $\langle \mathcal{X} \rangle$ , i.e. the left-hand and right-hand side of Eq. (4.2). Unless explicitly stated otherwise, we will average an estimator over the whole spacetime lattice  $\Lambda$  of  $|\Lambda|$  points – in order to increase statistics while carefully preserving relations between lattice points. So, if  $\mathcal{X}(\delta x)$  depends on  $\phi(x)$  and  $\phi(x + \delta x)$ , we imply the following

$$\langle \mathcal{X}(\delta x) \rangle = \frac{1}{N_{\text{MC}}} \sum_{n=1}^{N_{\text{MC}}} \frac{1}{|\Lambda|} \sum_{x \in \Lambda} \mathcal{X}[\phi_n(x), \phi_n(x + \delta x)]. \quad (4.7)$$

Some care is in order if dealing with non-linear operations within this convention. Most prominently, this includes taking the absolute value in the estimation of condensates. We will imply such an absolute value for condensates in fermionic, e.g.  $\langle \bar{\psi} \psi \rangle$ , as well as bosonic representation, e.g.  $\langle \sigma \rangle$ , *in between* the spacetime and the MC average unless stated otherwise, i.e.

$$\langle \sigma \rangle = \frac{1}{N_{\text{MC}}} \sum_{n=1}^{N_{\text{MC}}} \left| \frac{1}{|\Lambda|} \sum_{x \in \Lambda} \sigma(x) \right|. \quad (4.8)$$

We will denote by  $\mathcal{F}[f]$  the FOURIER transform (FT) of a function  $f$ . Depending on the context, this should be interpreted as a continuous or discrete form as appropriate.

For correlation functions, we define the connected correlator

$$\langle \phi(x) \phi(y) \rangle_c = \langle \phi(x) \phi(y) \rangle - \langle \phi(x) \rangle \langle \phi(y) \rangle. \quad (4.9)$$

We will sometimes refer to the spatial lattice  $\Lambda_s$  only.

### 4.4 Scalesetting

It is usually convenient to work in so-called lattice units in which everything is measured in units of the lattice spacing. In order to extract results in physical units or even just compare between different parameter sets, we have to express the lattice spacing itself in terms of a known physical observable which is typically the experimentally measured mass of some particle. This is less relevant for the study of critical properties without external parameters due to the expected scale invariance in the vicinity of a second-order PT but is of utmost importance if external parameters and, obviously, explicit length scales like spatial inhomogeneities are considered. The former

applies to our studies of TH models and we will spare us the trouble of setting a scale there but instead focus on the  $\mathbb{Z}_2$ -GN and  $\chi$ GN scalesetting here.

Our models of interest are sufficiently far away from real-world physical systems that no experimental data exist to which we could fit our model. Instead, we will optimize for comparability with the MF prediction. In  $\mathbb{Z}_2$ -GN models, we can set the scale by measuring the dimensionless

$$a\sigma_0 = \langle \sigma \rangle_{T=0, \mu=0}. \quad (4.10)$$

Thus, if we are interested only in quantities made dimensionless by comparing them to  $\sigma_0$ , e.g.  $T/\sigma_0$ ,  $L\sigma_0$  or  $\langle \sigma \rangle / \sigma_0$ , we can immediately translate between lattice units and such physical quantities by multiplying/dividing by the respective power of the above numerical value. Physically, one could imagine that we are able to measure the real-world value of the condensate and build our whole system of units on top of that. We will take over the values from [65] here as the same ensembles are used.

We can do the equivalent procedure for  $\chi$ GN models by measuring

$$a\rho_0 = \langle \rho \rangle_{T=0, \mu=0}. \quad (4.11)$$

One should note that this is a valid scale whenever there is a non-trivial global minimum in the effective action for  $\rho$ . This does neither imply nor assume any form of symmetry breaking because the crucial aspect of SSB is that the complex phase  $\theta$  spontaneously chooses a fixed value. Nevertheless, the measurement of this number poses significant problems as is laid out in detail in [42]. Although the methods described there have significant shortcomings, I have not found a better method and will, hence, proceed using the values stated there.

# Chapter 5

## The DIRAC Operator and its Discretizations

In order to study fermionic theories in MC simulations, one has to discretize the DIRAC operator  $\not{\partial}$  on a finite set of points. In Section 5.1, I will first gather important properties of the DIRAC operator in the continuum the preservation of which in a discretized setting is desirable. Unfortunately, it turns out that the no-go theorem of NIELSEN and NINOMIYA [132, 133] forces one to compromise in this respect. I will then describe the various formulations of fermions on the lattice (Sections 5.2 to 5.4) relevant to this thesis. I will shortly introduce a method to couple a chemical potential to SLAC fermions in Section 5.5 and discuss the SP in Section 5.6. This chapter mostly contains commonly known facts that can be found in pertinent textbooks (e.g. [70, 90]). As introduced before, we will work in units of the lattice spacing such that  $a = 1$  unless otherwise stated.

### 5.1 Properties of the Continuum DIRAC Operator

In the continuum, the DIRAC operator is an anti-HERMITIAN<sup>30</sup> operator

$$\partial_\mu^\dagger = -\partial_\mu \quad \Rightarrow \quad \not{\partial}^\dagger = -\not{\partial} \quad (5.1)$$

where the conclusion about  $\not{\partial}$  follows from the fact that the  $\gamma$ -matrices are HERMITIAN in EUCLIDEAN spacetime. Whenever there exists a  $\gamma_*$ , it anti-commutes with them

$$\gamma_* \not{\partial} \gamma_* = \not{\partial}^\dagger \quad (5.2)$$

---

<sup>30</sup>Strictly speaking, one has to be careful about the domains at this point but I will only use the following algebraic relation, so I will be slightly sloppy in this regard.

which realizes the chiral symmetry of free massless fermions. Parity and time-reversal symmetry are similarly implemented as

$$\mathcal{T}^{-1}\not{\partial}(x)\mathcal{T} = \not{\partial}(\mathcal{T}^\mu{}_\nu x^\nu), \quad (5.3)$$

$$\mathcal{P}^{-1}\not{\partial}(x)\mathcal{P} = \not{\partial}(\mathcal{P}^\mu{}_\nu x^\nu) \quad (5.4)$$

and  $\not{\partial}$  is translationally invariant. It is a local operator in the sense that  $\not{\partial}f(x)$  depends on the function  $f$  only in some neighborhood of  $x$ . Its eigenfunctions<sup>31</sup> are plane waves

$$\partial_\mu e^{-ipx} = -ip_\mu e^{-ipx} \quad (5.5)$$

such that it is diagonal in momentum space. The relation between the momentum  $p$  enumerating the eigenfunctions and the corresponding eigenvalue is linear and I will call this a dispersion relation, thereby slightly generalizing from its usual meaning relating momentum to (kinetic) energy. It has exactly one root which is at  $p = 0$  and corresponds to a pole of the propagator for the single massless fermion it describes.

## 5.2 Ultralocal Discretizations

The most naive approach to formulate fermions on the lattice is the use of a simple nearest-neighbor derivative stencil. While forward and backward derivatives are not anti-HERMITIAN, the central derivative

$$\not{\partial}_{xy} = \sum_{\mu=0}^d \gamma_\mu (\delta_{x^\mu+1,y^\mu} - \delta_{x^\mu-1,y^\mu}) \prod_{\substack{\nu=0, \\ \nu \neq \mu}}^d \delta_{x^\nu,y^\nu} \quad (5.6)$$

allows for a consistent implementation of fermions on the lattice. It is *ultralocal* because it only depends on a constant finite number of neighboring points independent of the lattice size and it is chiral in the sense of Eq. (5.2). Its dispersion relation is indeed linear around the origin (describing one fermion here as desired) but has further roots whenever at least one of the momenta is  $\pm\pi$ . These correspond to additional fermions that are described in this discretization. They are called doublers because the total number of fermionic DOFs described via this prescription doubles for each spacetime dimension. This is a serious problem if one is interested in a particular number of fermions but, if it is acceptable to work with multiples of  $2^d$  fermions, one can use the doublers as physical DOFs. It is then, however, necessary to carefully check that all couplings with other fields and external parameters have the correct form for all doublers. This problem was first realized in [134] and we worked out two formulations for the interaction term of the GN model in [65].

It turns out that the operator from Eq. (5.6) only couples half of the doublers among each

---

<sup>31</sup>Since I did not specify the HILBERT space to work on, these might be improper eigenfunctions.

other. By a (local) redefinition of the field variables the operator becomes diagonal in the (re-defined) spinor space. The so-called *staggered* formulation reduces the doublers to  $1/2^{\lfloor d/2 \rfloor}$  their original number by keeping only one such component. It is widely used – particularly in QCD [90] – despite its reduced symmetry group. The continuum theory arising from staggered fermions is the KÄHLER-DIRAC theory [135]. In the perturbative weak-coupling regime, one can show that the original symmetry is recovered but for the non-perturbative case of the 1+2D TH model, [136] showed that this theory differs from the standard TH model. Similar differences are likely to appear in other strongly coupled theories, too, and thus we did not use staggered fermions for this thesis.

Another famous and ubiquitous approach to the reduction of doublers is the WILSON formulation. It gaps out the doubler DOFs by a momentum dependent mass that diverges in the continuum limit. This comes at the expense of breaking chiral symmetry explicitly which, in turn, allows for an additive mass renormalization. A chirally symmetric continuum limit is, hence, only reached via finetuning of at least one parameter [137] and chiral symmetry is, at best, approximately realized at finite lattice spacing. Since chiral properties are essential in our studies, we did not use WILSON fermions in this thesis either.

This ubiquitous failure of translating all properties of the continuum DIRAC operator to the lattice is a general principle formalized by the NIELSEN-NINOMIYA theorem [132, 133]:<sup>32</sup>

**Theorem 3** (NIELSEN-NINOMIYA). *There exists no translationally invariant DIRAC operator that fulfills the four following properties:*

1. *locality*:  $|\not{\phi}_{xy}| \lesssim e^{-\text{const}|x-y|}$  asymptotically for large  $|x - y|$
2. *continuum limit*:  $\lim_{a \rightarrow 0} \not{\phi}_{pq} = \delta_{pq} \gamma^\mu p_\mu$
3. *no doublers*:  $\not{\phi}_{pq}$  is invertible on the subspace  $p, q \neq 0$
4. *chirality*:  $\{\gamma_*, \not{\phi}\} = 0$ .

In one dimension, its proof boils down to the necessity of (at least) one further root in any dispersion relation that is linear through the origin and periodic. In general dimensions, the intuition is the same but the formulation uses a more precise but abstract topological language. After all, the question is not if, but only which, property will be violated on the lattice.

Results with naive fermions were used during the studies as a crosscheck to rule out common pitfalls with more elaborate approaches. These results are not presented in this thesis but can be found in the corresponding publications [65, 67, 68].

---

<sup>32</sup>The formulation is taken from [70]. The reader should note that there are further (presumably) independent studies from that time coming to the same conclusion [138].

### 5.3 Nonlocal Discretizations

A complementary approach to ultralocal derivatives is the SLAC<sup>33</sup> derivative [139, 140]. It starts from the desired dispersion relation, Eq. (5.5), and equidistantly discretizes it up to a finite box cutoff

$$\not{D}_{pq} = -i\not{p}\delta_{pq} \quad (5.7)$$

in momentum space. In position space, this yields a non-local coupling along the axes that falls off as  $\mathcal{O}(1/|x-y|)$ .<sup>34</sup> By definition, it is the most precise lattice approximation of the continuum DIRAC operator in momentum space, it has no doublers and it is chiral. Unfortunately, non-locality is unacceptable in gauge theories where it yields non-LORENTZ-invariant counter terms [138, 142, 143] and, thus, after some attempts to cure this the interest in the SLAC derivative waned over the years. However, in theories without local symmetries (and even after complete gauge-fixing) many studies found it not only to produce correct results [42, 43, 64–68, 96, 141, 144–149] but also to be superior to other formulations, e.g. in terms of discretization errors [65]. It is, hence, the discretization of choice for this thesis.

But the SLAC derivative is conceptually much richer: It is a simple example of a pseudospectral discretization. This approach describes an operator in terms of its spectrum (including the corresponding eigenfunctions) and afterwards introduces a cutoff there. It captures the DOFs of the continuum theory that are most important with respect to the operator in question. These can differ significantly from the ones easily described on common lattice structures, e.g. hyper-square or hexagonal lattices.<sup>35</sup> Consequently, in a pseudospectral approach usually a much smaller cutoff yields precise results as was observed for the SLAC derivative above.

Thus, there is an obvious explanation for the failure of the SLAC derivative in gauge theories: The free DIRAC operator is not gauge-invariant and neither is a cutoff of the free DIRAC operator's spectrum. Instead, a pseudospectral discretization of the covariant derivative is a valid formulation of gauge-theories on the lattice. This could be an advantageous formulation of fermions in static background fields. Unfortunately, this is not a practical approach for dynamical gauge fields because the discretization would not only change after every update, its calculation for a general gauge configuration will generically also require lots of resources.

---

<sup>33</sup>after the Stanford Linear Accelerator Center where the respective ideas were developed

<sup>34</sup>A very explicit description of the position space formulation is given in [141].

<sup>35</sup>Coincidentally, they do not in the case of the SLAC derivative because the hyper-square momentum grid transforms to a hyper-square position grid.

## 5.4 Local Discretizations

It turns out that while Theorem 3 requires some violation of the desired properties, these can be chosen to be very small. The GINSPARG-WILSON relation [150]

$$\{\not{\partial}, \gamma_*\} = a\not{\partial}\gamma_*\not{\partial} \quad (5.8)$$

describes an alternation of the chiral symmetry that is of  $\mathcal{O}(a)$  and vanishes in the continuum limit. One solution to this equation is the overlap formulation<sup>36</sup>

$$a\not{\partial} = \mathbb{1} + A \left( \sqrt{A^\dagger A} \right)^{-1}, \quad A = a\not{\partial}^{(\text{Wilson})} - \mathbb{1}. \quad (5.9)$$

While Eq. (5.8) is only defined if  $\gamma_*$  exists, Eq. (5.9) can be written down in any dimension and gives rise to fermions on the lattice, even if there is no  $\gamma_*$  [152]. The overlap formulation inherits the gapped-out doublers from the WILSON formulation and is local but not ultralocal.<sup>37</sup> It features a non-local lattice version of chiral symmetry [155]

$$\delta\psi = i\alpha\gamma_* \left( 1 - \frac{a}{2}\not{\partial} \right) \psi, \quad \delta\bar{\psi} = i\alpha\bar{\psi} \left( 1 - \frac{a}{2}\not{\partial} \right) \gamma_*, \quad (5.10)$$

wherein  $\alpha$  is a small parameter, that converges to the standard continuum chiral symmetry.

The closely-related domain-wall (DW) formulation at the same time serves as a computational tool and an intuitive interpretation of the overlap formula: The chiral fermions are interpreted as edge modes of a bulk (WILSON) theory in a space with one additional spatial dimension [156]. If the separation of the domain walls on which the physical fermions live tends to infinity, Eq. (5.9) is recovered. A discretization of the bulk theory with a finite domain wall separation yields an approximation with a controlled limit. This is the standard approach taken in gauge theories [90]. Without dynamical gauge fields the overlap operator can be precomputed and its exact application becomes feasible on reasonably large lattices [37, 38, 87].

Overlap and DW fermions were not directly used in this work. But the former was used in other publications during my doctoral research [37, 38, 87] and the latter was the method of choice in [29, 84, 89, 136, 154, 157, 158] which will be discussed in great detail in relation with our own results on 1+2D TH models.

<sup>36</sup>The original reference is [151] but we use a formulation from [152] that does not refer to  $\gamma_*$  and is, hence, better suited for our general spacetime dimensions and fermion representations.

<sup>37</sup>This is true for the free operator. With additional field content, its locality properties can be proven under mild conditions [153]. Pertinent numerical results are found, e.g., in [154].

## 5.5 Chemical Potential on the Lattice

In the continuum language, the (particle number) chemical potential couples to the (particle number) conserved charge, i.e.

$$\mu \int d^{d-1}x \bar{\psi} \gamma_0 \psi. \quad (5.11)$$

On the lattice, the given operator is no longer a conserved charge and thereby lacks its distinguished meaning. Instead, there are various prescriptions giving rise to the correct chemical potential in the pertinent limits. In [159], a conserved current was constructed for nearest neighbor discretizations and – supplemented with an arbitrary choice of a regularizing function – this yields a family of couplings the most prominent of which is [90]

$$\phi_{xy} = \sum_{\nu=0}^d \gamma^\nu \left( e^{\mu \delta_{\nu 0}} \delta_{x^\nu, y^\nu+1} - e^{-\mu \delta_{\nu 0}} \delta_{x^\nu, y^\nu-1} \right) \prod_{\substack{\xi=0, \\ \xi \neq \nu}}^d \delta_{x^\xi y^\xi}. \quad (5.12)$$

In the above prescription the chemical potential acts like an imaginary part to the temporal component of a gauge field which is the same as in the continuum. It was widely adopted and we have used this prescription due to its established status for naive fermions.

In fact, translating the linear coupling prescription from the continuum to the lattice yields additional terms for some observables that are finite in 1+1D but diverge in higher dimensions with increasing powers of  $a^{-1}$  [66, 159]. This was originally taken as an exclusion reason but it turns out that it is a feature of the continuum theory as well although it is usually hidden by the particular ordering of limits. They can be corrected for order by order yielding highly accurate discretizations [66]. We will use such a prescription for SLAC fermions which conceptually do not lend themselves well to a hopping formulation.<sup>38</sup>

## 5.6 The Sign Problem

Whichever lattice realization was chosen, we need its determinant for all possible field configurations to be real and positive in order to use it in MC simulations. If this is not the case, the stochastic interpretation of the path integral's weight is no longer valid and the importance sampling approach (see Section 4.1) breaks down. There is a plethora of ideas for tackling such a problem [55–57] but it is no coincidence that each and every such idea either introduces new but equally hard problems or lacks a certain generality; in fact, under mild assumptions it can be proven that solving the general SP is NP-hard [54].

In practice, this means that each model under consideration has to be tested for the existence

---

<sup>38</sup>Attempts on the interpretation as a peculiar form of hopping in the early days failed [142, 143] which is generally expected from the perspective taken above. We did not investigate if the formulation in [143] which fails for dynamical gauge fields could work for the special case of a chemical potential acting as such.

of a SP. Oftentimes, the symmetries of the DIRAC operator are enough to prove its absence and we have carefully chosen our models and parameters to ensure this. If not, one has to generally expect a SP and measures have to be taken to deal with its consequences. Still, a SP can be mild, vaguely referring to the circumstances when the additional computational effort introduced by the SP is affordable in the desired parameter ranges, e.g. lattice sizes.

Our 1+1D SLAC and naive DIRAC operators have provably real determinants. As they are both real-valued matrices, we can apply complex conjugation and relate the result to the charge-conjugated version

$$D^* = \gamma^{\mu*} \partial_\mu + \sigma - i(\gamma_*)^* \pi + \mu \gamma^{\mu*} = \mathcal{C}^{-1} D \mathcal{C} \quad (5.13)$$

where we have used that the  $\gamma$ -matrices and  $\gamma_*$  are HERMITIAN as well as Eq. (2.10) and the resulting property

$$\gamma_*^\top = -\mathcal{C}^{-1} \gamma_* \mathcal{C}. \quad (5.14)$$

After taking the determinant, the two factors of charge conjugation cancel such that  $\det D$  equals its complex conjugate. Being diagonal in flavor space, even flavor numbers ensure that the single-flavor determinant occurs in even powers only casting it non-negative.

For our 1+2D reducible TH simulations, the argument even simplifies a little. In an appropriate basis, the DIRAC operator is block-diagonal with two identical blocks up to a sign in the (irreducible)  $\gamma$ -matrices. As the mass term is HERMITIAN and the SLAC derivative (including the auxiliary vector field) is anti-HERMITIAN (and they commute), the two blocks are HERMITIAN conjugates of each other. Thus, the determinant is real and non-negative as a product of complex conjugated eigenvalue pairs.



# Chapter 6

## GROSS-NEVEU Models in 1+1 Dimensions

This chapter is devoted to a detailed study of 1+1D GN models at finite flavor number. As discussed in Chapter 3, their MF approximation predicts the exciting possibility of inhomogeneous condensates at finite density. At the same time, such low-dimensional models are generically plagued by IR divergences that prohibit most kinds of long-range order if fluctuations are present (irrespective of their nature, quantum or thermal). While this seems to render these models a special case, in recent years conjectures arose that the phenomenon of a QSL which we will encounter instead of actual long-range order might be quite generic (see Section 3.4). We will discuss  $\chi$ GN models in Section 6.2 and  $\mathbb{Z}_2$ -GN models in Section 6.3 after giving a brief summary of rather technical concerns in Section 6.1.

### 6.1 Technical Overview

#### 6.1.1 Observables

One of the most important properties of a MC algorithm is ergodicity (cf. Chapter 4). In a finite volume – hence, in every MC simulation – it implies that configurations that are related by a symmetry of the action are equally likely to be generated, even if this symmetry might be spontaneously broken after taking the infinite-volume limit. Therefore, it is common practice in MC simulations to use estimators of the infinite-volume physical observables that are invariant under all symmetry transformations [1]. For example, the magnetization in an ISING-type model is usually averaged in MC time only after taking its absolute value because otherwise it would vanish exactly in the limit  $N_{MC} \rightarrow \infty$ . This technique was also used to define  $\sigma_0$  in Eq. (4.10).

Normally, translational invariance is not among the symmetries that must be taken care of explicitly because in most scenarios observables of interest do not depend on spacetime coordinates in equilibrium. This is different in the MF predictions and we will use a similar technique as described above to arrive at spacetime-independent observables that can probe inhomogeneities. To this end, we will be careful to only consider relative spatial relations for all local observables, i.e. instead of asking "what happens at point  $x$ ?" we will be concerned with questions like "what

happens in a distance  $x$  from a maximum?".<sup>39</sup> While the answer of the former is trivial due to the exactly implemented symmetries, the answer to the latter is invariant under all symmetry transformations and can therefore yield a non-vanishing result.

Concretely, this means that instead of the local order parameter field  $\Delta_x$  or  $\sigma_x$  we will concentrate on

$$C(x) = \frac{1}{|\Lambda|} \sum_{(t,\delta x) \in \Lambda} \begin{cases} \langle \Delta^*(t, x + \delta x) \Delta(t, \delta x) \rangle & \text{in } \chi\text{GN} \\ \langle \sigma(t, x + \delta x) \sigma(t, \delta x) \rangle & \text{in } \mathbb{Z}_2\text{-GN} \end{cases} \quad (6.1)$$

and instead of the baryon density  $n_B$  in the  $\mathbb{Z}_2$ -GN

$$C_{n_B}(x) = \frac{1}{|\Lambda|} \sum_{(t,\delta x) \in \Lambda} \langle n_B(t, x + \delta x) \sigma^2(t, \delta x) \rangle. \quad (6.2)$$

The use of the squared order parameter field in the latter case is owed to the fact that  $n_B$  has twice the wave number of the order parameter itself (see Chapter 3). The additional averaging in form of the sums only improves the statistical properties of these estimators.

The reader should be aware that we consider the use of correlators as a translationally invariant description of a local observable and will often loosely speak of the latter when we mean the former. This is to be interpreted in the sense that the predominant configurations of the local observable will have the same properties as the correlator in these particular cases.<sup>40</sup>

From the above correlators, a number of properties can be extracted. First of all, Eq. (3.7) shows that if

$$k_{\max} = \frac{1}{2} \operatorname{argmax}_k \mathcal{F}[C](k) \quad (6.3)$$

is half the dominant wave number of  $C$  in MF, then the dominant configurations of the order parameter in the  $\chi$ GN ( $\mathbb{Z}_2$ -GN) are  $\chi$ spirals (cosine-like) with wave number  $k_{\max}$ . We will see that this quantity remains meaningful after the inclusion of quantum fluctuations because the MF result will still dominate the configurations.

In order to characterize the different phases of the MF phase diagram in the infinite-volume limit, one can use the following quantity

$$C_{\text{short}} = \min_x \Re C(x) \begin{cases} > 0 & \text{homogeneous } \chi\text{SB}, \\ = 0 & \text{symmetry restored phase}, \\ < 0 & \text{inhomogeneous } \chi\text{SB}. \end{cases} \quad (6.4)$$

<sup>39</sup>Of course, the term "maximum" could be replaced by any other distinguished field value.

<sup>40</sup>For example, we will later talk about the dominant wave number of the order parameter field when evaluating the corresponding property of its correlators because this property does translate directly to most configurations in an ensemble. In contrast, we will never talk about a decay of the order parameter (but always explicitly in relation to the correlator) because this is not a property of the field itself.

The name is chosen to stress that after the inclusion of fluctuations this quantity will be dominated by the short-range behavior of the system (see Section 3.3). In that case, one should be careful with the terms "phase" and "symmetry breaking". Instead, the case distinction should be interpreted as "dominated by" homogeneous, symmetric or inhomogeneous configurations, respectively, and the question of SSB has to be decided separately.

Such a decision crucially depends on the long-range behavior of the system. To probe the latter, one has to perform a careful study of the decay properties of spatial correlations. This is an intricate endeavor for  $\mathbb{Z}_2$ -GN models where one can extract the amplitude of the correlator only on discrete extremal values. It is devoted a dedicated Section 6.3.3 later on. In  $\chi$ GN models instead, it turns out that spatial correlations split up into a monotonically decaying amplitude and a single dominant  $\chi$ spiral. The former is then easily extracted taking the absolute value of  $C$  and the behavior on the largest scales on the lattice is given by

$$C_{\text{long}} = \min_x |C(x)| \begin{cases} > 0 & \text{long-range order (with respect to } \mathbb{L}), \\ = 0 & \text{short-range order.} \end{cases} \quad (6.5)$$

This quantity, however, cannot distinguish between homogeneous and inhomogeneous regimes.

## 6.1.2 Further Stumbling Blocks

During our studies, we have identified a number of further stumbling blocks the details of which can be found in the corresponding papers [42, 43, 65, 66]. Here, I will present a summary focussing on the essential aspects for the later interpretation of the results.

As is often the case in theories that have topologically distinct sectors<sup>41</sup>, our simulations on finite lattices encounter exorbitantly large AC times (ACTs) that are caused by the inability of the rHMC algorithm in use to sample efficiently from varying winding numbers. In [42], we were able to beautifully illustrate that – with our choice of HMC parameters – fluctuations within one topological sector are almost uncorrelated with ACT on the order of  $\mathcal{O}(1)$  while inter-sector jumps happen on much larger MC timescales. The latter still seem to be mostly captured by our extensive ensembles but the properties of the HMC algorithm and the physical system at hand render it inadvertible that they exceed our computational resources at sufficiently small temperatures. We cannot exclude that this happened for our smallest temperatures. Most importantly, our general conclusions do not depend on this parameter regime and remain valid even if these temperatures were not sufficiently sampled.

We have further found that this tendency for topological freezing can lead to excessive thermalization periods at the beginning of the simulation such that the choice of initial conditions can make a significant difference in terms of required computational resources. In [66], we already became aware that we lacked the computational resources to reconcile a hot and a cold start for the most challenging regions in the phase diagram. Being aware of this, I have stripped

---

<sup>41</sup>In our case, the topological invariant distinguishing these sectors is the number of oscillations in finite volume.

the unreliable data from the plots of this thesis. Plots including some data that were found to be unreliable after the fact can be found in the corresponding publications [65, 66].

For our later simulations of  $\chi$ GN models, we employed a freeze-out technique to reduce thermalization efforts. We started our simulations at some sufficiently large temperature such that AC and thermalization were easily overcome. We then froze out some thermalized configuration to a lower temperature in order to find a good initial configuration to start with. Of course, we carefully checked that this procedure does not introduce a bias by itself. Details of this can be found in [42].

The discretization of fermions is a delicate issue that was in detail discussed in Chapter 5. It can introduce various kinds of artifacts that might or might not go away when taking the continuum limit, for example doublers or distortions of the internal and external symmetries. Due to the SLAC discretization's discontinuity in momentum space a valid concern might be that this could trigger inhomogeneities in a GIBBS' phenomenon fashion that are purely artificial.

In order to tackle such concerns and, at the same time, have a crosscheck for our results, we also implemented naive fermions and used them to simulate  $\mathbb{Z}_2$ -GN models whenever possible. As described in Section 5.2, they are tainted by  $2^d$  doublers that can be regarded as physical fields in free field theory. For this procedure to yield the correct continuum limit in an interaction theory, it is of vital importance that all doublers couple to the bosonic fields correctly. Our earliest proceedings [67, 68] contained naive implementations that did not take care of this, while later work [65] introduced an additional weight function to suppress unwanted interactions.

For this thesis, results with naive fermions are not shown but the reader may rest assured that the SLAC results that are shown can be crosschecked with other, more conventional discretizations.

## 6.2 Chiral GROSS-NEVEU Models

Despite its seemingly more complicated LAGRANGIAN, it turns out that  $\chi$ GN models are conceptually much simpler than  $\mathbb{Z}_2$ -GN models. This is already seen in the MF phase diagram Fig. 3.1c which instead of a complicated competition of homogeneous and inhomogeneous phases including a critical chemical potential (cf. Fig. 3.1a) shows a very clear picture: There is a single critical temperature below which the MF order parameter is a  $\chi$ spiral for *all* parameter choices. In MF, their wave numbers and amplitudes are completely independent and governed only by chemical potential and temperature, respectively. This simplicity is due to the continuous U(1) symmetry group which further allows for a simple perturbative analysis identifying the relevant modes in the IR and renders all the no-go theorems, Theorems 1 and 2, straightforwardly applicable. From this strong analytical toolkit, we have a clear expectation about the phase diagram that will be mostly confirmed in the following.

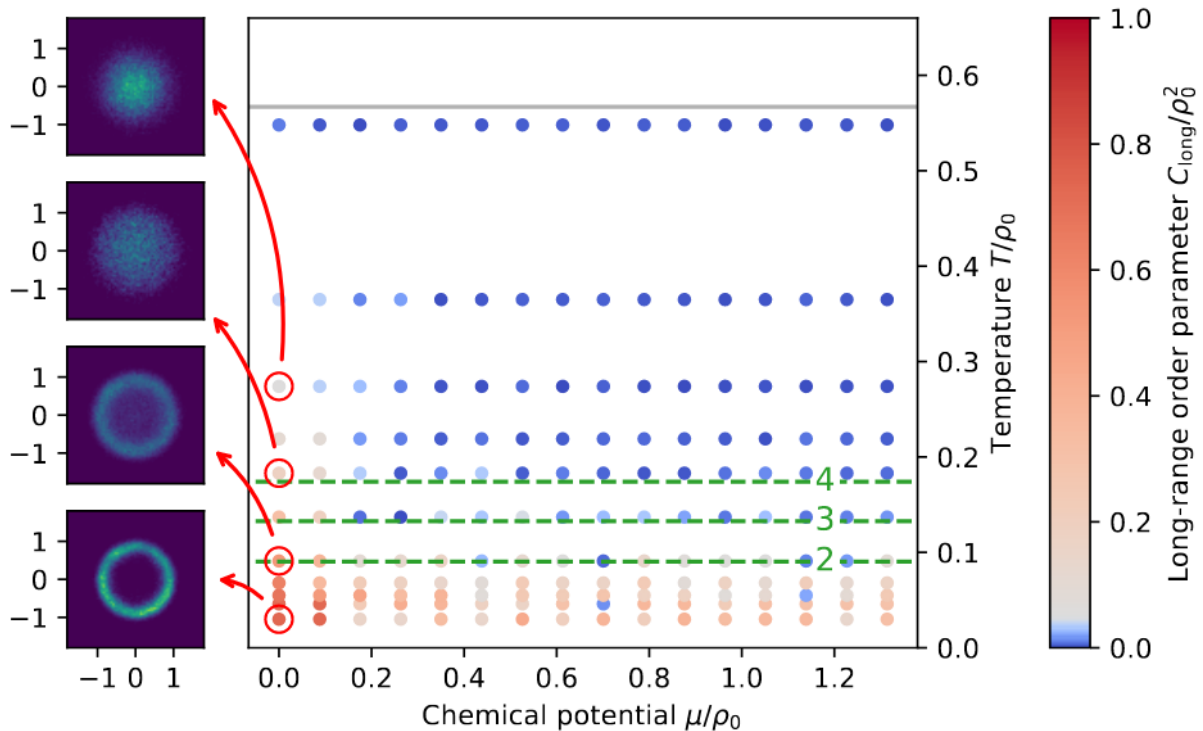


**Figure 6.1:** Finite-volume phase diagram of the  $N_f = 2$   $\chi$ GN model for  $(/a, a\rho_0) \approx (63, 0.46)$  as mapped out via  $C_{\text{long}}$ . The gray line indicates the large- $N_f$  critical line. On the left, histograms of the spacetime-averaged  $\Delta$  in the complex plane are shown for the temperatures  $T/\rho_0 \in \{0.030, 0.091, 0.183, 0.274\}$ . The colormap is linear in the blues and in the reds but with different slopes changing at 0.05 which is considered as a reasonable threshold for noise. The green dashed lines show the thresholds  $L/\xi_\beta = 2, 3, 4$  for later reference (Section 6.2.2). The given colormap will be used for all  $C_{\text{long}}$  plots in this thesis.

### 6.2.1 The Finite-Volume Phase Diagram for Two Flavors

As it turns out, in a finite volume the finite-flavor phase diagram as mapped out via the various quantities discussed in Section 6.1 is remarkably similar to the MF result up to some rescaling. In Fig. 6.1,  $C_{\text{long}}$  is shown for  $(/a, a\rho_0) \approx (63, 0.46)$ . Apart from a small low-chemical-potential region, the values of  $C_{\text{long}}$  are significantly non-vanishing only below a threshold temperature which appears to be largely independent of the chemical potential for a wide range of chemical potentials. This threshold temperature is significantly lower than the critical temperature of the MF phase diagram but as we introduced further fluctuations by lowering the flavor number an overall reduction of ordering is expected.

At vanishing density, one can clearly see a non-vanishing condensate<sup>42</sup> in the histograms on the left. For various temperatures, they show  $\Delta$  averaged over the whole spacetime lattice on a  $(/a, a\rho_0) \approx (63, 0.46)$  lattice. One should stress that on this small lattice all configurations are clearly dominated by a homogeneous background either of (would-be) symmetry-breaking or symmetric type. The histograms additionally ensure us that we are very well sampling the whole  $U(1)$  symmetric space of configurations. This is no longer true for larger lattices due to insufficient statistics but all observables are carefully designed to be invariant under this symmetry (see Section 6.1.1).

<sup>42</sup>in finite volume

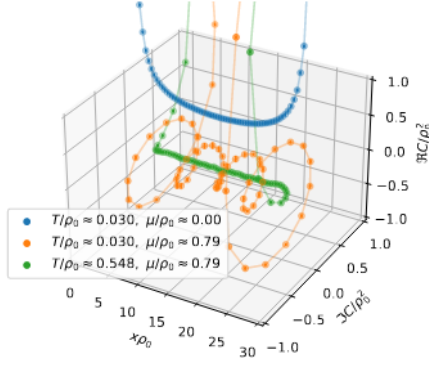


**Figure 6.2:** Representative examples of  $C$  in the  $N_f = 2 \chi$ GN model on a  $(/a, a\rho_0) \approx (63, 0.46)$  lattice.

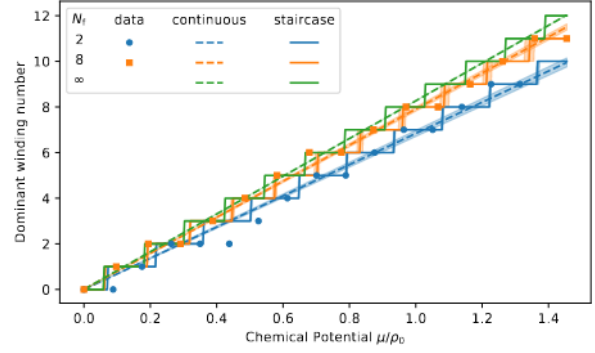


**Figure 6.3:** Dominant winding number from Eq. (6.3) for flavor numbers  $N_f = 2, 8, \infty$ . The figure shows simulation data (markers), fitted slope (dashed) and fitted staircase (solid) with  $T \approx 0.030$  for  $N_f = 2, 8$  on  $(/a, a\rho_0) \approx (63, 0.46)$  resp.  $(/a, a\rho_0) \approx (63, 0.41)$ . The values for the fits are given in Table 6.1.

Figure 6.2 shows some of the correlators that lead to Fig. 6.1. One can see the clear overall resemblance with Fig. 3.1c showing the MF results for  $\Delta$ . This includes the following non-trivial facts: The correlators at vanishing chemical potential as well as sufficiently large temperature are real and monotonically decaying. This is reassuring because the former indicates that exact chiral symmetry holds in our simulations (cf. Chapter 4) while the latter must provably hold if full EUCLIDEAN symmetry holds (so, at least at zero temperature).<sup>43</sup>

The height of the plateau where low-temperature correlators level is easily understood from our scalesetting convention: Assuming that cluster decomposition [160] holds at  $(T/\rho_0, \mu/\rho_0) \approx (0, 0)$  we expect

$$C(x) \sim \underbrace{\langle \Delta^*(x) \Delta(0) \rangle_c}_{\rightarrow 0, x \rightarrow \infty} + \underbrace{\langle \Delta^*(x) \rangle}_{=(\Delta(0))^*} \underbrace{\langle \Delta(0) \rangle}_{=\rho_0 e^{i\text{const}}} \xrightarrow{x \rightarrow \infty} \rho_0^2 \quad (6.6)$$

where we ignored the additional averaging of Eq. (6.1) for the sake of simplicity. As the amplitude is mostly independent of the chemical potential, this should also hold for  $\chi$ spiral-like regions at finite chemical potential. This is, however, true mostly *by definition* and one should not interpret this as a non-trivial result.

The remaining example correlator clearly indicates a predominance of  $\chi$ spiral-like configurations at non-vanishing density. The wave number increases with increasing chemical potential while the amplitude decays with temperature. This behavior is again reminiscent of the MF result.

As expected from Section 3.3, beyond this qualitative agreement there are minor differences:

<sup>43</sup>It is well-known that EUCLIDEAN-time correlation functions decay monotonically [75]. Using EUCLIDEAN symmetry, the same must hold for spatial correlations. One should note that we are concerned with bosonic correlators in infinite volume and zero temperature such that temporal and spatial directions are large and have the same boundary conditions. This is no longer true with a non-vanishing chemical potential explicitly breaking this rotational part of EUCLIDEAN symmetry.

**Table 6.1:** Proportionality constant between  $\mu$  and  $k_{\max}$  for all parameter settings at low temperatures. The "linear" and "staircase" fit are explained in the text (see Fig. 6.3 for a visual representation). It is important to stress that the staircase's uncertainty is not comparable to a statistical uncertainty. The quality of fit is much better assessed by the number of outliers in the staircase fit. There were 16  $\mu$  values for each parameter set.

$N_f$	$(/a, a\rho_0)$	$T/\rho_0$	linear	staircase	outliers
2	(63, 0.46)	0.030	0.8(1)	0.759(2)	4
2	(127, 0.46)	0.030	0.7(1)	0.738(9)	8
2	(255, 0.46)	0.030	0.7(1)	0.733(9)	9
2	(127, 0.19)	0.036	0.8(1)	0.806(2)	6
2	(255, 0.08)	0.087	0.9(1)	0.838(2)	5
8	(63, 0.41)	0.030	1.0(1)	0.95(1)	2
$\infty$	-	0	1	-	-

The amplitude of all correlators is significantly enhanced for small separations  $x$ . This is due to excited states that can get populated due to fluctuations. Their existence is hidden in the higher order terms in the perturbative result Eq. (3.15) that focusses on the limit of large distances.

Furthermore, the  $\chi$ spirals have different wave number as compared to their MF counterparts. A closer look at sufficiently low temperature (see Fig. 6.3), reveals that the wave numbers are generally lower compared to the MF values but equally well described by proportionality to the chemical potential. We will have a closer look at this in Section 6.2.5. These wave numbers always fit the box size without any fine-tuning which is a commensurability effect that will be discussed later.

### 6.2.2 $C_{\text{short}}$ and the Competition of Scales

Unexpectedly, the same phase diagram plotted via the quantity  $C_{\text{short}}$  as shown in Fig. 6.4 does not corroborate this great qualitative agreement with MF. While the figure exhibits the same regimes described by MF – homogeneously non-vanishing, inhomogeneous and vanishing configurations – in roughly similar parameter regions, the transitions between these regimes are significantly distorted: Predominance of homogeneous configurations extends to finite chemical potential where in MF there is always a non-degenerate  $\chi$ spiral. Even more severe, the transition temperature from inhomogeneous to mostly vanishing (i.e. symmetry-restored phase in MF) configurations is far from  $\mu$ -independent in contrast to that in MF but also via  $C_{\text{long}}$ .

However, these findings are well-explained as resulting from a competition of scales. To this end, we first list the length scales relevant to the system:

1. the lattice spacing  $a$ ,
2. the system size  $L$ ,

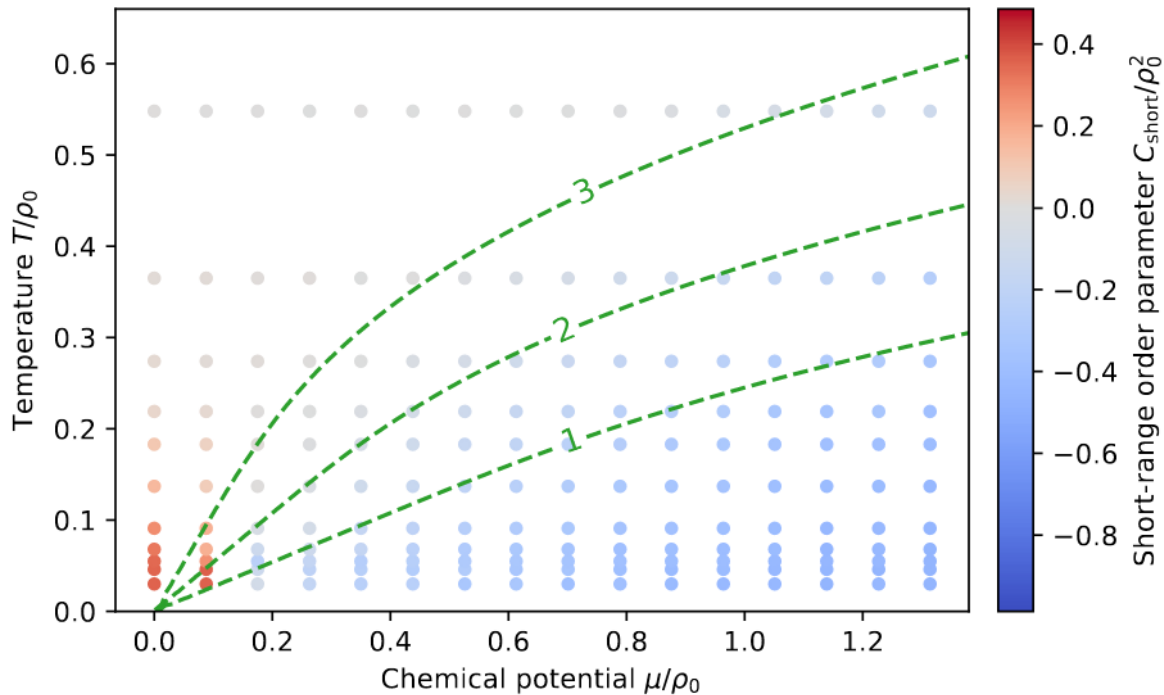


**Figure 6.4:** Same as Fig. 6.1 but with  $C_{\text{short}}$  instead of  $C_{\text{long}}$ . In this case, the green dashed lines indicate  $\log_2(\lambda_{\chi S}/\xi_\beta) = 1, 2, 3$ . The given colormap will be used for all  $\chi\text{GN } C_{\text{short}}$  plots in this thesis.

3. the (inverse) temperature  $1/T = \beta$  and

4. the (inverse) chemical potential  $1/\mu$ .

From these,  $a$  will probably not be relevant for the IR physics.<sup>44</sup> This leaves us with three scales to consider:  $L$  serves as an IR cutoff. To describe the thermodynamic limit, we intend to remove this cutoff systematically and a competition between  $L$  and another physical scale is a finite-size (FS) effect. On the one hand, FS effects are particularly important due to the ill-behaved IR limit; on the other hand, a large but finite system might be of greater physical relevance after all because the, in part, very dense matter that is described by this model will usually be confined in comparably small objects like neutron stars.

The perturbative analysis from Chapter 3 suggests that the temperature's length scale manifests itself in a finite correlation length  $\xi_\beta$  that is given in Eq. (3.14) to leading order (LO). We assume in the following that the same length scale also governs the decay of spatial correlations, similar to a screening mass. The chemical potential is proportional to the wave number of the dominant  $\chi$  spirals. In MF, this relation is exactly known, Eq. (3.8); at finite flavor number, this proportionality still holds to a high precision but the coefficient experiences quantum corrections that can be extracted from a fit to Fig. 6.3.<sup>45</sup> As the dominant wave number is discretized on a finite lattice, we also fitted a staircase function of constant step width and a step height of one

<sup>44</sup>a posteriori verified in Section 6.2.3

<sup>45</sup>The reader should note that in that figure there is a volume factor involved and due to the slightly different lattice spacings the data for different  $N_f$  are not exactly comparable. The current normalization emphasizes the integer-valuedness of the wave number to illustrate the staircase-like behavior.

to the data. While in the  $N_f = 8$  case (discussed later in Section 6.2.5) such a fit can achieve almost perfect agreement, the  $N_f = 2$  data can at best be fitted to have four outliers. As they all appear at small chemical potential they might be related to statistical or thermalization problems similar to those encountered later on in the  $\mathbb{Z}_2$ -GN models. One should note that the continuous and the staircase function are fitted independently but their slopes agree within errorbars. As fitting the discontinuous staircase function does not allow for standard algorithms to be used, the problem was solved analytically and the error is chosen as half of the width of the minimum.<sup>46</sup>

We already encountered one competition of scales, maybe the most intuitive one: An equilibrium  $\chi$ spiral has to fit into the finite box of length  $L$ . Otherwise, it will destructively interfere with itself via the periodic boundary conditions. This leads to a discretization of the allowed wave numbers  $k_{\max}$  because the winding number has to be integer-valued. This is clearly illustrated by the step-like behavior in Fig. 6.3. It is also the cause of homogeneously dominated (red) points at finite chemical potential in Fig. 6.4. A related form of FS effects that was neither encountered in  $\chi$ GN nor  $\mathbb{Z}_2$ -GN models during this study was observed in  $\mathbb{Z}_2$ -GN models in [161].

The traditional description of FS effects is also given in terms of a competition of scales: A system is usually considered plagued by FS effects if the largest correlation length in the system is of the same order as the finite system size  $L$ . Although this is a rather vague statement, one can base a qualitative comparison on this after giving some reasonable meaning to "same order". We will successfully do so in the following but the reader should be aware that the – after all arbitrary – choices going into such an estimate can have significant impact on the quantitative agreement.

Due to the use of periodic boundary conditions, the furthest separation between two points is  $L/2$ , so we are surely observing FS effects if  $L/\xi_\beta = 2$ . But more conservatively, one would not expect to describe an infinite volume if the lattice size is only three or four times the correlation length. In our case, we have a concrete prediction for the largest correlation length being  $\xi_\beta$ . Plugging in the parameters for the system under investigation, we can compare this would-be infinite-volume scale with the system size  $L$ . The result is shown in Fig. 6.1 for  $L/\xi_\beta = 2, 3, 4$ . It is in great qualitative agreement, i.e. obviously horizontal because the perturbative formula Eq. (3.14) does not depend on  $\mu$  but also of the same order of magnitude as the transition temperature. One should stress at this point that the threshold of  $C_{\text{long}}/\rho_0^2 = 0.05$  to change from red to blue colors is a reasonable but in the end arbitrary choice to distinguish noise around vanishing values from significant ones. The coincidence of the color border and the order-of-magnitude borders should, thus, be regarded as a beautiful illustration of the qualitative statement and *not* as quantitative agreement.<sup>47</sup>

<sup>46</sup>Due to the discontinuous nature of the staircase function, the cost function is piecewise constant. Thus, the "width" is well-defined. The "half of" accounts for the fact that the interval  $[c - \delta c, c + \delta c]$  shall coincide with the minimal piece where  $c$  is chosen as the center of this interval and  $\delta c$  is the provided error.

<sup>47</sup>This perspective is further corroborated when diving deeper into this estimation: Assuming that the correlators' amplitudes would be given by a single  $\cosh(x/\xi_\beta)$ , we can plug in  $x = L/2$  to get a quantitative prediction for  $C_{\text{long}}$ . This turns out to be in astonishing quantitative agreement for homogeneous backgrounds for the parameters of

Both of the above effects are strictly speaking finite-size effects because they involve a finite box size that should be removed to obtain the thermodynamic limit. However, there is one interesting pair of scales that is present even after removing all cutoffs: temperature and chemical potential. Their competition is already relevant at the MF level where the temperature dictates the amplitude while the chemical potential enforces the winding. At finite flavor number, this competition is taken one step further because the correlation length  $\xi_\beta$  is relevant in the spatial direction, too:

Clearly, if  $\lambda_{\chi S} \ll \xi_\beta$ , we will find a large number of oscillations before a notable decoherence, i.e. decay of  $C$ , sets in. If this is realized by  $\xi_\beta$  being large, which can very well happen at low temperatures, there are large coherent patches of space where the system behaves like a rigid crystal (or at least a very viscous fluid). As  $C_{\text{short}}$  is concerned, it will clearly indicate such inhomogeneity by a large negative value.

Oppositely, if  $\xi_\beta \ll \lambda_{\chi S}$ , the amplitude is damped and vanishes before a notable oscillation can build up. Instead, the additional decay due to the cosine at small argument effectively even shortens the correlation length further. Such a system will behave like a gas of massive fermions without much influence from the oscillations.  $C_{\text{short}}$  will vanish here.

In between, there is a regime where  $\xi_\beta$  and  $\lambda_{\chi S}$  are of the same order of magnitude. In this case, one can identify  $\lambda_{\chi S}$  as a dominant scale of oscillations but coherent patches of the latter are only of the order  $\xi_\beta$ , i.e. as short as only a few wavelengths. This behavior is typically found in liquids [162]. They also tend to have a preferred nearest-neighbor separation stemming from the competition of attractive and repulsive forces. The liquid constituents are, however, still moving around prohibiting larger coherent patches that would occur in a crystal. In the  $\mathbb{Z}_2$ -GN model later on, we will be able to concretely identify these "liquid constituents" to be localized baryons. In the  $\chi$ GN model without localized DOFs this correspondence remains more abstract but, of course, the physics is still the same.  $C_{\text{short}}$  will have negative but smaller values in magnitude than in the first case.

Of course, there is no strict separation between these regimes. Still, the described competition between correlation length and wavelength is capable of describing even the crossover between the  $C_{\text{short}} < 0$  to the  $C_{\text{short}} \approx 0$  regime. Again, we have to define "the same order of magnitude" which includes some arbitrary choices. As the first minimum appears at a quarter of the wavelength  $\lambda_{\chi S}$ ,  $\lambda_{\chi S}/\xi_\beta = 2$  should still have a significant, though diminished, amplitude at the first minimum.  $\lambda_{\chi S}/\xi_\beta = 4$  would thus be the regime where  $\xi_\beta$  becomes smaller than the distance to the first minimum and  $\lambda_{\chi S}/\xi_\beta = 8$  would be expected to have its first minimum disappearing into the noise after diminishing the amplitude over twice the correlation length before arriving at the first minimum. This estimate – again to be taken with a grain of salt due to the arbitrariness of scale comparisons – nevertheless yields quite reasonable agreement with the crossover regime in Fig. 6.4 and can be considered a plausible explanation for the data.

To summarize, we have identified all noteworthy features of the phase diagrams Figs. 6.1

---

Fig. 6.1 but predicts significantly higher values for most inhomogeneous backgrounds. A number of technical and physical reasons spring to mind as candidates to explain this observation but we did not proceed this further.

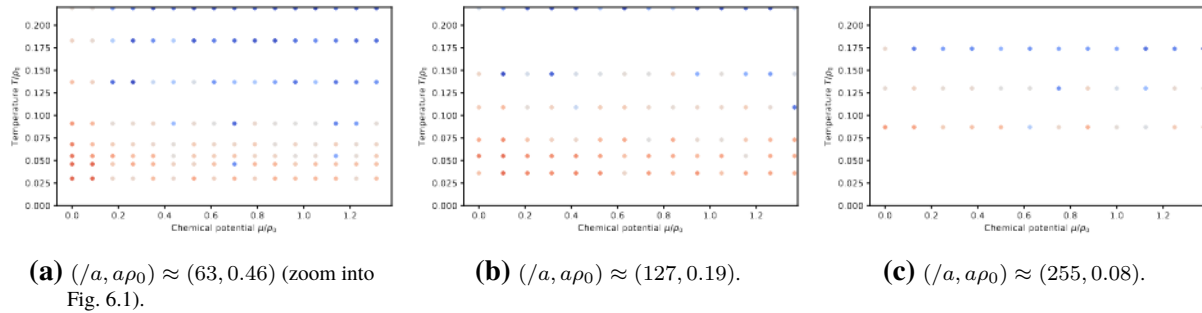


**Figure 6.5:** Finite-volume phase diagrams of the  $N_f = 2$   $\chi$ GN model for successively smaller lattice spacings with approximately constant lattice volume as mapped out via  $C_{\text{long}}$ . For comparability the colormap from Fig. 6.1 is used for all plots.

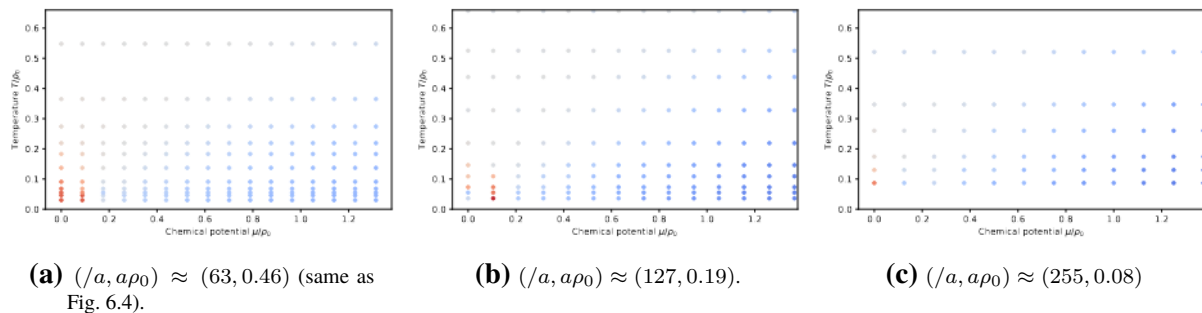


**Figure 6.6:** Same as Fig. 6.5 but with  $C_{\text{short}}$  instead of  $C_{\text{long}}$ . For comparability the colormap from Fig. 6.4 is used for all plots.

and 6.4 as arising from competing external scales. While the competition with  $\mathbb{L}$  is traditionally rather considered an artifact to be removed by extrapolation, the competition between temperature- and density-induced scales is physical and allows for an interpretation of the inhomogeneous regions in terms of a liquid regime. We will strengthen the case for this interpretation in the next sections.

### 6.2.3 Physical Limits

Before we study the IR behavior of the system to confirm our assertions about some features being FS effects, we will first verify the above assumption that  $a$  is not a relevant length scale for our further discussion. Figs. 6.5 and 6.6 show  $C_{\text{long}}$  and  $C_{\text{short}}$  for successively smaller lattice spacings. Although the troublesome scales setting does not allow for precise quantitative claims, the long-range behavior (Fig. 6.5) does not show a significant shift in the transition from non-vanishing long-range amplitude to (noisy) vanishing long-range amplitude.<sup>48</sup>

Similarly,  $C_{\text{short}}$  in Fig. 6.6 exhibits very little variation between the different lattice spacings. Most importantly, for each lattice spacing a clearly (short-range) inhomogeneous region can be identified. As shape and intensity of this region are very similar,<sup>49</sup> we can safely conclude that

<sup>48</sup>Admittedly, the data for low-temperatures are pretty sparse for the finest lattice spacing because the large temporal extent needed for small temperatures became prohibitively expensive at some point. Still, even at the moderately-small temperatures simulated,  $\chi$ spirals can be identified which hints on a similar transition temperature.

<sup>49</sup>One should note that the first non-vanishing value of the chemical potential is  $\mu/\rho_0 \approx 0.125$  for the finest lattice spacing while it is only  $\mu/\rho_0 \approx 0.087$  for the coarsest lattice. This shift – together with the slight change in

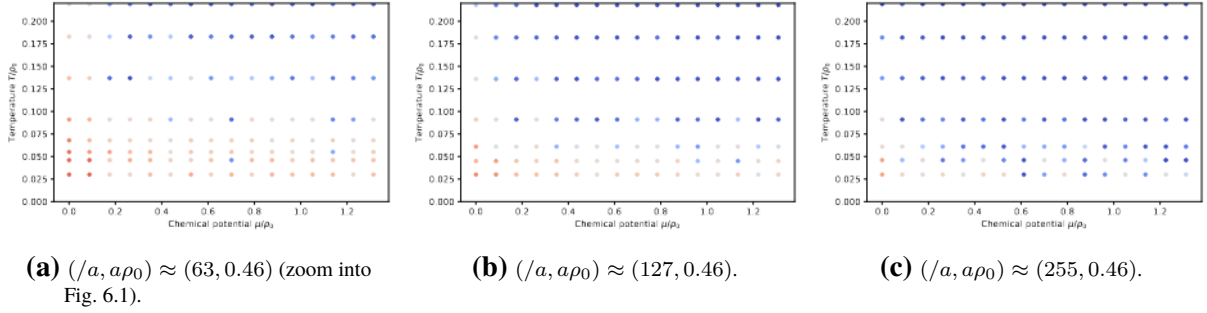


**Figure 6.7:** Finite-volume phase diagrams of the  $N_f = 2$   $\chi$ GN model for successively doubled system size at approximately constant lattice spacing as mapped out via  $C_{\text{long}}$  and zoomed into the relevant low-temperature region. For comparability the colormap from Fig. 6.1 is used for all plots.

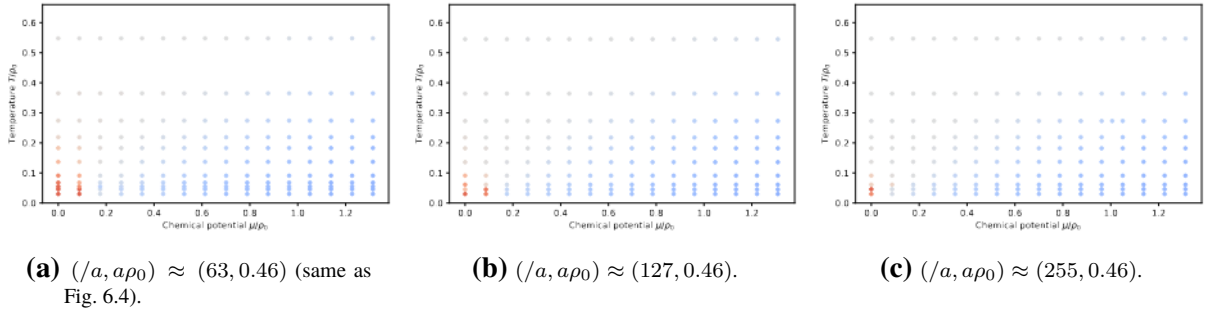


**Figure 6.8:** Same as Fig. 6.7 but with  $C_{\text{short}}$  instead of  $C_{\text{long}}$ . For comparability the colormap from Fig. 6.4 is used for all plots.

inhomogeneities are hardly affected by a decreasing lattice spacing. Nevertheless, one should mention that  $C_{\text{short}}$  shows more irregularities than  $C_{\text{long}}$ . Most prominently, there seem to be inhomogeneities at vanishing chemical potential. We strongly suspect that these are caused by thermalization problems. But despite this, there is no doubt that suboptimal  $\chi$ spiral backgrounds are still local minima of the effective action which will contribute to the partition function. In that sense, the finding should not be disregarded in totality but only seen as an overestimation due to insufficient statistics.

The interpretation of the previous section has further corroborated the dependence of our results on the system size  $\mathbb{L}$ . Figs. 6.7a and 6.8a show the same data as Figs. 6.1 and 6.4 while the remaining data in Figs. 6.7 and 6.8 are taken in successively doubled volume.

As one can see, all features that were already identified as FS effects indeed tend to disappear in the limit of large system size. These include the temperature extent of the non-vanishing  $C_{\text{long}}$  region, but also the temperature extent of the homogeneously dominated region in  $C_{\text{short}}$ —as a competition of  $\mathbb{L}$  with the thermal correlation length  $\xi_{\beta-}$ , as well as the  $\mu$ -extent of the homogeneously dominated region in  $C_{\text{short}}$  stemming from  $\lambda_{\chi S}$  compared to  $\mathbb{L}$ . In contrast to that, the crossover between the regions of  $C_{\text{short}} < 0$  and  $C_{\text{short}} \approx 0$  is not at all affected by the change in volume. This was already predicted in Section 6.2.2 because neither of the involved scales is related to the system size.

---

volume – is likely responsible for the change of sign in the low-temperature values for those values of the chemical potential.

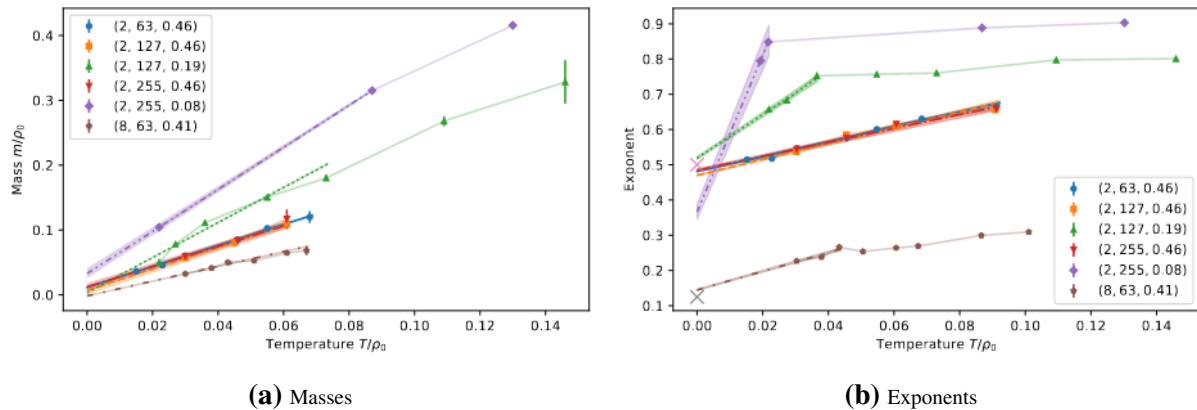


**Figure 6.9:** Physically relevant parameters extracted from fits to temporal correlators for all available lattice setups as described in the text. The parameter tuple in the legends is of the form  $(N_f, /a, a\rho_0)$ . The corresponding fit parameters are found in Table 6.2. The fit range is indicated by the extent of the dashed lines.

That the dominant wave number constitutes a scale independent of other externally induced scales of the system is a non-trivial observation. This independence should be regarded in contrast to various other scenarios, ranging from systems subject to constraints [163] that can also exhibit inhomogeneities in an attempt to conform to a suboptimal average value of the order parameter to MF results in 1+2 dimensions [101, 103] where the existence of inhomogeneities depends on the cutoff and regularization details.

## 6.2.4 Temporal Correlators

At this point, we have already established a significant amount of evidence pointing towards perturbation theory (PerT) being an accurate description of the system. But there is a direct way to establish this: spectroscopy. Instead of spatial correlators, we will now consider temporal correlations of the order parameter field. PerT predicts a finite thermal mass for all non-vanishing temperatures that, however, vanishes in the  $T \rightarrow 0$  limit. At vanishing temperature, the system finally becomes critical.

I have measured temporal correlators defined analogously to Eq. (6.1) for further analysis. In order to determine the thermal mass, I have fitted a double-cosh ansatz given by

$$C(t) = A_1 \cosh [m_1/\rho_0 \cdot \rho_0(t - t_{\text{center}})] + A_2 \cosh [m_2/\rho_0 \cdot \rho_0(t - t_{\text{center}})] \quad (6.7)$$

at vanishing chemical potential for all temperatures. This ansatz results in plausible fits over a wide range of low and moderate temperatures. The lower of the two masses is shown in Fig. 6.9a for all lattice setups available.

One can clearly see that all masses decrease for decreasing temperature. A linear extrapolation from a plausible range of temperatures is shown to give an idea of the expected  $y$ -intercept (see Table 6.2 for the parameter values). All extrapolate linearly to very small but non-vanishing masses – except for  $N_f = 8$  which is zero within errors. This is expected as a FS effect: In a

**Table 6.2:** Fit parameters for linear fits in Fig. 6.9. These fits are to be understood on a qualitative level due to the very sparse data basis. The uncertainties presented in the table are those reported by `scipy.optimize.curve_fit` [2]. They very likely underestimate the true uncertainties due to a lack of data to estimate them and possible systematic effects. They are only presented for completeness.

$N_f$	$/a$	$a\rho_0$	Masses		Exponents	
			Slope	$y$ -intercept	Slope	$y$ -intercept
2	63	0.46	1.62(3)	0.0115(9)	4.63(5)	0.481(1)
2	127	0.46	1.7(2)	0.007(7)	4.9(1)	0.470(2)
2	255	0.46	1.6(2)	0.012(6)	4.3(2)	0.485(3)
2	127	0.19	2.70(4)	0.004(1)	32.4(8)	0.519(4)
2	255	0.08	3.2(1)	0.033(8)	278(13)	0.37(2)
8	63	0.41	1.14(5)	-0.002(2)	6.4(1)	0.145(2)

finite volume and at sufficiently low temperature, the spatial extent takes over as the smallest IR scale in the system and provides a lower bound for the realizable correlation length.

The reader should note, however, that the theoretical prediction is that masses between  $N_f = 2$  and  $N_f = 8$  should differ by about a factor of  $1/4$  which is clearly not the case. I have not fully understood why that is – particularly in conjunction with the excellent extrapolation to zero of the latter – but considering the mass scale of  $\mathcal{O}(10^{-2})$  which even becomes  $\mathcal{O}(10^{-3})$  in lattice units it is very unlikely that the given lattices of at most  $N_s = 63$  and  $N_t = 80$  were capable of resolving such masses.

At sufficiently small temperature, it is also plausible for the correlations to show first signs of the expected rational decay at vanishing temperature. That is why I have also fitted a symmetrized rational ansatz of the form

$$C(t) = B \left[ \frac{1}{x^E} + \frac{1}{(-x)^E} \right] \quad (6.8)$$

with  $E > 0$  an exponent free to fit. This also results in plausible fits. Interestingly, the extracted exponents systematically overestimate the expected value of  $1/N_f$  and seem to extrapolate linearly to approximately the expected value. It should be stressed that these fits are meant to guide the eye and should not be understood as quantitative results given the sparse data to fit to.

For  $N_f = 2$  and the largest lattice spacings  $a\rho_0 \approx 0.46$  the extrapolations seem most reliable. The  $y$ -intercept in these cases systematically underestimates the naive value of  $1/N_f$ . However, a refined analysis was recently published in [164]. Their exponent is

$$E = 2 \cdot \frac{1}{N_f(1 + \lambda'/2\pi N_f)} \quad (6.9)$$

with  $\lambda' = 1/2g_{\chi\text{GN}}^2$  up to lattice artifacts. This differs from our findings and expectations by a factor of two which might be a difference in conventions or a mistake on either side. But the

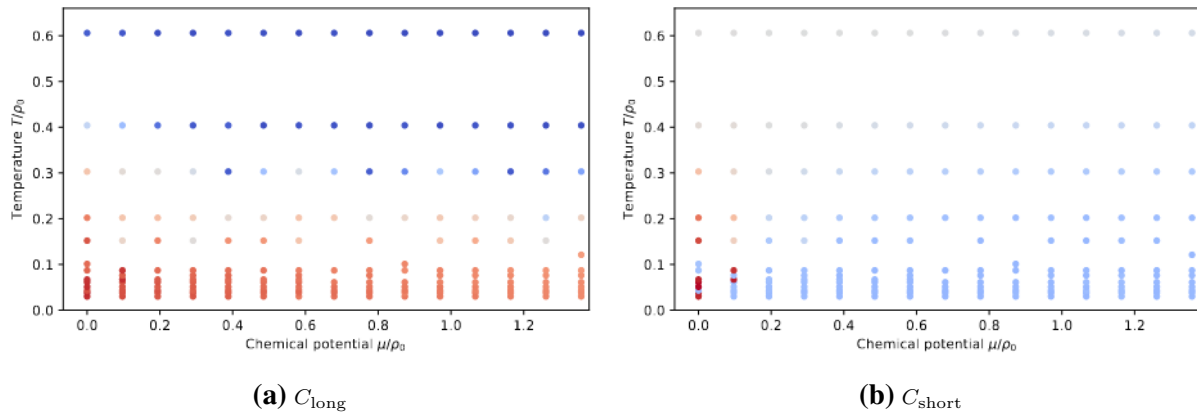


**Figure 6.10:** Finite-volume phase diagrams of the  $N_f = 8$   $\chi$ GN model as mapped out via  $C_{\text{long}}$  and  $C_{\text{short}}$  for  $(/a, a\rho_0) \approx (63, 0.41)$ . For comparability the colormaps from Fig. 6.1 resp. Fig. 6.4 are used.

general structure suggests that  $N_f$  is to be replaced by an effective  $N_f' = N_f(1 + \lambda'/2\pi N_f)$  which for the case under consideration amounts to

$$N_f' \approx 2.168, \quad 1/N_f' \approx 0.461 \quad (6.10)$$

and in general lowers the expected exponent. This trend is also seen in the extrapolated exponents as discussed above and the numerical value is of a comparable order of magnitude.

### 6.2.5 Notes on Eight Flavors

Finally, we took some samples for larger flavor number. A first glimpse of this was presented in Fig. 6.3 where the dominant wave number of the eight-flavor model was shown for comparison. Already there, we found hints of a rapid convergence to the MF result that becomes exact at  $N_f = \infty$ .

Fig. 6.10 shows the finite-volume  $C_{\text{long}}$  and  $C_{\text{short}}$  phase diagrams at  $(/a, a\rho_0) \approx (63, 0.41)$  similar to Figs. 6.1 and 6.4 for  $N_f = 8$ . One can immediately see that the qualitative conclusions from before still hold – which is only reasonable because we already found strong ties to the MF result at  $N_f = 2$  and with the current choice  $N_f = 8$  we are only moving closer. The general trend is towards more order and coherence which suggests that the approach  $N_f \rightarrow \infty$  will probably be monotonic in that regard. This is reflected in a larger temperature extent of regions with non-vanishing  $C_{\text{short}}$  and  $C_{\text{long}}$ .

## 6.3 Discrete GROSS-NEVEU Models

Due to their continuous symmetry group,  $\chi$ GN models manage to be, in a sense, only weakly inhomogeneous: While the phase of the condensate is surely position-dependent (in MF), most physically relevant quantities like, e.g., the mass gap or the baryon number density are completely homogeneous. Opposed to that, the discrete symmetry group of  $\mathbb{Z}_2$ -GN models does not

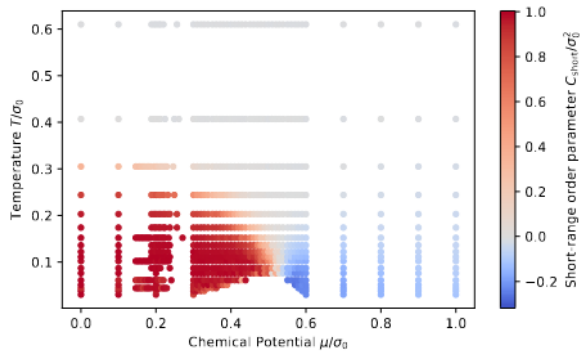


**Figure 6.11:** Finite-volume phase diagram of the  $N_f = 8 \mathbb{Z}_2$ -GN model for  $(/a, a\sigma_0) \approx (63, 0.41)$  as mapped out via  $C_{\text{short}}$ .

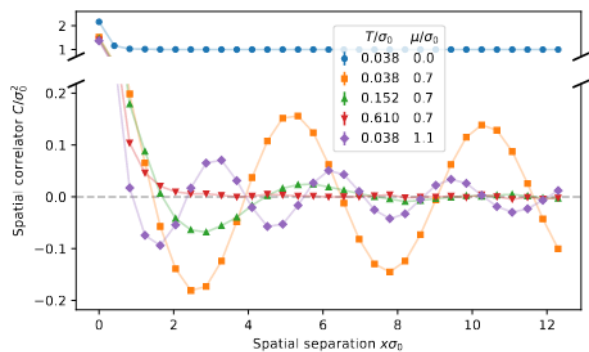


**Figure 6.12:** Representative examples of  $C$  in the  $N_f = 8 \mathbb{Z}_2$ -GN model on a  $(/a, a\sigma_0) \approx (63, 0.41)$  lattice.

allow such a homogeneity. If they are forced by a chemical potential to have a finite-particle-number equilibrium, they produce localized clumps of fermions, so-called baryons, and move them away from each other as far as possible. The CHMW Theorem 1 is not applicable at small chemical potentials due to the discrete symmetry breaking pattern and it is not straightforward to apply it to the finite density case either because of the external symmetries involved, as discussed in Section 3.3. All these properties render  $\mathbb{Z}_2$ -GN models more interesting but also more challenging.

### 6.3.1 The Finite-Volume Phase Diagram for Eight Flavors

For  $\mathbb{Z}_2$ -GN models,  $C_{\text{long}}$  is of little use because the real order parameter field has zeros whenever there exist inhomogeneities such that an inhomogeneously dominated regime could not be distinguished from a symmetrically dominated one. Therefore, we directly turn to the quantity  $C_{\text{short}}$  for a first parameter scan.

Fig. 6.11 shows the  $C_{\text{short}}$ -finite-volume phase diagram for  $(/a, a\sigma_0) \approx (63, 0.41)$ . As in  $\chi$ GN models it shows qualitatively the same structure as its MF counterpart, i.e. a homogeneously dominated regime at small temperature and chemical potential, a symmetrically dominated regime at sufficiently high temperature and an inhomogeneously dominated region at low temperature and chemical potentials larger than a threshold  $\mu_c$ . As in  $\chi$ GN models, quantitatively the respective non-trivial regions shrink due to further fluctuations working to disorder the system. It is interesting to note that just like in MF, the transition temperatures at vanishing chemical potential for  $\mathbb{Z}_2$ -GN and  $\chi$ GN models are very similar, roughly around  $T/\sigma_0 \approx 0.3$  for  $N_f = 8$  (compare Figs. 6.10b and 6.11) and  $T/\sigma_0 \approx 0.15$  for  $N_f = 2$  (see Fig. 6.4 for  $\chi$ GN and [65] for  $\mathbb{Z}_2$ -GN).

Representative correlators  $C$  for a sample of five pairs of thermodynamic parameters are shown in Fig. 6.12. They should be compared to the shapes of MF  $\sigma$  fields in Fig. 3.1b. Again, there is great qualitative agreement with basically the same distortions as described for  $\chi$ GN models. One detail worth noting is that we were not able to resolve KAK structures that are distinguishable from cosine-like condensates. While we expect this to be due to insufficiently

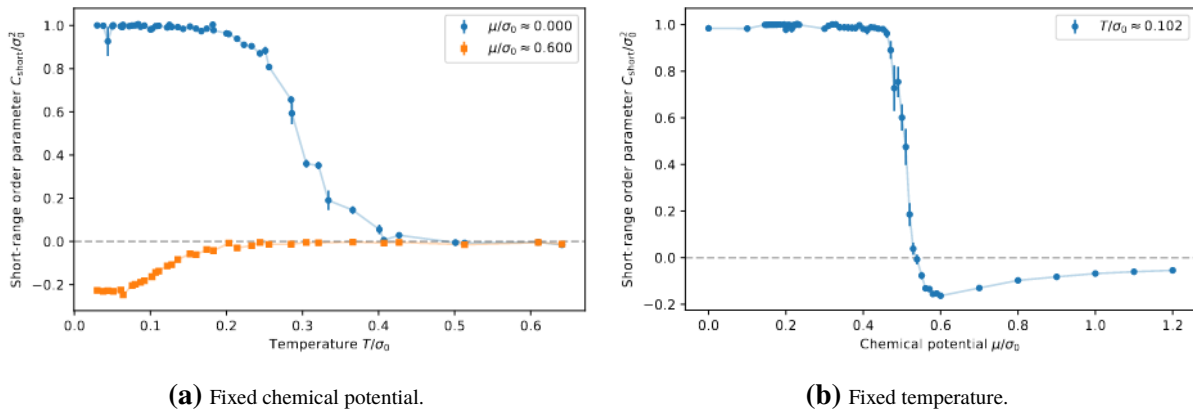


**Figure 6.13:**  $C_{\text{short}}$  in the  $N_f = 8 \mathbb{Z}_2$ -GN model on a  $(/a, a\sigma_0) \approx (63, 0.41)$  lattice in dependence of one parameter while the other is kept fix.

large system sizes, it could also be a hint that fluctuations might smoothen out these structures generically. It is also possible that this is purely an artifact of long ACTs. Further data on larger lattices would be needed to answer this question.

A more detailed way to illustrate these results is in terms of slices of Fig. 6.11 at fixed temperature or chemical potential which is shown in Fig. 6.13. At vanishing chemical potential  $C_{\text{short}}$  very accurately mimics a second-order PT, although the LANDAU-LIFSHITZ (LL) argument (Theorem 2) would forbid SSB at finite temperature. By use of cluster decomposition [160], one could again argue that at vanishing temperature  $C_{\text{short}}$  should be equivalent to the chiral condensate squared (see Eq. (6.6) and the discussion around that). We will see that this is very stable with respect to the IR limit which is due to the fact that we are working at comparably large flavor number  $N_f = 8$ .

At finite chemical potential, the temperature-dependent behavior of  $C_{\text{short}}$  is smoother but still very much resembles a phase transition. Again, as we can see by comparison with Fig. 6.12 not all data points of negative  $C_{\text{short}}$  can be interpreted as inhomogeneities on scales (at least) comparable with the system size  $L$ . Instead, in some intermediate temperature parameter region  $C_{\text{short}} < 0$  can mean again a rapid decay of oscillations. However, also in this respect the larger flavor number leads to more pronounced structures.

We could also verify that the transition between homogeneously and inhomogeneously dominated regions is smooth, as seen in Fig. 6.13b. Also, the amplitude of the inhomogeneities is much smaller than the homogeneous condensate over most of the homogeneously dominated region. This, as well as the decaying amplitude for larger chemical potentials is predicted by the MF approximation but it is much more pronounced in our simulations. Particularly, the sharp drop in amplitude around the transition is not predicted. This is probably due to the newly acquired (would-be) phonon modes that are available to induce large disordering in the inhomogeneously dominated regime.

The above findings are very stable with respect to both, the infinite-volume and the continuum limit, as seen in Fig. 6.14.<sup>50</sup>

<sup>50</sup>One should note that, while there are objectively fewer points with  $C_{\text{short}} < 0$  for larger number of lattice

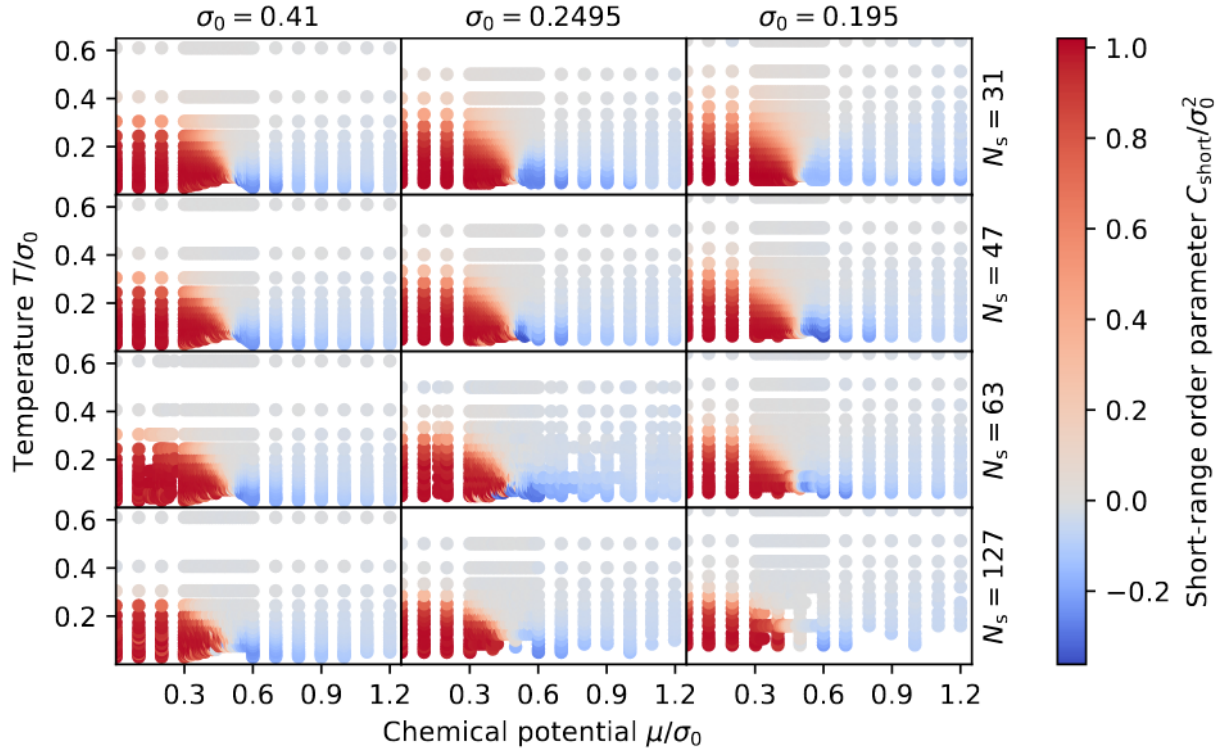


**Figure 6.14:** Finite-volume phase diagrams in the  $N_f = 8$   $\mathbb{Z}_2$ -GN model mapped out via  $C_{\text{short}}$  for various lattice sizes and spacings.

### 6.3.2 Baryonic Liquids

In  $\mathbb{Z}_2$ -GN models, as opposed to  $\chi$ GN models, a finite-density equilibrium is realized by an array of localized baryons in MF as well as in a finite volume. This can be seen in terms of  $C_{n_B}$  (see Eq. (6.2)) in Fig. 6.15b for  $(/a, a\sigma_0) \approx (63, 0.41)$  at  $(T/\sigma_0, \mu/\sigma_0) \approx (0.038, 0.7)$ . Fig. 6.15a shows the MF expectation which beautifully resembles the numerical results, Fig. 6.15b. Indeed, we find that any root of the correlator  $C$  comes with half a localized baryon. As governed by the periodic structure of  $C$ , they organize in an array maximizing the distance between nearest-neighbor (NN) baryons.

The array of baryons is stabilized by the finite volume due to the quantization of the number of oscillations analogously to the discussion of winding number discretization in Section 6.2.2. The existence of localized baryons, however, admits a heuristic interpretation of the influence of periodic boundary conditions on this: In a one-dimensional infinite chain, PEIERLS argued that stochastically independent fluctuations of the individual components' positions will add up to disorder on large scales (see the discussion in Chapter 3) [121]. The introduction of periodic boundary conditions now invalidates the assumption of independence of the fluctuations. Instead, the fluctuations repeat after the system size is exceeded and, thus, a long-range correlation is *enforced* on the system. It is this long-range correlation that stabilizes the infinite-volume baryonic liquid into a baryonic crystal in finite volume. Of course, this still admits the possibility that

---

points, this has to be attributed to our limited compute resources. The estimated-by-eye boundary between inhomogeneously dominated and symmetric regions stays roughly constant; only, it is much more computationally demanding to simulate small temperatures, i.e. large temporal extent, with more spatial points.

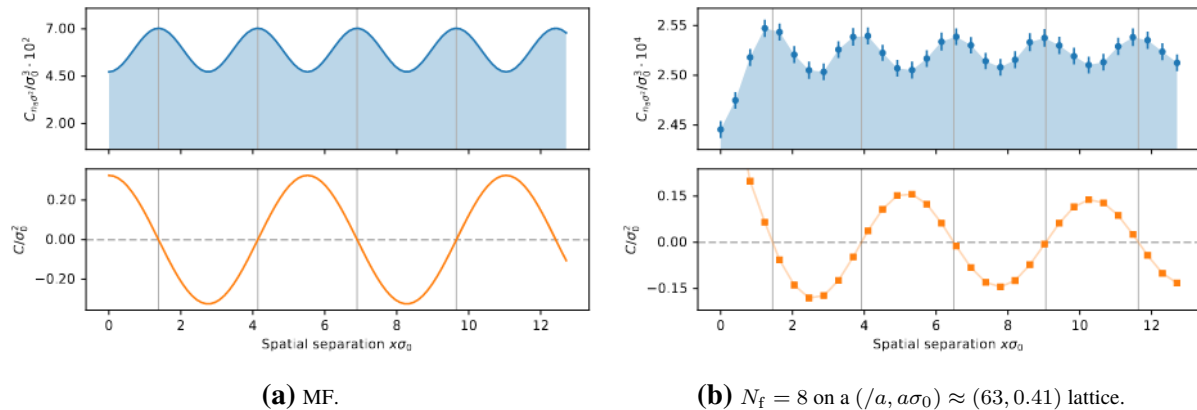


**Figure 6.15:**  $C_{n_B}$  (top) and  $C$  (bottom) in  $\mathbb{Z}_2$ -GN models at infinite and finite flavor number for  $(T/\sigma_0, \mu/\sigma_0) \approx (0.038, 0.7)$ .

correlated patches inside the given volume are small, i.e. the correlation length is much smaller than the system size  $L$ . In this case, the revival of correlations after a distance of  $/2$  would be clearly identifiable as a FS effect. Still, the putative mechanism for circumventing SSB realizes a QSL at finite temperature with diverging correlation length for vanishing temperature. So, at some sufficiently low temperature, every finite-size system would again crystallize.

The correspondence of roots of  $C$  and the baryon number is established systematically for all<sup>51</sup> chemical potentials in Figs. 6.16 and 6.17 for  $(/a, a\sigma_0) \approx (63, 0.41)$  at temperature  $T/\sigma_0 \approx 0.076$ . Fig. 6.16 shows that the sharp drop of the squared  $\sigma$ -field  $\langle \sigma^2 \rangle / \sigma_0^2$  occurs at the same value  $\mu_c$  of the chemical potential at which the baryon number rises. As we already established that at this temperature the transition happens into an inhomogeneously dominated regime, this implies that a non-vanishing baryon number is intimately related to the appearance of inhomogeneities.

It should further be noted in this figure that the baryon number at finite  $N_f = 8$  very much resembles the MF prediction qualitatively. Quantitatively, there are minor differences, e.g., the fact that  $\mu_c$  is somewhat smaller and the systematic offset in the asymptotic behavior.

Even more precisely, we can measure the dominant wave number of each configuration individually, i.e. we denote by  $\tilde{k}_{\max}$  the result of Eq. (6.3) if one pulls the application of  $\langle \cdot \rangle$  (hidden in  $C$ ) out of  $\text{argmax}$ . This results in a non-quantized version of  $k_{\max}$  that can take values not quantized to multiples of  $\pi$  realized by averaging over two (or more) commensurate cosine-like configurations.

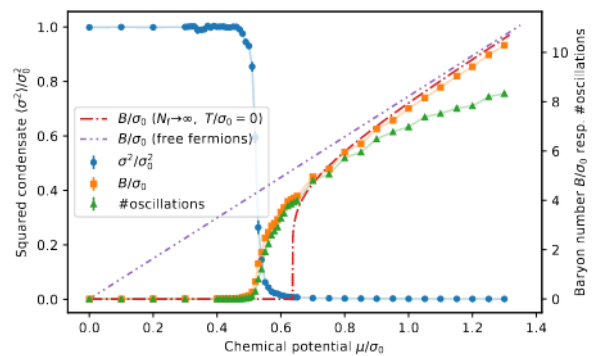


**Figure 6.16:** Baryon number in the  $N_f = 8$   $\mathbb{Z}_2$ -GN model on a  $(/a, a\sigma_0) \approx (63, 0.41)$  lattice at temperature  $T \approx 0.076$  compared to  $\langle \sigma^2 \rangle / \sigma_0^2$  and the (configuration-wise) number of oscillations.

<sup>51</sup>In the sense, that seeming deviations from this relation are explained below.

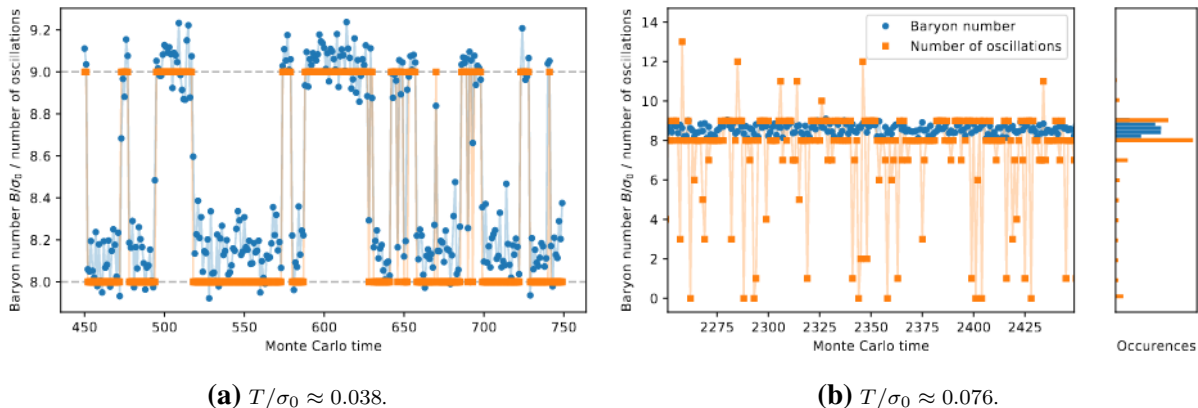


**Figure 6.17:** MC timelines of baryon number and configuration-wise number of oscillations in the  $N_f = 8$   $\mathbb{Z}_2$ -GN model on a  $(/a, a\sigma_0) \approx (63, 0.41)$  lattice at  $\mu/\sigma_0 \approx 1.1$ .

Fig. 6.16 now shows the direct correlation between the number of oscillations and the baryon number. There is excellent agreement at small and intermediate values of the chemical potential. The only minor difference between the two curves in that regime is that the baryon number seems to be a tiny amount greater than  $\tilde{k}_{\max}$  in general. We attribute this to the subtraction scheme (see Section 5.5) being only a first order correction.

This is also seen in Fig. 6.17a where besides this tiny overall offset, we find that this correspondence is realized even on the configuration-wise level. That implies that the system dominantly fluctuates between two semiclassical inhomogeneous backgrounds with only minor perturbations on top.

However, in Fig. 6.16 there is a sizable deviation for large chemical potentials. What goes wrong, is shown in Fig. 6.17b. This MC timeline at  $(T/\sigma_0, \mu/\sigma_0) \approx (0.076, 1.1)$  clearly shows that most of the configurations indeed have a very precise correlation between baryon number and dominant wave number. What spoils the final average are those configurations that due to some fluctuation coincidentally have a much smaller wave number. We regard this as rather a problem of noisy signal processing than physically relevant because the overwhelming peak of both distributions is very consistent.

### 6.3.3 A Detailed Study of the Infrared Behavior

As discussed in Chapter 3, the applicability of the CHMW theorem is still disputed in the case of  $\mathbb{Z}_2$ -GN models where the internal symmetry is only discrete. In an attempt to clarify this issue, we performed simulations on lattices up to  $N_s = 725$  with the largest lattice spacing  $a\sigma_0 \approx 0.41$  at one fixed parameter pair  $(T/\sigma_0, \mu/\sigma_0) \approx (0.030, 0.5)$ .

Fig. 6.18a shows the results for  $C$  in successively larger systems. For starters, one can see clearly that the correlators for different system sizes match quite well up to commensurability effects. That the mismatch in wave number is really only an issue of commensurability is clearly seen in Fig. 6.18b showing the FT of the same data. In general, the FTs are close to identical. However, the inset shows that  $N_s = 65, 525, 725$  have a maximum at  $k/\sigma_0 \approx 0.70$  where there

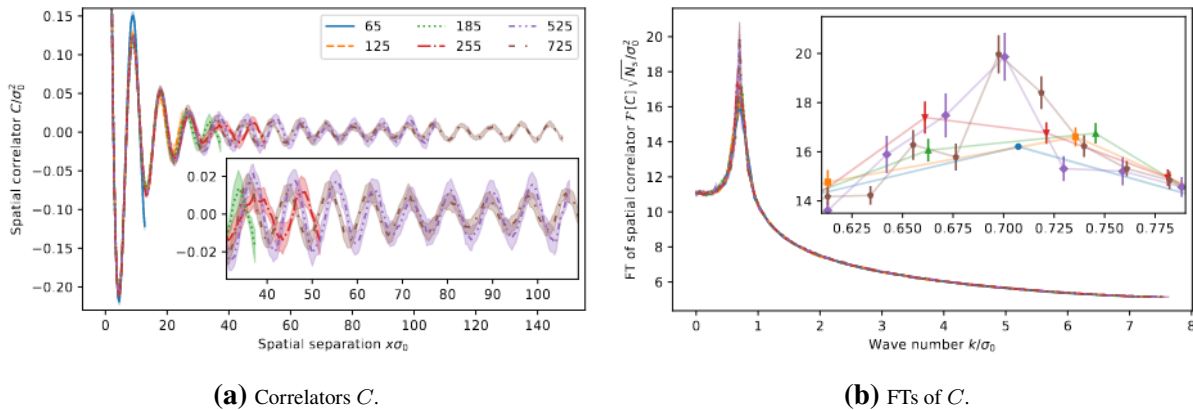
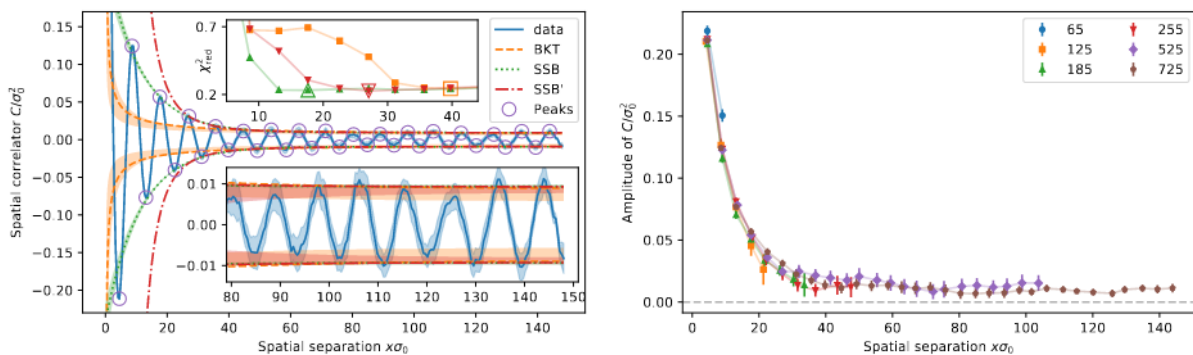


**Figure 6.18:** Correlators  $C$  and FTs thereof in the  $N_f = 2 \mathbb{Z}_2$ -GN model for  $(T/\sigma_0, \mu/\sigma_0) \approx (0.030, 0.5)$  on lattices with  $a \in \{65, 125, 185, 255, 525, 725\}$  and lattice spacing  $a\sigma_0 \approx 0.41$ .



**(a)** Detailed account of  $C$  on the largest lattice including an example for the extracted extremal values and fits to several plausible scenarios. The SSB' fit is lacking an error sleeve because the error is off the charts as soon as it leaves the fitted area. The inset shows the reduced  $\chi^2$  value for fits starting from different  $x$  values.

**(b)** Amplitude values extracted from the peaks as exemplified in Fig. 6.19a for varying number of spatial lattice points  $a$ .

**Figure 6.19:** Figures concerned with the extraction of oscillation amplitudes from  $C$  in the  $N_f = 2 \mathbb{Z}_2$ -GN model for  $(T/\sigma_0, \mu/\sigma_0) \approx (0.030, 0.5)$  at lattice spacing  $a\sigma_0 \approx 0.41$ .

are no commensurate wave numbers for the other lattices. They instead have their maxima slightly shifted to the left or right depending on which discrete FOURIER mode is closer to the optimal (infinite-volume) value.

More importantly, however, we find a small but statistically significant amplitude over the whole range of each lattice that does not seem to decrease much further in the IR. In an attempt to resolve this contradiction with the CHMW theorem which would allow for at most a rationally decaying amplitude, we will now study the long-range behavior of the data in more detail.

As opposed to  $\chi$ GN models, the extraction of the amplitude is not a trivial mathematical operation but involves advanced signal processing techniques. We use the `scipy.signal`'s `find_peaks` function<sup>52</sup> [2] to extract the extrema of the correlators as illustrated in Fig. 6.19a. These give us the amplitude<sup>53</sup> of the correlator at discrete spatial separations. The extracted values for all lattices sizes are plotted in Fig. 6.19b. Again, one can clearly see that there is a rapid

<sup>52</sup>with `prominence=0.01`

<sup>53</sup>formally only a lower bound due to the finite lattice spacing

decay of correlations for small spatial separations but in the long-range regime the amplitude never quite drops to zero and does not even show such tendency. In fact, most of the extracted long-range amplitudes are consistent with each other. To be more precise, we will make some educated guesses on how to model the amplitude behavior in the following and try to fit the models to the data.

In the case of actual SSB the amplitude would drop to a finite value while the phonon modes on top of that crystal would be NGB that are massless and have a rationally decaying correlator. We will refer to this scenario as SSB'. Thus, in this case<sup>54</sup>

$$\text{amplitude}_{\text{SSB}'}[C] = A_0 + A_1 \left[ \frac{1}{|x|^B} + \frac{1}{|-x|^B} \right] \quad (6.11)$$

for parameters  $A_0, A_1, B > 0$  to be determined by a fitting procedure, should be a reasonable description of the correlator  $C$  as soon as higher excitations die off, i.e. in the IR.

The CHMW theorem tells us that SSB' should not be possible due to the incurable IR divergences of massless modes in the system. The standard resolution to this is to restore the symmetry in the IR limit. This scenario, we call it BKT, would be realized by  $A_0 = 0$ . The reader should be aware that in this scenario there is one free parameter less to fit and thus one would generally expect this to be less flexible in describing the data. However, this scenario would also be confirmed if a fit of the SSB' yielded  $A_0 \approx 0$ .

However, it might be possible that the phonon somehow decouples from the rest of the system such that the IR divergence can be ignored. A similar scenario in closely related models where the NGBs decouples is described in [41]. There, it turns out that the condensing degrees of freedom are not actually charged under the would-be broken symmetry. After decoupling the massless mode, the leading fluctuations on top of a condensate would all be massive and for sufficiently large distances described by

$$\text{amplitude}_{\text{SSB}}[C] = A_0 + A_1 [\exp(-B|x|) + \exp(-B|-x|)]. \quad (6.12)$$

Although it is not clear how this would be physically realized for translation symmetry, in the light of CHMW theorem it is more realistic than SSB' and we will consider such a scenario as SSB in the following.

Our best attempts to fit the respective models to the  $/a = 725$  correlator data are shown in Fig. 6.19a. As the definition of IR is somewhat arbitrary without detailed knowledge of the mass spectrum of the system, we fitted the models for a varying number of points in the long-range tail of the data and used the description with minimal  $\chi^2$  value as final answer. All  $\chi^2$  values are

---

<sup>54</sup>One should note that the periodic boundary conditions induce additional contributions from crossing the boundary any number of times in both directions. The largest such contribution is included by the addition  $(x \rightarrow -x)$ . However, the further contributions  $(x \rightarrow n \pm x)$  for  $n \in \mathbb{N}$  do not sum up to a finite contribution. This problem is well-known in low-dimensional field theories. For  $B = 2$ , the so-called WEIERSTRASS elliptic function [165] provides a regularized version of such sums and any elliptic function can be expanded in terms of this function and its derivative. This theory could maybe be used (directly or as an inspiration) to write down a better behaved model for such correlations but we stick to the largest two contributions for simplicity here.

**Table 6.3:** Fit parameters for the three fits shown in Fig. 6.19a and given by Eqs. (3.15), (6.11) and (6.12). One should note that  $B$  is a mass for SSB, so we imply a correct normalization  $B/\sigma_0$ .

	$A_0/\sigma_0^2$	$A_1/\sigma_0^2$	$B$	$\chi^2$	$\sigma_0 x_{\min}$
BKT	-	0.12(7)	0.7(1)	0.254	37
SSB	$9.4(4) \cdot 10^{-3}$	0.23(3)	0.090(5)	0.232	15
SSB'	$9.1(5) \cdot 10^{-3}$	$1(2) \cdot 10^3$	3.3(5)	0.226	25

shown in Fig. 6.19a where the used one is highlighted. The corresponding values for  $A_0$ ,  $A_1$ ,  $B$  can be found in Table 6.3.

The best fit, in terms of  $\chi^2$  as well as range of applicability and stability with respect to the number of included points, is the SSB scenario. The value of the constant offset is small but statistically significantly non-vanishing which, at the same time, entails that the BKT scenario is the worst fit, not so much in  $\chi^2$  but surely in range of applicability. One should again stress that the BKT has one fewer free parameter and is therefore not expected to fit as well. Furthermore, all three fits are surely dominated by fitting the close-to-constant behavior that sets in around  $x\sigma_0 \approx 40$  and at most (for SSB) fit to a handful of significantly decaying points. This also explains why SSB and SSB' are in such excellent agreement about the constant offset.

However, it is worth noting that the exponent  $B \approx 0.66 \pm 0.13$  is reasonably close to the expected  $B = \frac{1}{2}$  for  $N_f = 2$  in case of a BKT phase. While it is not as close as in the  $N_f = 2$   $\chi$ GN model, the findings from there are similar: The BKT yielded a slightly larger exponent and the massive correlators amounted to essentially an approximation of a constant and an exponential decay on top of that. In the  $\chi$ GN model, this was predicted by PerT.

Furthermore, accounting for boundary conditions in a more reliable way would probably raise the prediction for the long-range tail of the model significantly allowing for a smaller exponent at intermediate distances.<sup>55</sup> This renders the possibility of a BKT phase at low or vanishing temperature rather plausible.

Another open question concerns the ACT of the data. While we did not find an artifact region as shown in [65] for  $N_f = 2$ , the MC timeline of the configuration-wise  $k_{\max}$  does not show any jumps after thermalization for  $N_f = 2$ . The opposite behavior was interpreted in the  $N_f = 2$   $\chi$ GN model as a further indication for a BKT phase. One could argue that the absence of such jumps is physical, in the sense of being sufficiently close to the infinite-volume limit where there would be no jumps in case of actual SSB. In any ever-so-large finite volume at finite lattice spacing we know for a fact that there are (potentially very small) contributions from all possible configurations including such with differing dominant wave numbers. In that sense, ergodicity is only truly achieved if such jumps are seen frequently<sup>56</sup> in the MC timeline. The best-founded conclusion, hence, seems to be that this question is undecidable with the available computational resources in conjunction with the algorithmic setup.

<sup>55</sup>At least, this is the case if one compares the WEIERSTRASS elliptic function (regularizing  $B = 2$ ) in comparison to a simple  $x^{-2}$  decay.

<sup>56</sup>compared to the number of configurations



# Chapter 7

## THIRRING Models in 1+2 Dimensions

By the time I joined the research group, it had already been established that 1+2D TH models do not feature  $\chi$ SB for any flavor number  $N_r \geq 2$  which contradicts a large number of previous claims. This chapter is devoted to an in-depth study of  $N_r = 1$  and an analytically continued neighborhood of it. We will clarify the status of  $N_r = 1$  as being chirally symmetric for all coupling strengths outside the LAP and in doing so discover an exotic non-symmetry-breaking PT that could allow us to construct non-trivial strongly-coupled continuum TH models. For completeness, we will start out in Section 7.1 with a small summary of previous results excluding  $\chi$ SB for  $N_r \geq 2$  and establishing parity symmetry breaking for odd  $N_f \leq 9$ . Afterwards, we will gather evidence against  $\chi$ SB in the  $N_r = 1$  TH model in Section 7.2 and instead establish the existence of the new PT in Section 7.3. This effort will culminate in a revised phase diagram of non-symmetry-breaking strongly-coupled TH models in Section 7.4. We will finally discuss some thoughts on discrepancies with concurrent studies of  $N_r = 1$  with DW fermions in Section 7.5. The reader should note that we refrain from setting a scale for these investigations because we are interested in critical behavior that is by definition scale-invariant.

### 7.1 Precursors About Other Flavor Numbers

As was discussed in Section 2.5, TH models formulated with reducible and irreducible fermions species are fundamentally different due to the non-existence of chirality in 1+2 dimensions. While an even number of irreducible flavors can be rearranged into an equivalent description in terms of reducible fermions, this is not the case for odd  $N_f$  that behave fundamentally differently.

Prior to the work in our group, there had already been a long-standing interest in 1+2D TH models. Similar to other 4FTs in 1+2D, TH models are perturbatively non-renormalizable and can only yield finite predictions in an expansion in  $1/N_f$ . As opposed to its relatives however, the MF approximation does not feature dynamical mass generation or SSB because the corresponding diagram is suppressed by FURRY's theorem [166] as the calculation in [167] shows.

This leads to the unintuitive situation that introducing *more* quantum fluctuations when decreasing  $N_f$  could actually induce *more* order through the formation of a condensate. This is quite

the opposite of the previous chapter where the suppression of fluctuations lead to a stronger and stronger tendency to (almost) condense.

While from the early days there was general consensus about the existence of a critical line in the  $1/2g_{\text{TH}}^2-N_r$  plane, predictions about its location never managed to converge until recently. Predictions for the onset of this line reached from  $N_{r,c} = 2$  to  $N_{r,c} = \infty$  coming from a variety of methods including DSEs, FRG and lattice simulations. Historical overviews of these results have been collated multiple times by now, see e.g. [69, 145].

The results to be discussed here are in stark contrast to older results. Only in recent years, a convergence of different methods is observed and the technical subtleties become apparent. FRG studies, for example, need to consider higher-order momentum contributions to be successful [30] while previous lattice studies with staggered fermions are nowadays known to give rise to TH models of KÄHLER-DIRAC fermions in the continuum [136] which are theories distinct from the one studied in this thesis. Recent studies are consistent concerning their general trend – namely that  $N_{r,c}$  is likely to be smaller than two – but disagree concerning the prediction of  $\chi\text{SB}$  in the  $N_r = 1$  TH model with a series of papers utilizing DW fermions suggesting its existence in contrast to this thesis [29, 84, 89, 136, 154, 157, 158].

SSB in TH models is hard to study on the lattice because the fermionic determinant in the vector formulation of TH models is parity/chirally symmetric for each configuration of the vector field individually [128] on a finite lattice. Only after the introduction of a small trigger source, usually a mass  $m$ , a non-vanishing chiral condensate can be measured that requires a careful extrapolation to the chiral limit ( $m \rightarrow 0$ ) after taking the thermodynamic limit ( $|\Lambda| \rightarrow \infty$ ). We will resort to this technique later on to corroborate the first hints stemming from a complementary approach working directly in the chiral limit.

This complementary approach starts by reformulating a TH model of  $N_f$  flavors via a FIERZ transformation

$$\mathcal{L}_{\text{TH}} = \bar{\psi}i \left( \not{\partial} + T + \frac{1}{2} \text{tr} T \right) \psi + \frac{N_r}{2g_{\text{TH}}^2} \left( \frac{1}{2} (\text{tr} T)^2 + \text{tr} T^2 \right), \quad \langle T_{ab} \rangle \propto \langle \bar{\psi}_a \psi_b \rangle \quad (7.1)$$

where  $T$  is a HERMITIAN (matrix) auxiliary boson field transforming as  $T \mapsto UTU^\dagger$  under a chiral transformation  $U$  from Eq. (2.13). As opposed to the vector formulation, this formulation includes all possible order parameter fields for SSB into two separate unitary groups. For even numbers of irreducible flavors, the expected  $\chi\text{SB}$  follows  $U(2N_r) \otimes \mathbb{Z}_2^P \rightarrow U(N_r) \otimes U(N_r) \otimes \mathbb{Z}_2^P$ . For an odd number of irreducible flavors, it is not possible to break the  $U(N_f) \otimes \mathbb{Z}_2^P$  in a  $\chi\text{SB}$ -like pattern and instead the relevant direction in the space of order parameters turns out to be related to parity breaking, i.e.  $U(N_f) \otimes \mathbb{Z}_2^P \rightarrow U(N_f)$ .

This formulation unfortunately has a strong SP and cannot be used for simulations. It did, however, inspire the formulation of a fermion-bag-like [129] occupation number algorithm which has been used directly for  $N_f = 1$  [96]. Furthermore, these occupation numbers allow for the reconstruction of an effective potential for the pertinent local order parameter and can be measured in other formulations like the vector formulation due to their relation to thermodynamic observ-

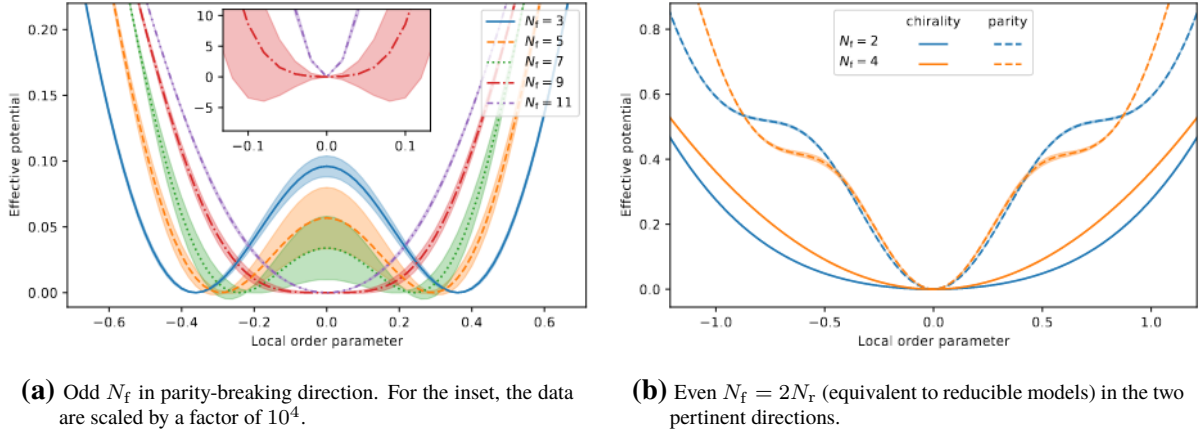


**Figure 7.1:** Effective Potential for symmetry-breaking order parameters in TH models on a  $16 \times 15 \times 15$  lattice at strong couplings outside the LAP (see values in Table 7.1). Data were produced and first used in the context of [128].

**Table 7.1:** Values of the coupling constants  $1/2g_{\text{TH}}^2$  at which the data in Fig. 7.1 were taken. For comparison, the two lattice phase transitions (LAP transition and parity-breaking transition) found in [128] are given.

$N_f$	2	3	4	5	7	9	11
LAP	0.208(4)	0.146(4)	0.112(3)	0.091(2)	0.067(1)	0.054(1)	0.045(1)
Fig. 7.1	0.214	0.154	0.114	0.098	0.070	0.054	0.050
Parity	-	0.172(2)	-	0.110(4)	0.077(1)	0.054(2)	-

ables. These developments culminated in a hybrid technique using simulations in the SP-free vector formulation with the purpose of determining the effective potential of the parity/chiral order parameter [128].

For our purposes, we only define the total lattice filling factor (LFF)

$$k = -\frac{1/2g_{\text{TH}}^2}{N_r|\Lambda|} \partial_{1/2g_{\text{TH}}^2} \ln Z(1/2g_{\text{TH}}^2) + \text{const} \propto \langle J_\mu J^\mu \rangle \quad (7.2)$$

varying between 0 and 1 but more fine-grained information is necessary for the reconstruction of all potentials. It can be shown to be exactly 1 in the LAP in the infinite-volume limit and will exactly vanish at vanishing coupling constant. It is, however, to the best of our knowledge no order parameter in the sense of (non-)vanishing if and only if SSB occurs.

Fig. 7.1 shows the effective potential in the pertinent direction for various flavor numbers of reducible and irreducible models at representative values of the coupling constants. In the irreducible models, Fig. 7.1a, one can clearly identify non-trivial global minima for  $N_f \lesssim 9$  while all reducible models, Fig. 7.1b, have their global minima at vanishing condensate. One should note that all these potentials are perfectly symmetric as it should be in the chiral limit. A detailed study in [128] determined the critical coupling constants for odd irreducible flavor numbers by examination of the curvature of the local extremum for vanishing condensate.

The same technique was also used to exclude second-order chiral PTs in reducible TH models

for all flavor numbers  $N_r \geq 2$ . Only for  $N_r = 1$  the curvature becomes very small around the transition into the LAP such that a tiny regime of  $\chi$ SB could not be fully excluded from the data. This will be subject of the following sections.

## 7.2 Absence of Chiral Symmetry Breaking

We will now focus our discussion on the case  $N_r = 1$  and a small analytically continued neighborhood around this value. In order to do so, we consider the prefactor  $N_r$  of the single-(reducible-)flavor effective action, Eq. (3.1), as a continuous parameter, allowing it to take any real value  $N_r \in [0.5, 1.1]$ .

To the best of our knowledge, the resulting theory does not describe a local QFT with a reasonable continuum limit (at least for  $N_r \notin \mathbb{N}/2$ ). Nevertheless, this approach is common in analytical studies [30, 45, 46, 83, 167–169] and was also used on the lattice before [170, 171]. The following study is instead intended to establish a non-negligible difference between the hypothetical critical flavor number  $N_{r,c}$  for  $\chi$ SB and  $N_r = 1$  in order to derive convincing conclusions about the single-flavor model.

Furthermore, it is important to realize that extrapolating to half-integer  $N_r$  does not give rise to the irreducible models as one might naively expect. This can be understood from various perspectives: Most prominently, the above procedure yields models that always have a notion of chirality and that can never break parity symmetry. More technically, the above recipe describes SP-free models for all  $N_r$  which is again different from irreducible ones. In that sense, it is closer to a phase-quenched version of the irreducible model.

### 7.2.1 The Chiral Condensate

The  $T_H$  effective action is chirally symmetric on every single vector-field configuration, so we have to trigger a chiral condensate by the introduction of a small explicit breaking of chiral symmetry. We choose this trigger to be a small mass

$$m = \frac{m_0}{\Lambda} \quad (7.3)$$

vanishing in the infinite-volume limit  $\rightarrow \infty$  with a free dimensionless parameter  $m_0 > 0$  that we will keep fixed at  $m_0 = 0.1$  during the main simulation runs later on. Qualitatively similar results to what follows were also found for smaller masses  $m_0 = 0.04$  but the ill-conditioned DIRAC operator hinders extensive studies in this parameter regime.

Before we do so, however, we show the dependence of the chiral condensate  $\Sigma$  on  $m_0$  for three lattice sizes  $N_t = 8, 12, 16$  for one representative value  $N_r = 0.70$  in Fig. 7.2a. Here and in the following, we will consider almost-cubic<sup>57</sup> lattices with  $N_t \times (N_t - 1)^2$  points unless otherwise stated. The figure shows the expected behavior in case of SSB: Due to the exact symmetry at

<sup>57</sup>in order to achieve a convenient formulation of the SLAC derivative, see [Wipf2021mns]

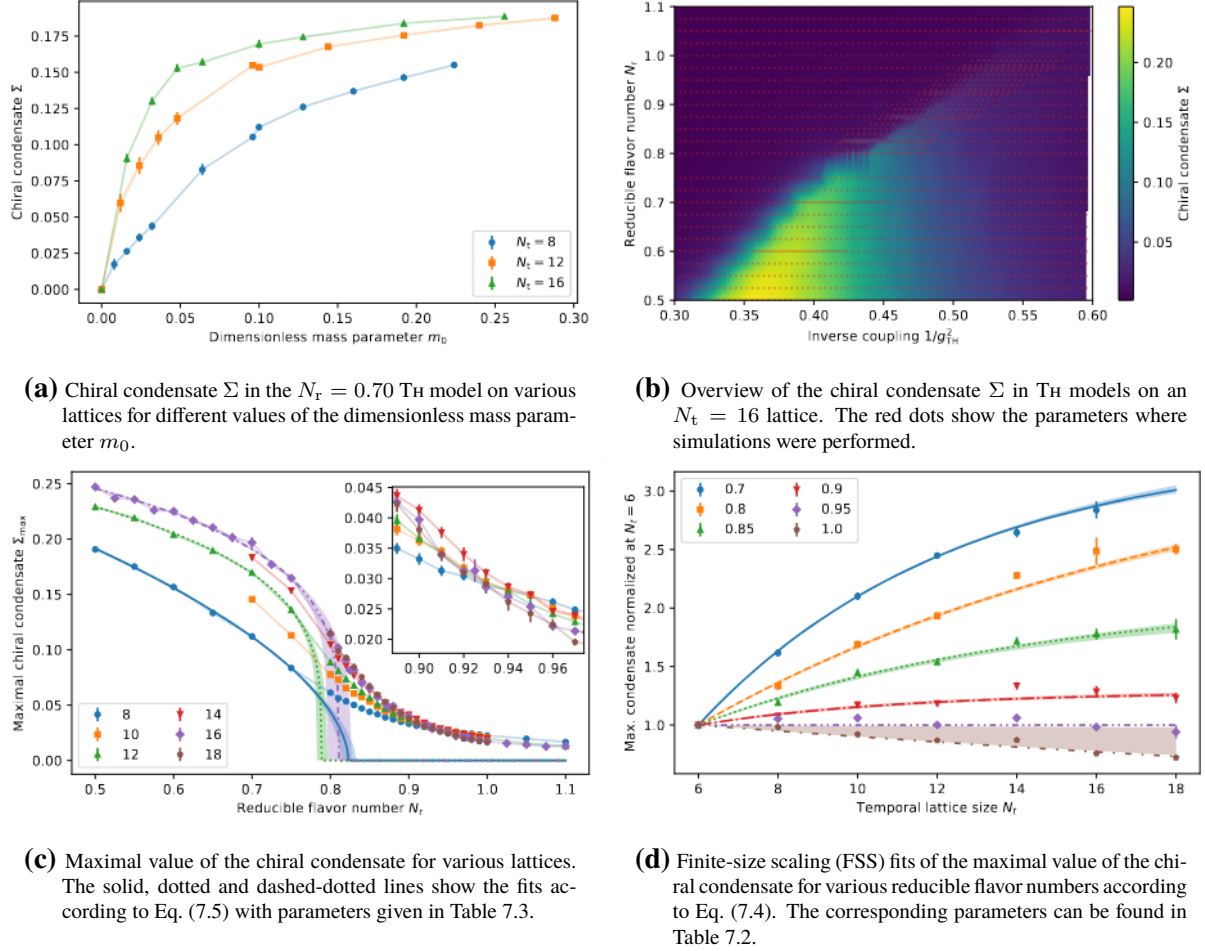


**Figure 7.2:** Chiral condensate in TH models.

$m_0 = 0$ , there is an *exactly* vanishing condensate. For small masses, it exhibits a steep rise that flattens for large masses. The features at non-vanishing mass become more distinct with increasing volume and the standard theory of SSB tells us that this will continue until the chiral condensate becomes discontinuous at  $m = 0$  for  $|\Lambda| \rightarrow \infty$  such that  $\Sigma(m \searrow 0) > 0$  whereas  $\Sigma(m = 0) = 0$ . Although on a qualitative level, this figure already establishes the fact that there exists  $\chi$ SB for sufficiently small  $N_r$ , our further investigations will show that  $N_r = 1$  is not "sufficiently small" in that regard.

Fig. 7.2b shows the chiral condensate on an  $N_t = 16$  lattice varying the two free parameters,  $N_r$  and  $1/2g_{\text{TH}}^2$ . It has a pronounced maximum at the smallest flavor number  $N_r = 0.50$  and an intermediate value of the coupling  $1/2g_{\text{TH}}^2 \approx 0.36$ . For larger coupling, i.e. smaller  $1/2g_{\text{TH}}^2$ , there is a sudden fall while reducing the coupling leads to a smooth decrease of the condensate. Increasing  $N_r$  the sudden drop wanders to smaller coupling while the rest of the features shows little change which effectively leads to a shift of the maximum to smaller couplings. At  $N_r = 1.00$ , the signal is very small compared to the maximum at  $N_r = 0.50$ . However, it still has a small maximum.

The shape of this condensate might look a little unexpected. Indeed, as discussed in Chapter 4 the non-monotonic behavior at strong coupling is due to the LAP producing the sudden drop.

**Table 7.2:** Parameter values obtained from fitting Eq. (7.4) to the data in Fig. 7.2d including the reduced  $\chi^2$ . The sign,  $S$ , was determined from the trend between the first and last data point. The  $N_r = 0.95$  data (marked with an asterisk) are basically flat and are not well described by the ansatz.

$N_r$	0.70	0.80	0.85	0.90	0.95	1.00
$B$	0.155(9)	0.08(1)	0.11(3)	0.20(7)	3*	0.03(2)
$C$	0.56(3)	0.87(3)	0.95(9)	1.4(4)	5*	0.0(7)
$\chi^2$	0.22	0.57	0.90	0.49	2.51	1.14

The smooth decay at smaller couplings is the region related to continuum physics and a first naive estimate of the onset of the LAP is given by the maximum for every fixed flavor number. This approximation is used, for example, in [29, 84, 89, 136, 154, 157, 158] while we will be more precise later on and show that this is not an adequate way to localize the transition into the LAP phase.

An upper bound for the chiral condensate for some given flavor number  $N_r$  is its maximum with respect to  $1/2g_{\text{TH}}^2$ . For various volumes, this is depicted in Fig. 7.2c. One should stress again that our definition of the mass couples the chiral limit to the infinite-volume limit such that larger volume implies approaching the chiral limit.

Qualitatively, we make the same observation as before: Increasing the flavor number quickly lowers the condensate and all volumes consistently show an inflection point around  $N_r \approx 0.80$ . Furthermore, it is clearly growing with the volume for  $N_r \leq 0.80$  which signals a symmetry-broken phase in that regime. Oppositely, it is clearly decreasing with the volume for  $N_r \geq 0.95$ . The inset shows a detailed view of the region in between. There is a reversal of the trend around  $N_r \approx 0.93$ .

The rising behavior with the volume at small flavor numbers is rapid and surely extrapolates to a non-vanishing value. Modeling the FSS in an explicitly massive system via<sup>58</sup>

$$\frac{\Sigma(N_t)}{\Sigma(N_t = 6)} = S \exp(-BN_t) + C, \quad S \in \{\pm 1\}, B, C > 0, \quad (7.4)$$

we can also conclude that the maximal condensate for  $N_r = 1.00$  extrapolates to a vanishing infinite-volume limit  $\Sigma(\infty) = C = 0.0(7)$  as seen in Fig. 7.2d and Table 7.2. In between, there is a region where such fits become unreliable because the data are close to constant and sometimes even non-monotonic. While this is strong evidence that  $N_r = 1.00$  does not show SSB, this analysis is inconclusive about its immediate neighborhood. It does not exclude the possibility that  $N_r = 1.00$  is critical.

A first hint that the critical flavor number is far below  $N_r = 1.00$  can be obtained from the following observation: The data below the inflection point<sup>59</sup> are well described by a criti-

<sup>58</sup>We excluded  $N_t = 14$  from the fits due to thermalization problems in the ensembles that would have been too expensive to overcome in a second run.

<sup>59</sup>We use  $N_r = 0.80$  for simplicity for all volumes.

cal behavior of the form

$$\Sigma(N_r) = A(N_r - N_{r,c})^\beta \quad (7.5)$$

where  $N_{r,c}$  is the critical flavor number,  $\beta$  is a critical exponent and  $A > 0$  an overall amplitude to fit to the data. The resulting values, given in Table 7.3, are largely consistent in terms of the critical flavor number

$$N_{r,c} = 0.797(6) \quad (7.6)$$

**Table 7.3:** Parameter values obtained from fitting Eq. (7.5) to the data in Fig. 7.2c including the reduced  $\chi^2$ .

$N_t$	8	12	16
$A$	0.36(1)	0.316(6)	0.327(9)
$N_{r,c}$	0.82(1)	0.789(7)	0.81(2)
$\beta$	0.56(4)	0.26(2)	0.25(3)
$\chi^2$	0.29	0.53	1.46

which we estimated as the weighted average of all three fits.<sup>60</sup> Below this value, the data are indeed very well described by Eq. (7.5) while larger  $N_r$  are inconsistent with these fits beyond the typical FS effects encountered in MC simulations. We will later see that this phenomenon is well understood after we have answered the question of what TH models above this critical flavor number look like.

As a side remark, we note that the critical exponent

$$\beta = 0.26(2) \quad (7.7)$$

is consistently fitted on the larger two lattices but far off from the first estimate as well as other values in the literature, e.g., 0.44 [46] from FRG or 1 [172] from DSEs, which are, however, themselves not very consistent across methods.

### 7.2.2 Spectral Investigations for $N_r = 0.80$ and $N_r = 1.00$

Before we turn to the broader picture, we will further strengthen the qualitative difference between the  $\chi$ SB phase for unphysically small flavor numbers and the symmetric phase that we found for  $N_r = 1.00$ . To this end, we choose two exemplary points  $(N_r, 1/2g_{\text{TH}}^2) = (0.80, 0.46)$  and  $(1.00, 0.55)$  where the respective condensate is maximal with respect to  $1/2g_{\text{TH}}^2$ .

We will first inspect the spectral density of the DIRAC operator. Via the BANKS-CASHER relation (BCR) [173], the spectrum of small eigenvalues is intimately related to  $\chi$ SB. We average the spectral density  $\rho$  over all auxiliary field configurations and arrive at the expression

$$\Sigma = \frac{2m}{|\Lambda|} \int_0^\infty \frac{\rho(E)dE}{E^2 + m^2}. \quad (7.8)$$

One can clearly see that a finite chiral condensate in the chiral limit  $m \rightarrow 0$  is only possible if  $\rho(E \rightarrow 0)$  stays finite.

<sup>60</sup>Due to the non-monotonicity of these values, an extrapolation was infeasible without more extensive data.

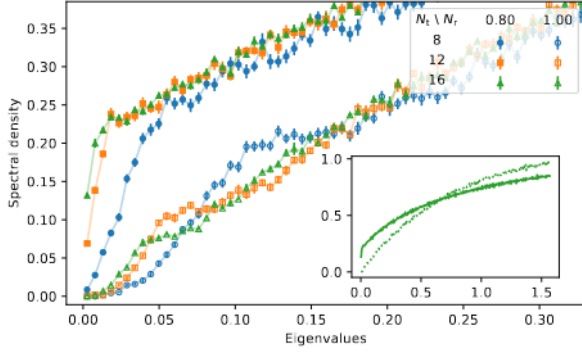


**Figure 7.3:** Spectral density according to Eq. (7.8) in 1+2D TH models with  $(N_r, 1/2g_{\text{TH}}^2) = (0.80, 0.46)$  and  $(1.00, 0.55)$  for various lattice sizes  $N_t = 8, 12, 16$ . The filled markers show the data for  $N_r = 0.80$ , the empty ones for  $N_r = 1.00$ . The inset shows in solid (dotted) lines the  $N_t = 16$ ,  $N_r = 0.80$  (1.00) data for a larger range.

Fig. 7.3 shows the spectral density for our two sample points. While the data for intermediate and large eigenvalues  $\geq 0.08$  are independent of the volume within errors in agreement with the discussion in [174], the data show a strong volume dependence in the low-energy spectrum. Indeed,  $N_r = 0.80$  – predicted to break chiral symmetry in the previous analysis – exhibits a non-vanishing and increasing spectral density around eigenvalues  $E = 0$  as necessitated by the BCR. In contrast, the low-energy spectral density stays close to zero for all volumes at  $N_r = 1.00$ .

The massless modes responsible for the above behavior of the low-energy spectrum are related to the NGBs that occur as a consequence of SSB.<sup>61</sup> In the following, we will identify and measure them directly for  $N_r = 0.80$  and show that these modes remain massive for  $N_r = 1.00$ .

In the reducible representation, there are four independent (pseudo)scalar mesons. For  $N_r = 1$ , interpolating operators at vanishing momentum are

$$\text{scalar: } M_0(t) = \sum_{x \in \Lambda_s} \bar{\psi}(t, x) \mathbb{1} \psi(t, x), \quad M_3(t) = \sum_{x \in \Lambda_s} \bar{\psi}(t, x) \gamma_* \gamma_{**} \psi(t, x), \quad (7.9)$$

$$\text{pseudoscalar: } M_1(t) = \sum_{x \in \Lambda_s} \bar{\psi}(t, x) i \gamma_* \psi(t, x), \quad M_2(t) = \sum_{x \in \Lambda_s} \bar{\psi}(t, x) i \gamma_{**} \psi(t, x). \quad (7.10)$$

As they are flavor-vector symmetric, it suffices to consider the case  $N_r = 1$ . In the reducible representation suggested in Section 2.5, the properties of the PAULI matrices turn the correlation matrix into

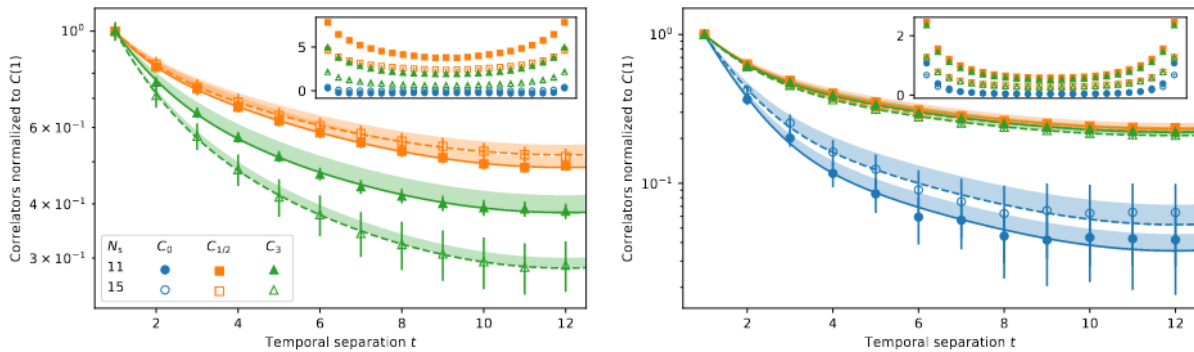
$$C_{ij}(t) = \langle M_i(t) M_j(0) \rangle_c = C_i(t) \delta_{ij} \quad (\text{no sum convention}), \quad (7.11)$$

i.e. diagonal in this operator space (see [64] for a proof of this and an explicit formula).

For a symmetric ground state in the chiral limit, one can prove that  $M_0$  transforms as a singlet under the  $U(2)$  chiral symmetry while the others form a triplet and thus  $C_1 = C_2 = C_3$ . In case of  $\chi\text{SB}$ , the  $M_3$  direction<sup>62</sup> has a non-vanishing expectation value lifting the degeneracy to  $M_1$  and  $M_2$  which, in case of SSB, become the massless NGBs. Due to the small explicit breaking, we do not expect perfect degeneracy or exactly vanishing mass but, at least, a good

<sup>61</sup>To the best of my knowledge, this is intuitive but not widely known. However, [175] derives the NGB pole as the chiral condensate which is, by use of the BCR, a direct consequence of the low-energy spectrum of the DIRAC operator.

<sup>62</sup>Remember that we redefined  $\psi \mapsto \gamma_* \gamma_{**} \psi$ , see Eq. (2.23).



(a)  $N_r = 0.80$ . The data for  $C_0$  are missing in the main plot because it is compatible with zero everywhere and cannot be normalized reliably.

(b)  $N_r = 1.00$ .

**Figure 7.4:** Temporal correlators according to Eq. (7.11) in 1+2D TH models at the representative sample points  $(N_r, 1/2g_{\text{TH}}^2) = (0.80, 0.46)$  and  $(1.00, 0.55)$ . The main plot shows the data normalized at  $t = 1$  including fits according to Eq. (7.12) over half the temporal extent with values given in Table 7.4. The inset shows  $10^4$  times the unnormalized data over the full temporal extent.

approximation. Furthermore,  $M_1$  and  $M_2$  are provably equal in our setup, see [64].<sup>63</sup>

Fig. 7.4 shows the described correlators at our two sample points for  $N_t = 24$  and  $N_s = 11, 15$ . All of them are well modeled by a double-cosh ansatz

$$C(t) = A_1 \cosh(m_1(t - N_t/2)) + A_2 \cosh(m_2(t - N_t/2)) \quad (7.12)$$

where  $A_{1/2}, m_{1/2} > 0$  are to be fitted to the data. The main figures show the data normalized for  $t = 1$ . The insets show the unnormalized data in order to emphasize when correlators are (close to) equal even beyond their masses.

This does indeed occur for  $C_{1/2} \approx C_3$  for  $N_r = 1.00$  which confirms the expected triplet structure of unbroken symmetry. The  $M_3$  meson is slightly heavier because of the small explicit mass lifting the degeneracy. The flavor singlet is heavier as can be seen from Table 7.4.

This situation is different for  $N_r = 0.80$ : As seen in the inset, the correlators  $C_{1/2}$  and  $C_3$  split up and their fitted masses are different. This is consistent with the appearance of two almost-NGB that are massless up to corrections from FS effects. The scalar meson seems to become very heavy such that  $C_0$  does not yield a non-vanishing signal for any temporal separation  $t$ .

We conclude that the spectral properties are consistent with  $\chi\text{SB}$  for  $N_r = 0.80$  but not for  $N_r = 1.00$ . The remainder of this chapter will finally present evidence against  $N_r = 1.00$  being critical.

## 7.3 The New Phase Transition

The previous sections have established the existence of a critical flavor number well below  $N_r = 1.00$ . We will now present evidence that points to an exotic previously unknown PT that

<sup>63</sup>also checked numerically

**Table 7.4:** Parameter values fitting the double-cosh ansatz Eq. (7.12) to the data depicted in Fig. 7.4. Due to the normalization, we could additionally fix  $A_1 = 1$  and only fit  $A = A_2$  afterwards, normalizing the result. For  $N_r = 0.80$  the correlator  $C_0$  was compatible with zero everywhere and could therefore not be fitted reliably.

		$N_r = 0.80$		$N_r = 1.00$		
		$C_{1/2}$	$C_3$	$C_0$	$C_{1/2}$	$C_3$
$N_s = 11$	$A \cdot 10^4$	0.05(3)	2(1)	0.4(2)	0.5(2)	0.3(1)
	$m_1$	0.1042(7)	0.110(2)	0.21(1)	0.134(2)	0.138(2)
	$m_2$	1.08(6)	0.81(5)	1.27(5)	1.03(4)	1.08(4)
	$\chi^2$	0.018	0.066	0.103	0.172	0.302
$N_s = 15$	$A \cdot 10^4$	0.2(1)	3(1)	0.4(3)	0.5(2)	1(3)
	$m_1$	0.0950(9)	0.127(2)	0.21(1)	0.128(2)	0.132(2)
	$m_2$	0.95(5)	0.82(3)	1.22(6)	1.03(3)	0.99(3)
	$\chi^2$	0.008	0.008	0.068	0.048	0.052

is – to the best of our knowledge – not related to any broken symmetry.

Fig. 7.5a shows the LFF, defined in Eq. (7.2), over a large scan in the flavor number and coupling constant. As expected, the LAP appears as a flat region  $k \approx 1$  at strong coupling that is separated by a sudden drop from a phase related to continuum physics. A comparison with the ridge in Fig. 7.2b reveals, however, that the naive expectation that the maximal condensate would follow this line is *not fulfilled*: While they indeed unite for small flavor numbers roughly below  $N_r \approx 0.80$ , the LAP transition line shows only a mild dependence on flavor numbers above  $N_r \approx 0.80$  as opposed to the position of the maximum which shifts from  $1/2g_{\text{TH}}^2 \approx 0.40$  to  $1/2g_{\text{TH}}^2 > 0.50$  while going from  $N_r = 0.80$  to  $N_r = 1.00$ .

Instead, it seems that the maximum follows a second drop of the LFF that was not studied before.<sup>64</sup> Attempting a quantitative analysis of this observation, we computed the lattice filling susceptibility (LFS)  $\chi = \partial_{1/2g_{\text{TH}}^2} k$  shown in Fig. 7.5b by numerically differentiating the  $k$  data, see Appendix A for details. In fact, Fig. 7.5b clearly shows that there is a single large peak related to the LAP transition for  $N_r = 0.60$  that, however, splits up at around  $N_r = 0.80$  and has resolved into two well-separated peaks at  $N_r = 1.00$ . One should stress again that the LAP – unambiguously signaled by  $k \approx 1$  – is to the left of the left-hand-side peak while the maximal condensate is measured slightly to the right of the right-hand-side peak (see Fig. 7.6 later on).

Another interesting property of these peaks is their volume dependence depicted in Fig. 7.5c for  $N_r = 1.00$ .<sup>65</sup> For small volumes, both peaks grow and move apart. The left peak signaling the entrance into the LAP stays rather broad while the right peak seems to sharpen with increasing

<sup>64</sup>Although it was already present in the data presented in [128].

<sup>65</sup>This analysis was refined with respect to the published one. Readers familiar with [64] should consult Appendix A for a description of the new method.

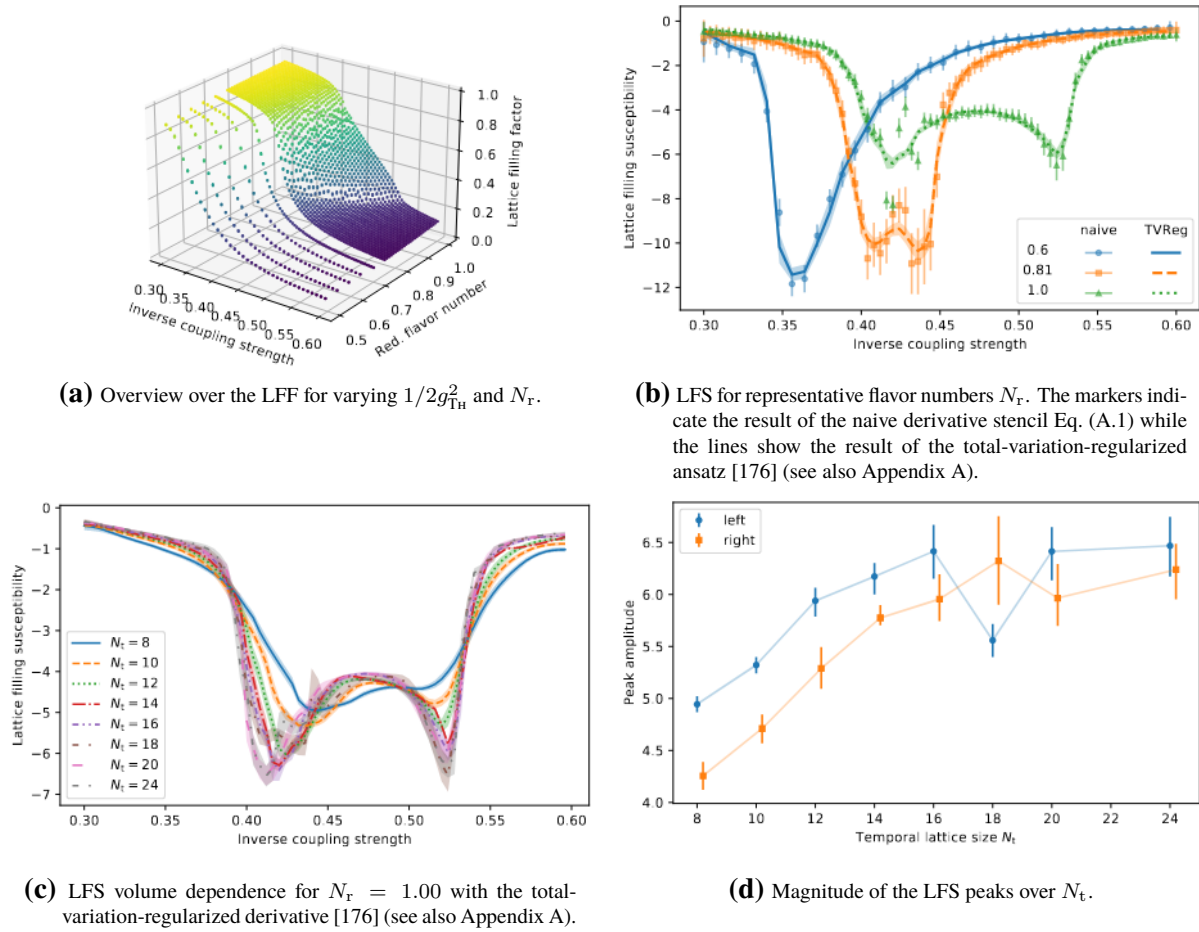


**Figure 7.5:** Figures on various aspects of the LFF and its derivative, the LFS.

volume. For large volumes, the growth becomes slow and magnitudes of the peaks seem to approach each other, see Fig. 7.5d.

Peaks of susceptibilities signal rapid changes in the physical properties of the system, often related to PTs or crossovers. While first-order PTs tend to have a peak of constant height, pertinent susceptibilities diverge at second-order PTs in an infinite volume [1]. The data of Fig. 7.5d could, thus, be interpreted as evidence for two first-order PTs because the peak height seems to become constant for large volumes. This would greatly enhance the possibility of a duality between the strong and the weak coupling regime. It would, however, disconnect a region of finite bare lattice coupling from any second-order PT where a continuum limit could be constructed.

On the other hand, the above analysis relies on a weak spot of the total-variation-regularized derivative that was used: It is particularly designed to smoothen noise while retaining as much information about qualitative features (including sharp ones as drops and peaks) as possible [176]. Still, in numerical experiments we found that the height of a sharp peak is generically underestimated. If one instead focuses on the width of the peaks, the right one becomes very sharp while the left one is and seems to stay much broader. It is therefore likely that the two PTs are qualitatively different. If so, we expect the left-hand-side one to be first-order separating the LAP from continuum physics while the right-hand-side one would probably be second order.

The latter scenario features a strongly-coupled continuum TH model that could be con-

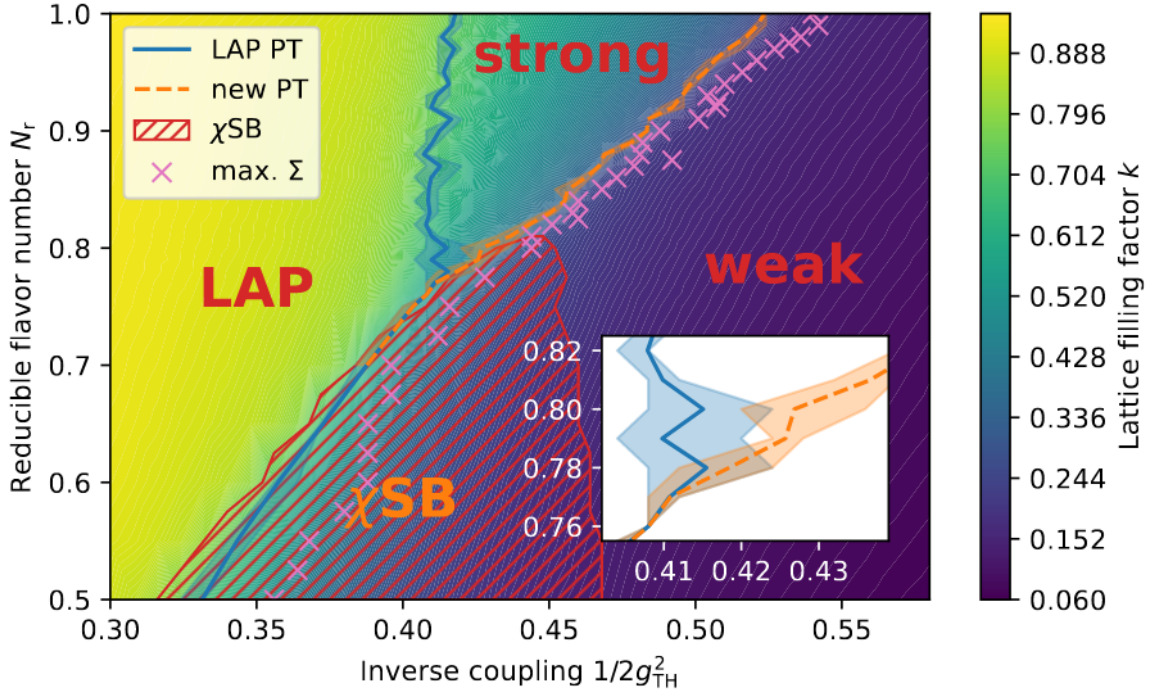


**Figure 7.6:** Rough sketch of the lattice phase diagram of 1+2D TH models in the  $1/2g_{\text{TH}}^2 - N_r$  plane on a  $N_t = 16$  lattice. The background color indicates the value of the lattice filling factor. The blue solid and orange dashed lines give the estimated positions of the transition into the LAP and the new PT, respectively. The triple point where these two transitions split up is magnified in the inset. The hatched red area indicates our conjecture where  $\chi\text{SB}$  occurs. The pink crosses show the positions of maximal (in  $1/2g_{\text{TH}}^2$ ) values of the chiral condensate.

structed from the lattice model by approaching the new transition from the left and we will assume that to be the case in the following. One should note that the present analysis comes to a slightly less conclusive result than the published one in [64] due to reasons laid out in Appendix A.

## 7.4 The Phase Diagram

The above findings suggest that the phase diagram of discretized TH models in the  $1/2g_{\text{TH}}^2 - N_r$  plane looks as sketched in Fig. 7.6. For lattice couplings exceeding a value  $g_{\text{TH,LAP}}^2$ , we find the theory in the LAP where there is no fermionic dynamics left because most of the finitely many lattice sites are blocked by interacting fermions. This phase makes up roughly the left third of Fig. 7.6 bordered by the LAP transition line. At very small coupling strength, the system's behavior is governed by a weakly-coupled FP. This phase constitutes the outer right region of the figure.

In between these two anticipated phases, we find regimes of strongly-coupled interacting physics that are probably governed by non-trivial continuum FPs. As already shown in the beginning, for sufficiently small flavor numbers we find a sizeable chiral condensate. It quickly drops for flavor numbers above  $N_r > N_{r,c} \approx 0.80$ . The remnant condensates above this value

will be understood in a way unrelated to  $\chi$ SB later on.

Unfortunately, our data lack the statistics to compute higher-order moments of the chiral condensate, e.g., a susceptibility, BINDER cumulant [177], or the like. Therefore, we have no quantitative means for estimating the transition line to the weakly-coupled region. As a rough sketch, the hatched region in Fig. 7.6 contains chiral condensates larger than 40% of the maximally measured condensate. This beautifully illustrates our conjecture for the shape and extent of the  $\chi$ SB region. But it is not a result, only a conjecture, and further computational resources would be required to map out this area precisely. We can, however, comfortably claim that any quantitative estimate of this region will stay significantly away from  $N_r = 1.00$  indicating the absence of  $\chi$ SB in all reducible 1+2D TH models.

In the small-flavor-number region discussed above, the LFS shows only a single peak. Around the triple point

$$N_{r,t} \in [0.77, 0.81], \quad 1/2g_{\text{TH},t}^2 \in [0.41, 0.43] \quad (7.13)$$

this peak splits up. The flavor range in Eq. (7.13) neatly includes the critical flavor number inferred from the chiral condensate Eq. (7.6) and we conjecture that  $N_{r,c}$  and  $N_{r,t}$  can be identified.

The only significant measurements for the chiral condensate above  $N_{r,t}$  are found to the right-hand side of the right-hand side transition. As it seems rather unlikely that the chiral condensate could show a non-monotonic behavior in a physical regime, we instead interpret this as a purely statistical artifact: Close to a second-order PT (as conjectured for this transition), fluctuations increase and govern the statistical properties of all random variables. A strictly non-negative observable like the chiral condensate is biased in this setup to larger values when fluctuations are large because there are no negative contributions to cancel positive outliers. Thus, from interpolating a monotonic behavior between the weak- and strong-coupling (but not LAP) regimes, we expect the chiral condensate to vanish even in regimes where the infinite-volume extrapolation was inconclusive or pointing to slightly positive values on our small lattices.

The 1+2D TH model of a single reducible flavor as well as its analytically continued neighborhood in the above sense instead feature a strongly-coupled phase. This phase exhibits a strong dependence of the LFF on the coupling strength without (to the best of our knowledge) breaking any symmetry. It is tempting to conjecture that the infinite-volume limit could bring the LFF down to zero in the perturbative regime which would render it an order parameter for this transition and would further allow for a simple duality to the LAP in the spirit of  $k \leftrightarrow 1 - k$ . Unfortunately, our data are not capable of supporting this conjecture, although it would be consistent as the LFF indeed shrinks with increasing volume. Much larger lattices and a dedicated scan would be needed.

The nature of the new phase and phase transition is largely unknown at the time of writing. A dedicated study is needed to explore critical exponents and physical properties. Another interesting question is what happens around the triple point  $(1/2g_{\text{TH},t}^2, N_{r,t})$ . It is mainly of academic interest because non-integer flavor numbers as used here most probably do not define a local

QFT. Still, many other methods are capable of treating  $N_f$  as a continuous parameter like FRG, DSE and large- $N_f$  expansions [30, 45, 46, 83, 167–169]. It would be interesting for methodological reasons to harmonize the descriptions of this point (including its position). Theoretically, there are three possible scenarios: The triple point and the end point for  $\chi$ SB might either coincide or allow for a gap between or an overlap of both phases. And if there are (non-integer) flavor numbers exhibiting both,  $\chi$ SB and the new phase, are they mutually exclusive, i.e. will there exist more than one PT, or do we find a regime where  $\chi$ SB occurs inside the new phase? As our data do not allow for a quantitative analysis of the  $\chi$ SB phase at this point, it would be compatible with either scenario.

## 7.5 On the Discrepancies of Modern Lattice Approaches

The above PD is still debated and concurrent studies with DW fermions do provide evidence in favor of  $\chi$ SB for  $N_f = 1$  in what is called the *bulk formulation* [29, 84, 89, 136, 154, 157, 158]. This formulation emphasizes the TH interaction as a coupling of conserved currents and sacrifices the validity of the DSE, Eq. (2.39), to this goal. It thereby loses its direct translation into a purely fermionic theory as well as its exact chiral symmetry. But it retains the conserved current that is crucial to renormalizability of the theory in the  $1/N_f$  expansion [178].

Interestingly, another formulation which was explored in early stages of said effort [89] exhibited phenomena much closer to what we found, particularly the absence of  $\chi$ SB. If one interpreted DW formulations as simply a means to construct chiral fermions, this so-called *surface formulation* directly translates the fermion-boson interaction term to the lattice by coupling the vector field to the physical fermion modes only. This vector field is no longer conserved on the lattice which is the same for our direct formulation in terms of SLAC fermions.

At the time of writing, it seems that both of these modern lattice approaches are thoroughly vetted and it is unlikely to reconcile the differences on a superficial level, e.g., by coming to new conclusions on the basis of more data. It seems more likely that the various lattice formulations are governed by different FPs, i.e., describe different continuum theories. This is also conjectured in [84] where the author describes the DW bulk formulation as closer to a gauge theory. Whether this is a desired property, depends on the very subtle question of what we actually mean by TH model. I will not attempt to answer this question here, but I will give some ideas on what the approach used in this thesis is capable of describing as a TH model.

The SLAC formulation is a superior formulation in a number of straightforward ways: It is the best approximation of the continuum dispersion relation of free fermions on a finite lattice. It retains exact chiral symmetry as well as the exact DSE Eq. (2.39). The latter point ensures that at any point in time the model can be interpreted as the purely fermionic theory it is typically written down as. Finally, on a more practical note, it is comparably easy to implement and very fast for simulations. However, beyond these very appealing properties it falls short on a more subtle level: Its non-locality is itself not immediately troublesome but still seems unnatural for

describing local QFTs and it fails to describe gauge theories completely (for reasons described in Chapter 5). Furthermore, it lacks conserved currents.

Therefore, I would conclude that the SLAC fermion formulation is capable of – and potentially the best choice for – describing a TH model as a purely fermionic theory with an exact chiral symmetry that is left intact by the strictly point-like interaction it is formulated with. This is a very explicit – maybe even superficial – interpretation of a TH model. It assumes that any other important properties these models are studied for, e.g. the interaction of conserved currents or the similarity with gauge theories, are emergent and/or coincidental phenomena and not defining properties. And, more importantly, they might *not* be emergent in this model after all if the above conjecture holds true.

Accepting this, it would be interesting to see if such a model can be constructed from our lattice action, recalling that the conserved current was a necessary condition during the renormalization in the large- $N_f$  limit, and the above PD is a first step in this direction.



# Chapter 8

## Conclusions

In this thesis, I presented our research findings on interacting fermionic models in low-dimensional spacetimes. As described in Chapter 1, these theories are not fundamentally realized in nature but emerge as models or effective theories in various branches of (quantum) physics, most prominently high-energy and condensed-matter physics.

While the main approach to study the chosen systems was lattice MC simulations, I first collated and reviewed the analytical precursors to our studies on SSB of translational invariance in and beyond low-dimensional systems. One of the main conclusions was that almost-long-range order, also known as BKT phase, is inevitable in 1+1D systems. While this seems to render such low dimensions special, I also pointed to conjectures that the resulting QSL behavior could be far more general and argued that as such the models under consideration provide a well-controlled example to study its realizations.

For 1+1D  $\chi$ GN models with small flavor numbers, our simulation results are in good agreement with analytical predictions: We have established multiple evidence supporting the claim that the finite-temperature model is in a massive phase of restored symmetry for all temperatures and chemical potentials becoming critical and turning into a BKT phase for  $T = 0$ .

These evidence include spectroscopic data (see Fig. 6.9) as well as scaling behavior of various non-local order parameters (see Figs. 6.5 to 6.8). On a qualitative level we were able to link all the features of the finite-temperature (would-be) PD to external length scales as induced by temperature, chemical potential and finite spatial extent.

That is not to say that the intriguing MF phenomena become irrelevant at finite flavor number. In contrast, even down to  $N_f = 2$  they still dominate the behavior of the system at small and intermediate length scales. This was concluded from the example correlators shown in Fig. 6.2, their linearly-in- $\mu$  increasing dominant wave number and the general shape of the finite-size (would-be) PDs. Already at  $N_f = 8$ , the behavior was hardly distinguishable from actual symmetry breaking, at least for the system sizes used in this thesis.

Furthermore, the results compiled in this thesis give valuable insight into how QSLs behave, particularly at the small and intermediate scales that are not as easily determined analytically as some asymptotic limits. We have seen how a finite system size – as it can well be realized in real-

world high-density systems – stabilizes the crystalline nature and, beyond that, how intermediate scale features like the existence of some local ordering is independent of the artificial scales of lattice extent and lattice spacing  $a$ . Given that the QSL behavior is conjectured to be applicable to a very general set of phenomena, these insights could prove useful and turn out to be a first, simple instance of a general behavior.

For 1+1D  $\mathbb{Z}_2$ -GN models, most of the above conclusions hold true. Due to the focus on  $N_f = 8$  and the additional challenges in signal processing, the evidence about the existence of SSB is less rigorous than in the  $\chi$ GN case. The same is true for the applicability of the theoretical no-go theorem. Nevertheless, the data are consistent with a massive-at-finite-temperature and BKT-at-zero-temperature scenario in accordance with the theoretical constraints. Our attempt to solidify the evidence on large lattices for  $N_f = 2$  was unfortunately inconclusive.

The new component brought into the thesis by this model was the existence of localized degrees of freedom. These localized baryons could be shown to crystallize at finite chemical potential in finite volume and are very likely to resemble the prototypical liquid much more closely than the somewhat "more homogeneous"  $\chi$ GN case. It was established that the baryon number – even configuration-wise – is tightly coupled to the number of oscillations of the condensate and that there is a preferred distance between baryons at fixed chemical potential even at finite flavor number.

Given the recent developments in higher-dimensional fermionic theories (see the review in Section 3.2), this renders it highly unlikely that purely fermionic theories are capable of breaking translational invariance even under the influence of some other form of LORENTZ-invariance breaking like a temperature and/or a chemical potential. It might still be the case that an even stronger instance of such explicit breaking could induce inhomogeneities. A first candidate, an external magnetic field, which was capable of producing inhomogeneous condensates in other effective theories [179] was recently ruled out by another study of ours [37, 38] (at least at small and moderate values of this parameter). Also, the inclusion of gauge fields could bring completely different mechanisms for such breaking.

But until such a mechanism is found the more reasonable expectation might be that crystalline phases are not fundamentally supported by QFTs without any cutoffs. This renders such scenarios less interesting for high-energy physics except for that it could exclude particularly stiff equations of state for QCD that would accompany a crystalline phase. It is less of a restriction for other branches of physics well described by QFT. In condensed matter systems, a UV as well as an IR cutoff are naturally given by the crystal's lattice spacing and the sample size, respectively, and the above considerations about strict as opposed to almost long-range order are less of a concern in these systems.

Afterwards, I turned to 1+2D TH models to discuss the long-standing issue of potential  $\chi$ SB for small flavor numbers. Building upon previous work in this group, I presented multiple evidence that no reducible TH model of integer flavor number exhibits  $\chi$ SB. To that end, we analytically continued our lattice action to non-integer flavor numbers around  $N_f = 1$ .

We indeed found a regime where direct extrapolations of the chiral condensate as well as

spectroscopic properties of the theory and spectral properties of its DIRAC operator clearly indicated a symmetry-broken phase at sufficiently strong coupling outside the LAP. This region was, however, restricted to  $N_r \lesssim 0.80$  which – to the best of my knowledge – does not describe a local QFT in the continuum limit.

The same analysis for  $N_r = 1$ , i.e. the single-flavor reducible TH model under consideration, in contrast yielded negative results. Direct extrapolation of the condensate yielded weaker but still significant decay towards zero. The eigenvalue spectrum of the DIRAC operator stays sparse around zero on average and correlation functions indicate an unbroken  $SU(2)$  triplet in the spectrum.

Instead, we found an unexpected two-peaked structure in a susceptibility that is – again to the best of our knowledge – not related to SSB. The stronger-coupling peak signalled the expected transition into the LAP, a phase where the additively renormalized  $1/2g_{\text{TH}}^2$  passed zero which is impossible in the continuum model. In that sense, it is considered purely artificial in this thesis although it is of physical relevance in other branches of physics where the lattice description is intrinsic to the problem [130, 131].

The second peak sparked the following conjecture about the PD: It might signal a second-order PT that is not related to SSB. There, a continuum TH model could be constructed that is strongly coupled but does not feature a chiral condensate. It would bypass the problem of how to construct any strongly-coupled continuum theory from this lattice action and render the ever so slight bump in the condensate that follows this peak an artifact of averaging the stronger noise expected around a second-order PT. A conjectured PD is given in Fig. 7.6.

This conjecture is at odds with other lattice formulations employing DW fermions. Following the authors of [84], I conjectured in Section 7.5 that these discrepancies could be an indication that the two formulations do not describe the same continuum theory. A dividing line between different lattice formulations could be the existence of and coupling to a conserved current. This would, in turn, raise the question why the two formulations agree so well for any higher flavor number.

Even with our expensive computer simulations, we have only scratched the surface concerning the new PT and more dedicated simulations are needed to find out more about its properties. Compared to our original publication [64] my refined analysis in this thesis was less conclusive about even the order of the PT. Further interesting information would include critical exponents to determine the universality class and the properties of the new strongly-coupled but not-symmetry-breaking phase. Such information could also inform other methods such as FRG for more dedicated studies.

The conjectured scenario implies further interesting questions: If there is an exotic PT for  $N_r = 1$ , what happens to it for larger  $N_r$ ? Does it maybe even exist in the MF approximation of infinite flavors and if not, are we once again looking for a critical flavor number?

Also, while not immediately physically relevant, several other methods such as FRG or  $1/N_r$  expansions are capable of working with non-integer flavor numbers. It would strengthen our findings if – in addition to further lattice studies – other methods could confirm the found critical

flavor number and, more interestingly, its co-location with the branching point in the LFS. In our simulations, see e.g. Fig. 7.5, the system exhibited a behavior similar to a second-order PT with respect to the flavor number. It would be interesting to confirm this and study its properties.

Finally, I observed that the analytical continuation to non-integer flavor numbers seems to be smooth. Naively, one must come to the conclusion that these theories are highly non-local due to some real exponent on the determinant in the effective action. But on the other hand, approaching  $N_r = 1$  locality apparently emerges in a manner that makes all studied observables smooth. It is a fascinating question how this non-locality vanishes. Are theories with  $N_r = 1 + \varepsilon$  only "slightly non-local" for small  $\varepsilon > 0$ ? As far as I know this question, however, has no physical relevance.

In the process of finalizing this thesis, there were further developments around 1+2D TH models that could not be accounted for with appropriate depth anymore: While not immediately asking about the critical flavor number, [180] comes to the conclusion that pure TH models lie on a first order PT line between a  $\chi$ SB and parity-breaking phase that are reached by adding a quadratic coupling of parity-condensates to the LAGRANGIAN. If this were true, it might be another explanation why different methods come to significantly different conclusions: If the discretized operators contain contaminations from such an operator, and different formulations do so in a different way, significantly differing results would be an obvious consequence. For our own results we have, however, measured neither a finite parity nor a chiral condensate beyond what we attribute to statistical noise. Either way, these results provide an interesting perspective on 1+2D TH models and might become relevant also to questions discussed in this thesis.

The results compiled in this thesis have shed a new light on purely fermionic interacting theories and contributed in various ways to a refined understanding of such. But they have also shown their limitations in the description of nature: To the best of our knowledge, fermion interactions on the fundamental level are mediated via gauge fields and their dynamics add a further level of complexity on top of the intricate phenomena discussed in this thesis. In both topical complexes studied, their lingering absence left room for interpretations and speculations about fundamental features of QFTs that need a wholesome approach to answer them. But even if at some point this wholesome approach – from lattice field theory or any other method – is available to study all these features in dynamical gauge theories, the purely fermionic view on things provides an interesting perspective to disentangle the various phenomena. And until we are at that distant point, this thesis constitutes a further example of what invaluable insights they provide.

# Appendix



# Appendix A

## Numerical Differentiation

We determined the LFS as a numerical derivative of the LFF because the direct measurement of the corresponding 8-point correlation function would have been prohibitively expensive and noisy. Derivatives can be easily approximated by finite difference stencils, the simplest of which reads

$$\partial_\lambda k(\lambda_i) = \frac{k(\lambda_{i+1}) - k(\lambda_{i-1})}{2\delta\lambda} + \mathcal{O}(\delta\lambda^2). \quad (\text{A.1})$$

This formula is linear in all  $k(\lambda_i)$  such that linear error propagation can be used to estimate the uncertainty of the resulting value up to the systematic error of order  $\mathcal{O}(\delta\lambda^2)$ .

Unfortunately, such a naive approach can be ill-behaved when applied to noisy data even if the errors seem to be rather small. This is seen in Fig. 7.5b where the markers show significant fluctuations despite the rather smooth appearance of the data in Fig. 7.5a. This problem is well-known in the literature and a plethora of regularization methods have been proposed.

Here, we apply the so-called total-variation regularized differentiation [176] via the implementation [181]. Instead of computing an approximation of the derivative directly, it integrates the latter and compares it to the original values. During the iteration towards an optimal solution, a regulator term can be applied to smooth out the amplified noise. A slightly more detailed version of this description can be found in [64].

In replicating the analysis from [64], I found that the result of this differentiation is sensitive to the given values of  $k$  beyond the level of precision provided by the measurements. Therefore, instead of using the values as-is, I repeated the analysis a large number of times while resampling the values of  $k$  from a GAUSSIAN distribution with width determined from their uncertainty. The average and 68% percentiles of this ensemble provide a smoother and statistically sounder estimate of the susceptibility and its uncertainty. The lines given in the original paper [64] are understood as one – in some parts rather exceptional – sample in this ensemble and some conclusions had to be weakened.



# Appendix B

## Parameters and Ensembles

This appendix provides a summary of the parameters used for the simulations and the resulting ensembles. A machine-readable and complete list of parameters is provided in the supplementary material [63].

### B.1 Chiral GROSS-NEVEU Models

The bulk of the simulations was performed to map out the  $N_f = 2$  PD in the  $\mu$ - $T$  plane. We simulated three different spatial extents at the largest lattice spacing and aimed for keeping a constant physical volume while lowering the lattice spacing in producing further ensembles with smaller lattice spacings. As we improved our method of scalesetting after the fact, the determined lattice spacings changed and the volumes do not precisely match up. These choices as well as the additional  $N_f = 8$  lattice setup are summarized in Table B.1.

For each of these spatial lattices we simulated at evenly spaced values of positive chemical potential starting at 0 as well as on a variety of different temporal extents to map out the temperature axis. These temperature and chemical potential grids are summarized in Table B.2.

In addition to the above, we took additional samples for specific purposes such as scalesetting and checks of thermalization/autocorrelation behaviour. In particular, the previously described ensembles all used the freeze-out method for the initial conditions.<sup>66</sup> Other methods we used are a hot start, cold start or the inverse of freezing-out, i.e., heat-up method. Descriptions of these can be found in [42]. These exceptional ensembles are sketched out in Table B.3.

The defaults for further technical parameters can be found in Table B.4. The trajectory length varied between 1.0 and 2.4 with at least 10 but up to 18 integration steps per trajectory depending on parameter details like lattice size and temperature.

---

<sup>66</sup>Except for  $63_{\text{large}}^8$  which used independent hot starts throughout all simulations.

**Table B.1:** Summary of (spatial) lattice setups on which  $\chi$ GN model ensembles were generated.

ID	$N_f$	$N_s$	$1/2g_{\chi\text{GN}}^2$	$a\rho_0$	$\rho_0$
$63_{\text{large}}^2$	2	63	1.0540	0.4566(6)	28.77(4)
$127_{\text{large}}^2$	2	127	1.0540	0.458(1)	58.2(1)
$255_{\text{large}}^2$	2	255	1.0540	0.457(1)	116(3)
$127_{\text{medium}}^2$	2	127	1.3895	0.194(3)	24.6(4)
$255_{\text{small}}^2$	2	255	1.8254	0.08(1)	49(3)
$63_{\text{large}}^8$	8	63	5.1013	0.4124(2)	25.98(1)

**Table B.2:** Overview of external parameters simulated per lattice setup in  $\chi$ GN models. The lattices are identified via their ID from Table B.1. All numerical values are given in lattice units.

ID	$N_t$ [min/max]	$\delta\mu$	$\mu_{\text{max}}$
$63_{\text{large}}^2$	2 / 72	0.04	0.60
$127_{\text{large}}^2$	2 / 72	0.04	0.60
$255_{\text{large}}^2$	2 / 72	0.04	0.60
$127_{\text{medium}}^2$	4 / 144	0.02	0.30
$255_{\text{small}}^2$	8 / 144	0.01	0.15
$63_{\text{large}}^8$	4 / 80	0.04	0.60

**Table B.3:** Overview over exceptional parameter settings for  $\chi$ GN models with a given motivation. If applicable, an ID is given as a basis with potential changes as stated.

ID	changes	motivation
$63_{\text{large}}^2$	hot start & cold start	full PD mapped out to exclude bias due to initial conditions
$127_{\text{large}}^2$	hot start & heating-up method for $\mu = 0.2, 0.4, 0.6$	exclude hysteresis effects due to initial conditions
$63_{\text{large}}^2$	$N_t = 96, 144$ at $\mu = 0.0$	scalesetting
$127_{\text{medium}}^2$	$N_t = 192, 240$ at $\mu = 0.0$	scalesetting
$255_{\text{small}}^2$	$N_f = 576, 648$ at $\mu = 0.0$	scalesetting (largest $N_t$ did not reach sufficient statistics)
$63_{\text{large}}^2$	$N_s = 31, 45, 91, 181, 361, 511, 1025$ at $\mu = 0.0$ and $N_t = 48, 72$	probing thermodynamic limit
-	$N_s = 63, N_t = 64, \mu = 0.0$ with varying $1/2g_{\chi\text{GN}}^2$	scalesetting

**Table B.4:** Defaults for various technical parameters in our  $\chi$ GN model simulations. These represent the vast majority of ensembles. For individual parameter combinations adjustments were made as can be retraced in the supplementary material [63].

parameter	value	description
$N_{\text{pf}}$	$N_f$	Number of pseudofermions
$N_{\text{remez}}$	(10, 20)	Number of terms in the Remez approximation (see Section 4.1) used for force and acceptance step respectively
spectral bounds	$[(10^{-4}, 50), (10^{-5}, 100)]$	Spectral range over which the Remez approximation is fitted again for force and acceptance
HMC integrator	3	Order of the integrator in the HMC
# trajectories/config	10	Number of HMC trajectories between two measurements

**Table B.5:** Summary of (spatial) lattice setups on which  $\mathbb{Z}_2$ -GN model ensembles were generated.

ID	$N_f$	$N_s$	$1/2g_{\mathbb{Z}_2\text{-GN}}^2$	$a\rho_0$	$\rho_0$
$(N_s)_{\text{large}}^8$	8	31, 47, 63, 127	5.2	0.4100(5)	12.71(1), 19.27(2), 25.83(3), 52.07(6)
$(N_s)_{\text{medium}}^8$	8	31, 47, 63, 127	6.3	0.2495(5)	7.73(2), 11.73(2), 15.72(3), 31.69(6)
$(N_s)_{\text{small}}^8$	8	31, 47, 63, 127	6.85	0.195(5)	6.0(2), 9.2(2), 12.3(3), 24.8(6)
$63_{\text{large}}^2$	2	63	1.022	0.4100(5)	25.83(3)

**Table B.6:** Overview of external parameters simulated per lattice setup  $\mathbb{Z}_2$ -GN models. The lattices are identified via their ID from Table B.5. All numerical values are given in lattice units. The marked (\*) value applies only to  $N_s \leq 63$ ;  $N_s = 127$  was only simulated up to  $\mu = 0.390$ .

ID	$N_t$ [min/max]	$\delta\mu$	$\mu_{\text{max}}$
$(N_s)_{\text{large}}^8$	4 / 80	0.0410	1.845
$(N_s)_{\text{medium}}^8$	4 / 80	0.02495	1.123
$(N_s)_{\text{small}}^8$	4 / 80	0.0195	0.877*
$63_{\text{large}}^2$	4 / 80	0.0410	1.845

## B.2 Discrete GROSS-NEVEU Models

The bulk of the simulations was performed to map out the  $N_f = 8$  PD in the  $\mu$ - $T$  plane. The larger flavor number was chosen in order to compare with naive fermions that are incapable of simulating lower flavor numbers without a SP. We simulated four different numbers of spatial lattice points at three different lattice spacings. A visual overview can be obtained from Fig. 6.14. Additional exploratory simulations of the  $N_f = 2$  PD were performed. These choices are summarized in Table B.5. All of these were simulated from independent hot starts.

For each of these spatial lattices we simulated at least at evenly spaced values of positive chemical potential starting at 0 as well as on a variety of different temporal extents to map out the temperature axis. These temperature and chemical potential grids are summarized in Table B.6. As this model was studied first chronologically, there was more experimentation and exploration and there is a significant number of additional sample points in parameter space. I refer the reader to the supplementary material for all the details [63], some of which can be inferred from the irregularities in Figs. 6.11 and 6.14.

In addition to the above, we took additional samples for specific purposes such as scale setting and checks of thermalization/autocorrelation behaviour. These exceptional ensembles are sketched out in Table B.7.

The defaults for further technical parameters can be found in Table B.8.

**Table B.7:** Overview over exceptional parameter settings for  $\mathbb{Z}_2$ -GN models with a given motivation. If applicable, an ID is given as a basis with potential changes as stated.

ID	changes	motivation
$63_{\text{large}}^2$	$N_s = 65, 125, 185, 255, 375, 525, 725,$ $N_t = 80$	exploration of thermodynamic limit due to initial conditions
$63_{\text{large}}^8$	cold start for $N_t = 32, 64$	investigation of hysteresis effects
-	$N_f = 4, 16, N_s = 63$ for $\mu = 0.0$	exploration of $N_f$ dependency
-	$N_f = 2, 4, 8, 16, N_t = 64$ (and more), $\mu = 0.0$ , varying $1/2g_{\mathbb{Z}_2\text{-GN}}^2$	scalesetting

**Table B.8:** Defaults for various technical parameters for our  $\mathbb{Z}_2$ -GN model simulations. These represent the vast majority of ensembles. For individual parameter combinations adjustments were made as can be retraced in the supplementary material [63].

parameter	value	description
$N_{\text{pf}}$	$N_f$	Number of pseudofermions
$N_{\text{remez}}$	(10, 20)	Number of terms in the Remez approximation (see Section 4.1) used for force and acceptance step respectively
spectral bounds	$[(10^{-2}, 200), (10^{-4}, 200)]$	Spectral range over which the Remez approximation is fitted again for force and acceptance
HMC integrator	3	Order of the integrator in the HMC
# trajectories/config	10	Number of HMC trajectories between two measurements
HMC trajectory length	3.6	-
HMC #integration steps	12	... per trajectory

### B.3 THIRRING Models

This project was ongoing in the group when I joined. The data for  $N_r \geq 2$  as well as all irreducible flavor numbers were directly taken over from [128] and I refer the interested reader to that publication for details about this part of the data.

The data this thesis is focussed on are concerned with the analytic continuation around  $N_r = 1$ . For most of the runs we used quasi-cubic lattices with  $N_t = N_s + 1$  and we will imply this whenever only one (usually  $N_t$ ) is stated.

We started our simulations with an exploration of the influence of the small trigger mass on three lattices  $N_t = 8, 12, 16$  for mass values

$$m_0 = 0.00, 0.01, \dots, 0.04, 0.08, \dots, 0.28. \quad (\text{B.1})$$

When data from other runs were available, they were also included into Fig. 7.2a. As mentioned in the main text, all following simulations were performed at fixed  $m_0 = 0.01$  from Eq. (7.3).

Next, we performed an overview scan of the chiral condensate on the  $N_t = 16$  lattice. We used a regular grid of coupling strengths and flavor numbers with steps of 0.04 in inverse coupling strength and 0.05 in flavor number.

This overview informed a refined scan on lattice of the sizes  $N_t = 6, 8, \dots, 18$  with a  $N_r$ -dependent window in inverse coupling strength and steps of 0.01 in  $N_r$ . The window was shifted in a manually tuned step-wise linear fashion to follow the maximum and can be seen in Fig. 7.2b as red dots.

A summary of these scans is given in Table B.9. They were used to create the Figs. 7.2 and 7.6. The remaining investigations at individual points in parameter space are already clearly labeled in the main text.

Concerning the LFF, we performed additional simulations on larger lattices. Concretely, we used  $N_t = 8, 10, \dots, 24$  for  $N_r = 1$ , scanning in  $1/2g_{\text{TH}}^2$  with step size 0.004 in order to produce Figs. 7.5c and 7.5d.

The defaults for further technical parameters can be found in Table B.10.

**Table B.9:** Summary of ensembles generated for scanning the PD of  $T_H$  models. The asterisk means that there is a sliding window following the maximum of the condensate as described in the text.

$N_t$	$N_r$	$1/2g_{TH}^2$	purpose
8,12,16	0.70	0.418	mass dependence, see Eq. (B.1) and Fig. 7.2a
16	0.50,...,1.10	0.300,...,0.600	condensate overview (Fig. 7.2b)
6,...,18	0.80,...,1.0	*	scan for maximum (Fig. 7.2)

**Table B.10:** Defaults for various technical parameters for our  $T_H$  model simulations. These represent the vast majority of ensembles. For individual parameter combinations adjustments were made as can be retraced in the supplementary material [63].

parameter	value	description
$N_{pf}$	4	Number of pseudofermions
$N_{remez}$	(10, 25)	Number of terms in the Remez approximation (see Section 4.1) used for force and acceptance step respectively
spectral bounds	$[(10^{-4}, 1000), (10^{-5}, 1000)]$	Spectral range over which the Remez approximation is fitted again for force and acceptance
HMC integrator	3	Order of the integrator in the HMC
# trajectories/config	10	Number of HMC trajectories between two measurements
HMC trajectory length	1.8	-
HMC #integration steps	12	... per trajectory



# Appendix C

## Data Availability Statement and Technical Acknowledgements

The fully automated analysis workflow is available in Ref. [63] and includes pointers to the full data release. Raw data and the simulation code for generating the configurations are available upon request and I will include pointers to public versions of these into the metadata of [63] if it becomes feasible to share these more widely. For a recent review on open science in the context of lattice QFT see [182].

The simulations for this thesis were performed using a C++ simulation framework originally developed in the context of [127]. From the scientific ecosystem, it leverages [126, 183–185].

The analysis workflow is Python-based [186], explicitly importing [2, 187–191].



# Acronyms

<b><math>\mathbb{Z}_2</math>-GN</b> discrete GROSS-NEVEU	<b>IR</b> infrared
<b><math>\chi</math>SB</b> chiral symmetry breaking	<b>KAK</b> kink-antikink
<b><math>\chi</math>GN</b> chiral GROSS-NEVEU	<b>LAP</b> lattice artifact phase
<b><math>\chi</math>spiral</b> chiral spiral	<b>LFF</b> lattice filling factor
<b>GN</b> GROSS-NEVEU	<b>LFS</b> lattice filling susceptibility
<b>NJL</b> NAMBU-JONA-LASINIO	<b>LL</b> LANDAU-LIFSHITZ
<b>Th</b> THIRRING	<b>LO</b> leading order
<b><math>1+nD</math></b> $1+n(-)$ dimension(al/s)	<b>LOFF</b> LARKIN-OVCHINNIKOV-FULDE-FERRELL
<b>4FT</b> four-FERMI theory	<b>MC</b> Monte Carlo
<b>AC</b> autocorrelation	<b>MF</b> mean-field
<b>ACF</b> AC function	<b>NGB</b> NAMBU-GOLDSTONE boson
<b>ACT</b> AC time	<b>NN</b> nearest-neighbor
<b>BCR</b> BANKS-CASHER relation	<b>PD</b> phase diagram
<b>BCS</b> BARDEEN-COOPER-SCHRIEFFER	<b>PerT</b> perturbation theory
<b>BKT</b> BEREZINSKI-KOSTERLITZ-THOULESS	<b>PT</b> phase transition
<b>CHMW</b> COLEMAN-HOHENBERG-MERMIN-WAGNER	<b>QCD</b> quantum chromodynamics
<b>DOF</b> degree of freedom	<b>QED</b> quantum electrodynamics
<b>DSE</b> DYSON-SCHWINGER equation	<b>QFT</b> quantum field theory
<b>DW</b> domain-wall	<b>QM</b> Quark-Meson
<b>EOM</b> equation of motion	<b>QSL</b> quantum-spin liquid
<b>FP</b> fixed point	<b>rHMC</b> rational HMC
<b>FRG</b> functional renormalization group	<b>SLAC</b> Stanford Linear Accelerator Center
<b>FS</b> finite-size	<b>SP</b> sign problem
<b>FSS</b> finite-size scaling	<b>SSB</b> spontaneous symmetry breaking
<b>FT</b> FOURIER transform	<b>TN</b> tensor network
<b>HMC</b> hybrid MC	<b>UV</b> ultraviolet
<b>HS</b> HUBBARD-STRATONOVICH	



# List of Figures

3.1	MF PDs and example configurations of $\mathbb{Z}_2$ -GN and $\chi$ GN models in 1+1D. . . . .	21
6.1	Finite-volume phase diagram of the $N_f = 2$ $\chi$ GN model for $(/a, a\rho_0) \approx (63, 0.46)$ as mapped out via $C_{\text{long}}$ . The gray line indicates the large- $N_f$ critical line. On the left, histograms of the spacetime-averaged $\Delta$ in the complex plane are shown for the temperatures $T/\rho_0 \in \{0.030, 0.091, 0.183, 0.274\}$ . The colormap is linear in the blues and in the reds but with different slopes changing at 0.05 which is considered as a reasonable threshold for noise. The green dashed lines show the thresholds $L/\xi_\beta = 2, 3, 4$ for later reference (Section 6.2.2). The given colormap will be used for all $C_{\text{long}}$ plots in this thesis. . . . .	47
6.2	Representative examples of $C$ in the $N_f = 2$ $\chi$ GN model on a $(/a, a\rho_0) \approx (63, 0.46)$ lattice. . . .	48
6.3	Dominant winding number from Eq. (6.3) for flavor numbers $N_f = 2, 8, \infty$ . The figure shows simulation data (markers), fitted slope (dashed) and fitted staircase (solid) with $T \approx 0.030$ for $N_f = 2, 8$ on $(/a, a\rho_0) \approx (63, 0.46)$ resp. $(/a, a\rho_0) \approx (63, 0.41)$ . The values for the fits are given in Table 6.1. . . . .	48
6.4	Same as Fig. 6.1 but with $C_{\text{short}}$ instead of $C_{\text{long}}$ . In this case, the green dashed lines indicate $\log_2(\lambda_{\chi S}/\xi_\beta) = 1, 2, 3$ . The given colormap will be used for all $\chi$ GN $C_{\text{short}}$ plots in this thesis. . . . .	50
6.5	Finite-volume phase diagrams of the $N_f = 2$ $\chi$ GN model for successively smaller lattice spacings with approximately constant lattice volume as mapped out via $C_{\text{long}}$ . For comparability the colormap from Fig. 6.1 is used for all plots. . . . .	53
6.6	Same as Fig. 6.5 but with $C_{\text{short}}$ instead of $C_{\text{long}}$ . For comparability the colormap from Fig. 6.4 is used for all plots. . . . .	53
6.7	Finite-volume phase diagrams of the $N_f = 2$ $\chi$ GN model for successively doubled system size at approximately constant lattice spacing as mapped out via $C_{\text{long}}$ and zoomed into the relevant low-temperature region. For comparability the colormap from Fig. 6.1 is used for all plots. . . . .	54
6.8	Same as Fig. 6.7 but with $C_{\text{short}}$ instead of $C_{\text{long}}$ . For comparability the colormap from Fig. 6.4 is used for all plots. . . . .	54
6.9	Physically relevant parameters extracted from fits to temporal correlators for all available lattice setups as described in the text. The parameter tuple in the legends is of the form $(N_f, /a, a\rho_0)$ . The corresponding fit parameters are found in Table 6.2. The fit range is indicated by the extent of the dashed lines. . . . .	55
6.10	Finite-volume phase diagrams of the $N_f = 8$ $\chi$ GN model as mapped out via $C_{\text{long}}$ and $C_{\text{short}}$ for $(/a, a\rho_0) \approx (63, 0.41)$ . For comparability the colormaps from Fig. 6.1 resp. Fig. 6.4 are used. . . . .	57
6.11	Finite-volume phase diagram of the $N_f = 8$ $\mathbb{Z}_2$ -GN model for $(/a, a\sigma_0) \approx (63, 0.41)$ as mapped out via $C_{\text{short}}$ . . . . .	58
6.12	Representative examples of $C$ in the $N_f = 8$ $\mathbb{Z}_2$ -GN model on a $(/a, a\sigma_0) \approx (63, 0.41)$ lattice. . . . .	58
6.13	$C_{\text{short}}$ in the $N_f = 8$ $\mathbb{Z}_2$ -GN model on a $(/a, a\sigma_0) \approx (63, 0.41)$ lattice in dependence of one parameter while the other is kept fix. . . . .	59

6.14	Finite-volume phase diagrams in the $N_f = 8 \mathbb{Z}_2$ -GN model mapped out via $C_{\text{short}}$ for various lattice sizes and spacings. . . . .	60
6.15	$C_{n_B}$ (top) and $C$ (bottom) in $\mathbb{Z}_2$ -GN models at infinite and finite flavor number for $(T/\sigma_0, \mu/\sigma_0) \approx (0.038, 0.7)$ . . . . .	61
6.16	Baryon number in the $N_f = 8 \mathbb{Z}_2$ -GN model on a $(/a, a\sigma_0) \approx (63, 0.41)$ lattice at temperature $T \approx 0.076$ compared to $\langle \sigma^2 \rangle / \sigma_0^2$ and the (configuration-wise) number of oscillations. . . . .	61
6.17	MC timelines of baryon number and configuration-wise number of oscillations in the $N_f = 8 \mathbb{Z}_2$ -GN model on a $(/a, a\sigma_0) \approx (63, 0.41)$ lattice at $\mu/\sigma_0 \approx 1.1$ . . . . .	62
6.18	Correlators $C$ and FTs thereof in the $N_f = 2 \mathbb{Z}_2$ -GN model for $(T/\sigma_0, \mu/\sigma_0) \approx (0.030, 0.5)$ on lattices with $/a \in \{65, 125, 185, 255, 525, 725\}$ and lattice spacing $a\sigma_0 \approx 0.41$ . . . . .	63
6.19	Figures concerned with the extraction of oscillation amplitudes from $C$ in the $N_f = 2 \mathbb{Z}_2$ -GN model for $(T/\sigma_0, \mu/\sigma_0) \approx (0.030, 0.5)$ at lattice spacing $a\sigma_0 \approx 0.41$ . . . . .	63
7.1	Effective Potential for symmetry-breaking order parameters in TH models on a $16 \times 15 \times 15$ lattice at strong couplings outside the LAP (see values in Table 7.1). Data were produced and first used in the context of [128]. . . . .	69
7.2	Chiral condensate in TH models. . . . .	71
7.3	Spectral density according to Eq. (7.8) in 1+2D TH models with $(N_r, 1/2g_{\text{TH}}^2) = (0.80, 0.46)$ and $(1.00, 0.55)$ for various lattice sizes $N_t = 8, 12, 16$ . The filled markers show the data for $N_r = 0.80$ , the empty ones for $N_r = 1.00$ . The inset shows in solid (dotted) lines the $N_t = 16$ , $N_r = 0.80$ (1.00) data for a larger range. . . . .	74
7.4	Temporal correlators according to Eq. (7.11) in 1+2D TH models at the representative sample points $(N_r, 1/2g_{\text{TH}}^2) = (0.80, 0.46)$ and $(1.00, 0.55)$ . The main plot shows the data normalized at $t = 1$ including fits according to Eq. (7.12) over half the temporal extent with values given in Table 7.4. The inset shows $10^4$ times the unnormalized data over the full temporal extent. . . . .	75
7.5	Figures on various aspects of the LFF and its derivative, the LFS. . . . .	77
7.6	Rough sketch of the lattice phase diagram of 1+2D TH models in the $1/2g_{\text{TH}}^2$ - $N_r$ plane on a $N_t = 16$ lattice. The background color indicates the value of the lattice filling factor. The blue solid and orange dashed lines give the estimated positions of the transition into the LAP and the new PT, respectively. The triple point where these two transitions split up is magnified in the inset. The hatched red area indicates our conjecture where $\chi_{\text{SB}}$ occurs. The pink crosses show the positions of maximal (in $1/2g_{\text{TH}}^2$ ) values of the chiral condensate. . . . .	78

# List of Tables

2.1	Summary of some 4FTs and their properties (inspired by a similar table in [70]). . . . .	13
6.1	Proportionality constant between $\mu$ and $k_{\max}$ for all parameter settings at low temperatures. The "linear" and "staircase" fit are explained in the text (see Fig. 6.3 for a visual representation). It is important to stress that the staircase's uncertainty is not comparable to a statistical uncertainty. The quality of fit is much better assessed by the number of outliers in the staircase fit. There were 16 $\mu$ values for each parameter set. . . . .	49
6.2	Fit parameters for linear fits in Fig. 6.9. These fits are to be understood on a qualitative level due to the very sparse data basis. The uncertainties presented in the table are those reported by <code>scipy.optimize.curve_fit</code> [2]. They very likely underestimate the true uncertainties due to a lack of data to estimate them and possible systematic effects. They are only presented for completeness. . . . .	56
6.3	Fit parameters for the three fits shown in Fig. 6.19a and given by Eqs. (3.15), (6.11) and (6.12). One should note that $B$ is a mass for SSB, so we imply a correct normalization $B/\sigma_0$ . . . . .	65
7.1	Values of the coupling constants $1/2g_{\text{Th}}^2$ at which the data in Fig. 7.1 were taken. For comparison, the two lattice phase transitions (LAP transition and parity-breaking transition) found in [128] are given. . . . .	69
7.2	Parameter values obtained from fitting Eq. (7.4) to the data in Fig. 7.2d including the reduced $\chi^2$ . The sign, $S$ , was determined from the trend between the first and last data point. The $N_r = 0.95$ data (marked with an asterisk) are basically flat and are not well described by the ansatz. . . . .	72
7.3	Parameter values obtained from fitting Eq. (7.5) to the data in Fig. 7.2c including the reduced $\chi^2$ . . . . .	73
7.4	Parameter values fitting the double-cosh ansatz Eq. (7.12) to the data depicted in Fig. 7.4. Due to the normalization, we could additionally fix $A_1 = 1$ and only fit $A = A_2$ afterwards, normalizing the result. For $N_r = 0.80$ the correlator $C_0$ was compatible with zero everywhere and could therefore not be fitted reliably. . . . .	76
B.1	Summary of (spatial) lattice setups on which $\chi$ GN model ensembles were generated. . . . .	92
B.2	Overview of external parameters simulated per lattice setup in $\chi$ GN models. The lattices are identified via their ID from Table B.1. All numerical values are given in lattice units. . . . .	92
B.3	Overview over exceptional parameter settings for $\chi$ GN models with a given motivation. If applicable, an ID is given as a basis with potential changes as stated. . . . .	93
B.4	Defaults for various technical parameters in our $\chi$ GN model simulations. These represent the vast majority of ensembles. For individual parameter combinations adjustments were made as can be retraced in the supplementary material [63]. . . . .	93
B.5	Summary of (spatial) lattice setups on which $\mathbb{Z}_2$ -GN model ensembles were generated. . . . .	94
B.6	Overview of external parameters simulated per lattice setup $\mathbb{Z}_2$ -GN models. The lattices are identified via their ID from Table B.5. All numerical values are given in lattice units. The marked (*) value applies only to $N_s \leq 63$ ; $N_s = 127$ was only simulated up to $\mu = 0.390$ . . . . .	94

B.7	Overview over exceptional parameter settings for $\mathbb{Z}_2$ -GN models with a given motivation. If applicable, an ID is given as a basis with potential changes as stated. . . . .	95
B.8	Defaults for various technical parameters for our $\mathbb{Z}_2$ -GN model simulations. These represent the vast majority of ensembles. For individual parameter combinations adjustments were made as can be retraced in the supplementary material [63]. . . . .	95
B.9	Summary of ensembles generated for scanning the PD of TH models. The asterisk means that there is a sliding window following the maximum of the condensate as described in the text. . . . .	97
B.10	Defaults for various technical parameters for our TH model simulations. These represent the vast majority of ensembles. For individual parameter combinations adjustments were made as can be retraced in the supplementary material [63]. . . . .	97

# Bibliography

1. Janke, W. in *Computational Many-Particle Physics* (eds Fehske, H., Schneider, R. & Weiße, A.) 79–140 (Springer Berlin Heidelberg, Berlin, Heidelberg, 2008). doi:10.1007/978-3-540-74686-7\_4. (Cit. on pp. vi, 30, 43, 77).
2. SciPy 1.0 Contributors *et al.* SciPy 1.0: Fundamental Algorithms for Scientific Computing in Python. *Nat Methods* **17**, 261–272. doi:10.1038/s41592-019-0686-2. (2020) (cit. on pp. vi, 56, 63, 99).
3. Castro Neto, A. H. *et al.* The Electronic Properties of Graphene. *Rev. Mod. Phys.* **81**, 109–162. doi:10.1103/RevModPhys.81.109. (2009) (cit. on pp. 1, 2).
4. Wehling, T. O., Black-Schaffer, A. M. & Balatsky, A. V. Dirac Materials. *Adv. Phys.* **63**, 1–76. doi:10.1080/00018732.2014.927109. (2014) (cit. on pp. 1, 2).
5. Volkov, M. & Radzhabov, A. The Nambu – Jona’Lasinio Model and Its Development. *Phys.-Usp.* **176**, 569. doi:10/dqbfsp (2006) (cit. on p. 1).
6. Buballa, M. & Carignano, S. Inhomogeneous Chiral Symmetry Breaking in Dense Neutron-Star Matter. *Eur. Phys. J. A* **52**, 57. doi:10.1140/epja/i2016-16057-6. (2016) (cit. on pp. 1–3, 17).
7. Fermi, E. Versuch einer Theorie der Strahlen. I. *Z. Physik* **88**, 161–177. doi:10.1007/BF01351864. (1934) (cit. on p. 1).
8. Thirring, W. E. A Soluble Relativistic Field Theory. *Ann. Phys.* **3**, 91–112. doi:10.1016/0003-4916(58)90015-0 (1958) (cit. on pp. 1, 15).
9. Nambu, Y. & Jona-Lasinio, G. Dynamical Model of Elementary Particles Based on an Analogy with Superconductivity. II. *Phys. Rev.* **124**, 246–254. doi:10.1103/PhysRev.124.246. (1961) (cit. on pp. 1, 15).
10. Nambu, Y. & Jona-Lasinio, G. Dynamical Model of Elementary Particles Based on an Analogy with Superconductivity. I. *Phys. Rev.* **122**, 345–358. doi:10.1103/PhysRev.122.345. (1961) (cit. on pp. 1, 14).
11. Bardeen, J., Cooper, L. N. & Schrieffer, J. R. Microscopic Theory of Superconductivity. *Phys. Rev.* **106**, 162–164. doi:10.1103/PhysRev.106.162. (1957) (cit. on p. 1).
12. Hubbard, J. Electron Correlations in Narrow Energy Bands. *Proc. R. Soc. Lond. A*, 238–257. doi:10.1098/rspa.1963.0204. (1963) (cit. on p. 2).
13. Lieb, E. H. & Wu, F. Y. Absence of Mott Transition in an Exact Solution of the Short-Range, One-Band Model in One Dimension. *Phys. Rev. Lett.* **20**, 1445–1448. doi:10.1103/PhysRevLett.20.1445. (1968) (cit. on p. 2).
14. Fulde, P. & Ferrell, R. A. Superconductivity in a Strong Spin-Exchange Field. *Phys. Rev.* **135**, A550–A563. doi:10.1103/physrev.135.a550. (3A 1964) (cit. on p. 2).
15. Larkin, A. I. & Ovchinnikov, Y. N. Nonuniform State of Superconductors. *Sov. Phys. JETP* **20**, 762–762 (1965) (cit. on p. 2).
16. Schnetz, O., Thies, M. & Urlichs, K. Phase Diagram of the Gross–Neveu Model: Exact Results and Condensed Matter Precursors. *Ann. Phys.* **314**, 425–447. doi:10.1016/j.aop.2004.06.009. (2004) (cit. on pp. 2, 3, 21–24).
17. Schön, V. & Thies, M. in *At The Frontier of Particle Physics* (ed Shifman, M.) 1945–2032 (World Scientific, 2001). doi:10.1142/9789812810458\_0041. (Cit. on pp. 2, 3, 21).
18. Thies, M. & Urlichs, K. Revised Phase Diagram of the Gross-Neveu Model. *Phys. Rev. D* **67**. doi:10.1103/physrevd.67.125015. (2003) (cit. on pp. 2, 21).
19. Gross, D. J. & Neveu, A. Dynamical Symmetry Breaking in Asymptotically Free Field Theories. *Phys. Rev. D* **10**, 3235–3253. doi:10.1103/PhysRevD.10.3235. (1974) (cit. on pp. 2, 12, 14).
20. Buballa, M. & Carignano, S. Inhomogeneous Chiral Condensates. *Prog.Part.Nucl.Phys.* **81**, 39–96. doi:10.1016/j.ppnp.2014.11.001. (2015) (cit. on pp. 2, 15, 24).
21. Lakaschus, P., Buballa, M. & Rischke, D. H. Competition of Inhomogeneous Chiral Phases and Two-Flavor Color Superconductivity in the NJL Model. *Phys. Rev. D* **103**, 034030. doi:10.1103/PhysRevD.103.034030. (2021) (cit. on p. 2).

22. Hands, S., Kocic, A. & Kogut, J. B. Four - Fermi Theories in Fewer Than Four Dimensions. *Ann. Phys.* **224**, 29–89. doi:10.1006/aphy.1993.1039. (1993) (cit. on pp. 2, 32).
23. Hands, S., Kim, S. & Kogut, J. B. The U(1) Gross-Neveu Model at Non-Zero Chemical Potential. *Nucl. Phys. B* **442**, 364–388. doi:10.1016/0550-3213(95)00136-0. (1995) (cit. on p. 2).
24. Hands, S., Armour, W. & Strouthos, C. *Graphene as a Lattice Field Theory* in *Proceedings of 9th International Workshop on Critical Point and Onset of Deconfinement — PoS(CPOD2014)* 9th International Workshop on Critical Point and Onset of Deconfinement (Sissa Medialab, ZiF (Center of Interdisciplinary Research), University of Bielefeld, Germany, 2015), 016. doi:10.22323/1.217.0016. (Cit. on p. 2).
25. Herbut, I. F., Juričić, V. & Roy, B. Theory of Interacting Electrons on the Honeycomb Lattice. *Phys. Rev. B* **79**, 085116. doi:10.1103/PhysRevB.79.085116. (2009) (cit. on p. 2).
26. Balatsky, A. V., Vekhter, I. & Zhu, J.-X. Impurity-Induced States in Conventional and Unconventional Superconductors. *Rev. Mod. Phys.* **78**, 373–433. doi:10.1103/RevModPhys.78.373. (2006) (cit. on p. 2).
27. Hasan, M. Z. & Kane, C. L. Colloquium: Topological Insulators. *Rev. Mod. Phys.* **82**, 3045–3067. doi:10.1103/RevModPhys.82.3045. (2010) (cit. on p. 2).
28. Qi, X.-L. & Zhang, S.-C. Topological Insulators and Superconductors. *Rev. Mod. Phys.* **83**, 1057–1110. doi:10.1103/RevModPhys.83.1057. (2011) (cit. on p. 2).
29. Worthy, J. & Hands, S. *Properties of Overlap and Domain Wall Fermions in the 2+1D Thirring Model* in *Proceedings of The 38th International Symposium on Lattice Field Theory — PoS(LATTICE2021)* The 38th International Symposium on Lattice Field Theory (Sissa Medialab, Zoom/Gather@Massachusetts Institute of Technology, 2022), 317. doi:10.22323/1.396.0317. (Cit. on pp. 2, 39, 68, 72, 80).
30. Dabelow, L., Gies, H. & Knorr, B. Momentum Dependence of Quantum Critical Dirac Systems. *Phys. Rev. D* **99**, 125019. doi:10.1103/PhysRevD.99.125019. (2019) (cit. on pp. 2, 68, 70, 80).
31. Kanazawa, T., Kieburg, M. & Verbaarschot, J. J. Cascade of Phase Transitions in a Planar Dirac Material. *J. High Energ. Phys.* **2021**, 15. doi:10.1007/JHEP06(2021)015. (2021) (cit. on p. 2).
32. Janssen, L. *et al.* Confinement Transition in the QED3-Gross-Neveu-XY Universality Class. *Phys. Rev. B* **101**, 235118. doi:10.1103/PhysRevB.101.235118. (2020) (cit. on p. 2).
33. Seifert, U. F. P. *et al.* Fractionalized Fermionic Quantum Criticality in Spin-Orbital Mott Insulators. *Phys. Rev. Lett.* **125**, 257202. doi:10.1103/PhysRevLett.125.257202. (2020) (cit. on p. 2).
34. Catterall, S. Fermion Mass without Symmetry Breaking. *J. High Energ. Phys.* **2016**. doi:10.1007/JHEP01(2016)121. (2016) (cit. on p. 2).
35. Kneur, J.-L., Pinto, M. B. & Ramos, R. O. Phase Diagram of the Magnetized Planar Gross-Neveu Model beyond the Large- N Approximation. *Phys. Rev. D* **88**, 045005. doi:10.1103/PhysRevD.88.045005. (2013) (cit. on p. 2).
36. Butt, N. & Catterall, S. *Four Fermion Condensates in SU(2) Yang-Mills-Higgs Theory on a Lattice* in *Proceedings of The 36th Annual International Symposium on Lattice Field Theory — PoS(LATTICE2018)* The 36th Annual International Symposium on Lattice Field Theory (Sissa Medialab, Michigan State University, East Lansing, Michigan, USA., 2019), 294. doi:10.22323/1.334.0294. (Cit. on p. 2).
37. Lenz, J. J., Mandl, M. & Wipf, A. *The Magnetized (2+1)-Dimensional Gross-Neveu Model at Finite Density* preprint (cit. on pp. 2, 3, 39, 84, 117).
38. Lenz, J. J., Mandl, M. & Wipf, A. Magnetic Catalysis in the (2+1)-Dimensional Gross-Neveu Model. *Phys. Rev. D* **107**, 094505. doi:10.1103/PhysRevD.107.094505. (2023) (cit. on pp. 2, 3, 39, 84, 117).
39. Benedetti, D. *et al.* Tensorial Gross-Neveu Models. *J. High Energ. Phys.* **2018**, 3. doi:10.1007/JHEP01(2018)003. (2018) (cit. on p. 2).
40. Benedetti, D. & Delporte, N. Phase Diagram and Fixed Points of Tensorial Gross-Neveu Models in Three Dimensions. *J. High Energ. Phys.* **2019**, 218. doi:10.1007/JHEP01(2019)218. (2019) (cit. on p. 2).
41. Witten, E. Chiral Symmetry, the 1/N Expansion and the SU(N) Thirring Model. *Nucl. Phys. B* **145**, 110–118. doi:10.1016/0550-3213(78)90416-9. (1978) (cit. on pp. 2, 27, 64).
42. Lenz, J. J., Mandl, M. & Wipf, A. Inhomogeneities in the Two-Flavor Chiral Gross-Neveu Model. *Phys. Rev. D* **105**, 034512. doi:10.1103/PhysRevD.105.034512. (2022) (cit. on pp. 2, 3, 25, 34, 38, 45, 46, 91, 117).
43. Lenz, J. & Mandl, M. *Remnants of Large-Nf Inhomogeneities in the 2-Flavor Chiral Gross-Neveu Model* in *Proceedings of The 38th International Symposium on Lattice Field Theory — PoS(LATTICE2021)* The 38th International Symposium on Lattice Field Theory (Sissa Medialab, Zoom/Gather@Massachusetts Institute of Technology, 2022), 415. doi:10.22323/1.396.0415. (Cit. on pp. 2, 3, 38, 45, 117).

44. Andersen, J. O. *Phase Fluctuations in Low-Dimensional Gross-Neveu Models* 2005. (Cit. on pp. 2, 26).
45. Gies, H. & Janssen, L. UV Fixed-Point Structure of the Three-Dimensional Thirring Model. *Phys. Rev. D* **82**, 085018. doi:10.1103/PhysRevD.82.085018. (2010) (cit. on pp. 2, 12, 70, 80).
46. Janssen, L. & Gies, H. Critical Behavior of the  $(2 + 1)$ -Dimensional Thirring Model. *Phys. Rev. D* **86**, 105007. doi:10.1103/PhysRevD.86.105007. (2012) (cit. on pp. 2, 70, 73, 80).
47. Scherer, D. D. & Gies, H. Renormalization Group Study of Magnetic Catalysis in the 3d Gross-Neveu Model. *Phys. Rev. B* **85**. (2012) (cit. on p. 2).
48. Tripolt, R.-A. *et al.* Fermionic Spectral Functions with the Functional Renormalization Group. *Phys. Rev. D* **98**. doi:10.1103/PhysRevD.98.094002. (2018) (cit. on p. 2).
49. Janssen, L. & Herbut, I. F. Antiferromagnetic Critical Point on Graphene's Honeycomb Lattice: A Functional Renormalization Group Approach. *Phys. Rev. B* **89**, 205403. doi:10.1103/PhysRevB.89.205403. (2014) (cit. on p. 2).
50. Scherer, D. D., Braun, J. & Gies, H. Many-Flavor Phase Diagram of the  $(2+1)$ d Gross-Neveu Model at Finite Temperature. *J. Phys. A* **46**, 285002. doi:10.1088/1751-8113/46/28/285002. (2013) (cit. on p. 2).
51. Bañuls, M. C. *et al.* Phase Structure of the  $(1 + 1)$ -Dimensional Massive Thirring Model from Matrix Product States. *Phys. Rev. D* **100**, 094504. doi:10.1103/PhysRevD.100.094504. (2019) (cit. on p. 2).
52. Bruognolo, B. *et al.* A Beginner's Guide to Non-Abelian iPEPS for Correlated Fermions. *SciPost Phys. Lect. Notes*, 25. doi:10.21468/SciPostPhysLectNotes.25. (2021) (cit. on p. 2).
53. Takeda, S. & Yoshimura, Y. Grassmann Tensor Renormalization Group for the One-Flavor Lattice Gross-Neveu Model with Finite Chemical Potential. *PTEP* **2015**. doi:10.1093/ptep/ptv022. (2015) (cit. on p. 2).
54. Troyer, M. & Wiese, U.-J. Computational Complexity and Fundamental Limitations to Fermionic Quantum Monte Carlo Simulations. *Phys. Rev. Lett.* **94**, 170201. doi:10.1103/PhysRevLett.94.170201. (2005) (cit. on pp. 2, 30, 40).
55. De Forcrand, P. *Simulating QCD at Finite Density in Proceedings of The XXVII International Symposium on Lattice Field Theory — PoS(LAT2009)* The XXVII International Symposium on Lattice Field Theory (Sissa Medialab, Peking University, Beijing, China, 2010), 010. doi:10.22323/1.091.0010. (Cit. on pp. 2, 40).
56. Alexandru, A. *et al.* Complex Paths around the Sign Problem. *Rev. Mod. Phys.* **94**, 015006. doi:10.1103/RevModPhys.94.015006. (2022) (cit. on pp. 2, 40).
57. Abbott, R. *et al.* *Sampling QCD Field Configurations with Gauge-Equivariant Flow Models in Proceedings of The 39th International Symposium on Lattice Field Theory — PoS(LATTICE2022)* The 39th International Symposium on Lattice Field Theory (Sissa Medialab, Bonn, Germany, 2023), 036. doi:10.22323/1.430.0036. (Cit. on pp. 2, 40).
58. Zinn-Justin, J. *Quantum Field Theory and Critical Phenomena* doi:10.1093/acprof:oso/9780198509233.001.0001. (Oxford University Press, 2002) (cit. on p. 3).
59. Nambu, Y. Quasi-Particles and Gauge Invariance in the Theory of Superconductivity. *Phys. Rev.* **117**, 648–663. doi:10.1103/PhysRev.117.648. (1960) (cit. on p. 3).
60. Goldstone, J. Field Theories with Superconductor Solutions. *Nuovo Cim* **19**, 154–164. doi:10.1007/BF02812722. (1961) (cit. on p. 3).
61. Goldstone, J., Salam, A. & Weinberg, S. Broken Symmetries. *Phys. Rev.* **127**, 965–970. doi:10.1103/PhysRev.127.965. (1962) (cit. on p. 3).
62. Casalbuoni, R. & Nardulli, G. Inhomogeneous Superconductivity in Condensed Matter and QCD. *Rev. Mod. Phys.* **76**, 263–320. doi:10.1103/RevModPhys.76.263. (2004) (cit. on pp. 3, 14).
63. Lenz, J. J. *Analysis and Visualization Code for Thesis "Four-Fermi Theories On The Lattice And In The Continuum"* 2023. URL: <https://doi.org/10.5281/zenodo.8262870> (cit. on pp. 3, 31, 91, 93–95, 97, 99).
64. Lenz, J. J., Welleghausen, B. H. & Wipf, A. Absence of Chiral Symmetry Breaking in Thirring Models in  $1 + 2$  Dimensions. *Phys. Rev. D* **100**, 054501. doi:10.1103/PhysRevD.100.054501. (2019) (cit. on pp. 3, 12, 38, 74–76, 78, 85, 89, 117).
65. Lenz, J. *et al.* Inhomogeneous Phases in the Gross-Neveu Model in  $1 + 1$  Dimensions at Finite Number of Flavors. *Phys. Rev. D* **101**, 094512. doi:10.1103/PhysRevD.101.094512. (2020) (cit. on pp. 3, 34, 36–38, 45, 46, 58, 65, 117).
66. Lenz, J. J. *et al.* Baryons in the Gross-Neveu Model in  $1 + 1$  Dimensions at Finite Number of Flavors. *Phys. Rev. D* **102**, 114501. doi:10.1103/PhysRevD.102.114501. (2020) (cit. on pp. 3, 25, 38, 40, 45, 46, 117).
67. Pannullo, L. *et al.* Inhomogeneous Phases in the  $1+1$  Dimensional Gross-Neveu Model at Finite Number of Fermion Flavors. *Acta Phys. Pol. B Proc. Suppl.* **13**, 127. doi:10.5506/APhysPolBSupp.13.127. (2020) (cit. on pp. 3, 37, 38, 46, 117).
68. Pannullo, L. *et al.* *Lattice Investigation of the Phase Diagram of the  $1+1$  Dimensional Gross-Neveu Model at Finite Number of Fermion Flavors in Proceedings of 37th International Symposium on Lattice Field Theory — PoS(LATTICE2019)* 37th International Symposium on Lattice Field Theory (Sissa Medialab, Wuhan, China, 2020), 063. doi:10.22323/1.363.0063. (Cit. on pp. 3, 37, 38, 46, 117).

69. Wipf, A. W. & Lenz, J. J. Symmetries of Thirring Models on 3D Lattices. *Symmetry* **14**, 333. doi:10.3390/sym14020333. (2022) (cit. on pp. 3, 7, 68, 117).
70. Wipf, A. *Statistical Approach to Quantum Field Theory: An Introduction* doi:10.1007/978-3-030-83263-6. (Springer International Publishing, Cham, 2021) (cit. on pp. 5–7, 13, 15–17, 19, 35, 37).
71. Wetterich, C. Spinors in Euclidean Field Theory, Complex Structures and Discrete Symmetries. *Nucl. Phys. B* **852**, 174–234. doi:10.1016/j.nucphysb.2011.06.013. (2011) (cit. on pp. 6–9).
72. Mehta, M. R. Euclidean Continuation of the Dirac Fermion. *Phys. Rev. Lett.* **65**, 1983–1986. doi:10.1103/PhysRevLett.65.1983. (1990) (cit. on p. 7).
73. Banerjee, H., Mitra, P. & Chatterjee, D. Dirac Fermion in Euclidean Metric and the U(1) and Strong CP Problems. *Z. Phys. C - Particles and Fields* **62**, 511–520. doi:10.1007/BF01555912. (1994) (cit. on p. 7).
74. Jain, J. K. *It's Anyon's Game: The Race to Quantum Computation* 2020. (Cit. on p. 7).
75. Streater, R. F. & Wightman, A. S. *PCT, Spin and Statistics, and All That* doi:10.1515/9781400884230. (Princeton University Press, 2001) (cit. on pp. 8, 48).
76. Pauli, W. On the Conservation of the Lepton Charge. *Nuovo Cim* **6**, 204–215. doi:10.1007/BF02827771. (1957) (cit. on p. 9).
77. Gürsey, F. Relation of Charge Independence and Baryon Conservation to Pauli's Transformation. *Nuovo Cim* **7**, 411–415. doi:10.1007/BF02747705. (1958) (cit. on p. 9).
78. Vaks, V. G. & Larkin, A. I. On the Application of the Methods of Superconductivity Theory to the Problem of the Masses of Elementary Particles. *J. Exp. Theo. Phys.*, 282–285 (1961) (cit. on p. 14).
79. Roose, G. *et al.* The Chiral Gross-Neveu Model on the Lattice via a Landau-forbidden Phase Transition. *J. High Energ. Phys.* **2022**, 19. doi:10.1007/JHEP06(2022)019. (2022) (cit. on p. 14).
80. Pelaez, J. R. From Controversy to Precision on the Sigma Meson: A Review on the Status of the Non-Ordinary F0(500) Resonance. *Physics Reports* **658**, 1–111. doi:10.1016/j.physrep.2016.09.001. (2016) (cit. on p. 15).
81. Srednicki, M. A. *Quantum Field Theory* doi:10.1017/CB09780511813917 (Cambridge University Press, Cambridge ; New York, 2007) (cit. on p. 15).
82. Osipov, A. A., Hiller, B. & Blin, A. H. Effective Multiquark Interactions with Explicit Breaking of Chiral Symmetry. *Phys. Rev. D* **88**, 054032. doi:10.1103/PhysRevD.88.054032. (2013) (cit. on p. 15).
83. Itoh, T. *et al.* Thirring Model as a Gauge Theory. *Prog. Theo. Phys.* **93**, 417–439. doi:10.1143/PTP.93.417. (1995) (cit. on pp. 15, 70, 80).
84. Hands, S. *Planar Thirring Model in the U(2N)-Symmetric Limit* preprint (cit. on pp. 15, 39, 68, 72, 80, 85).
85. Vacca, G. P. & Zambelli, L. Multimeson Yukawa Interactions at Criticality. *Phys. Rev. D* **91**. doi:10.1103/PhysRevD.91.125003. (2015) (cit. on p. 16).
86. Gusynin, V. P., Miransky, V. A. & Shovkovy, I. A. Dynamical Flavor Symmetry Breaking by a Magnetic Field in 2+1 Dimensions. *Phys. Rev. D* **52**, 4718–4735. doi:10.1103/PhysRevD.52.4718. (1995) (cit. on p. 17).
87. Mandl, M., Lenz, J. & Wipf, A. *Magnetic Catalysis in the 1-Flavor Gross-Neveu Model in 2+1 Dimensions in Proceedings of The 39th International Symposium on Lattice Field Theory — PoS(LATTICE2022)* The 39th International Symposium on Lattice Field Theory (Sissa Medialab, Bonn, Germany, 2023), 152. doi:10.22323/1.430.0152. (Cit. on pp. 17, 39, 117).
88. Thies, M. From Relativistic Quantum Fields to Condensed Matter and Back Again: Updating the Gross-Neveu Phase Diagram. *J. Phys. A* **39**, 12707–12734. doi:10.1088/0305-4470/39/41/s04. (2006) (cit. on pp. 17, 22).
89. Hands, S. Towards Critical Physics in 2+1d with U(2N)-Invariant Fermions. *J. High Energ. Phys.* **2016**, 15. doi:10.1007/JHEP11(2016)015. (2016) (cit. on pp. 17, 32, 39, 68, 72, 80).
90. Gattringer, C. & Lang, C. B. *Quantum Chromodynamics on the Lattice: An Introductory Presentation Lecture Notes in Physics* **788**. 343 pp. (Springer, Heidelberg ; New York, 2010) (cit. on pp. 17, 30, 31, 35, 37, 39, 40).
91. Tuchin, K. Particle Production in Strong Electromagnetic Fields in Relativistic Heavy-Ion Collisions. *Adv.High Energy Phys.* **2013**, 1–34. doi:10.1155/2013/490495. (2013) (cit. on p. 17).
92. Subramanian, K. Magnetic Fields in the Early Universe. *Astron. Nachr.* **331**, 110–120. doi:10.1002/asna.200911312. (2010) (cit. on p. 17).
93. Buballa, M. NJL-model Analysis of Dense Quark Matter. *Phys. Rep.* **407**, 205–376. doi:10.1016/j.physrep.2004.11.004. (2005) (cit. on p. 20).
94. Wolff, U. The Phase Diagram of the Infinite-N Gross-Neveu Model at Finite Temperature and Chemical Potential. *Phys. Lett. B* **157**, 303–308. doi:10.1016/0370-2693(85)90671-9. (1985) (cit. on p. 20).

95. Sarma, G. On the Influence of a Uniform Exchange Field Acting on the Spins of the Conduction Electrons in a Superconductor. *J. Phys. Chem. Solids* **24**, 1029–1032. doi:10.1016/0022-3697(63)90007-6. (1963) (cit. on p. 20).
96. Lenz, J. J. *Spontaneous Symmetry Breaking In Four Fermion Theories* MSc (University of Jena, Jena, 2018). 77 pp. (Cit. on pp. 21, 32, 38, 68, 117).
97. Başar, G. & Dunne, G. V. Self-Consistent Crystalline Condensate in Chiral Gross-Neveu and Bogoliubov–de Gennes Systems. *Phys. Rev. Lett.* **100**, 200404. doi:10.1103/PhysRevLett.100.200404. (2008) (cit. on p. 21).
98. Karsch, F., Kogut, J. & Wyld, H. The Gross-Neveu Model at Finite Temperature and Density. *Nuclear Physics B* **280**, 289–303. doi:10.1016/0550-3213(87)90149-0. (1987) (cit. on p. 22).
99. Dashen, R. F., Hasslacher, B. & Neveu, A. Semiclassical Bound States in an Asymptotically Free Theory. *Phys. Rev. D* **12**, 2443–2458. doi:10.1103/physrevd.12.2443. (1975) (cit. on p. 23).
100. Narayanan, R. Phase Diagram of the Large N Gross-Neveu Model in a Finite Periodic Box. *Phys. Rev. D* **101**, 096001. doi:10.1103/PhysRevD.101.096001. (2020) (cit. on p. 23).
101. Winstel, M., Pannullo, L. & Wagner, M. *Phase Diagram of the 2+1-Dimensional Gross-Neveu Model with Chiral Imbalance* in *Proceedings of The 38th International Symposium on Lattice Field Theory — PoS(LATTICE2021)* The 38th International Symposium on Lattice Field Theory (Sissa Medialab, Zoom/Gather@Massachusetts Institute of Technology, 2022), 381. doi:10.22323/1.396.0381. (Cit. on pp. 23, 55).
102. Winstel, M. & Pannullo, L. *Stability of Homogeneous Chiral Phases against Inhomogeneous Perturbations in 2+1 Dimensions* in *Proceedings of The 39th International Symposium on Lattice Field Theory — PoS(LATTICE2022)* The 39th International Symposium on Lattice Field Theory (Sissa Medialab, Bonn, Germany, 2023), 195. doi:10.22323/1.430.0195. (Cit. on p. 23).
103. Buballa, M. *et al.* Regulator Dependence of Inhomogeneous Phases in the  $(2 + 1)$ -Dimensional Gross-Neveu Model. *Phys. Rev. D* **103**, 034503. doi:10.1103/PhysRevD.103.034503. (2021) (cit. on pp. 23, 24, 55).
104. Carignano, S., Buballa, M. & Schaefer, B.-J. Inhomogeneous Phases in the Quark-Meson Model with Vacuum Fluctuations. *Phys. Rev. D* **90**, 014033. doi:10.1103/PhysRevD.90.014033. (2014) (cit. on pp. 24, 25).
105. Matsuda, Y. & Shimahara, H. Fulde-Ferrell-Larkin-Ovchinnikov State in Heavy Fermion Superconductors. *J. Phys. Soc. Jpn.* **76**, 051005. doi:10.1143/JPSJ.76.051005. (2007) (cit. on p. 24).
106. Koutroulakis, G. *et al.* Microscopic Study of the Fulde-Ferrell-Larkin-Ovchinnikov State in an All-Organic Superconductor. *Phys. Rev. Lett.* **116**, 067003. doi:10.1103/PhysRevLett.116.067003. (2016) (cit. on p. 24).
107. Carignano, S. & Buballa, M. Inhomogeneous Chiral Condensates in Three-Flavor Quark Matter. *Phys. Rev. D* **101**, 014026. doi:10.1103/PhysRevD.101.014026. (2020) (cit. on p. 24).
108. Pannullo, L., Wagner, M. & Winstel, M. *Inhomogeneous Phases in the 3+1-Dimensional Nambu-Jona-Lasinio Model and Their Dependence on the Regularization Scheme* in *Proceedings of The 39th International Symposium on Lattice Field Theory — PoS(LATTICE2022)* The 39th International Symposium on Lattice Field Theory (Sissa Medialab, Bonn, Germany, 2022), 156. doi:10.22323/1.430.0156. (Cit. on p. 24).
109. Carignano, S., Buballa, M. & Elkamhawy, W. Consistent Parameter Fixing in the Quark-Meson Model with Vacuum Fluctuations. *Phys. Rev. D* **94**, 034023. doi:10.1103/PhysRevD.94.034023. (2016) (cit. on p. 24).
110. Carignano, S. & Buballa, M. Inhomogeneous Islands and Continents in the Nambu–Jona-Lasinio Model. *Acta Phys. Pol. B Proc. Suppl.* **5**, 641. doi:10.5506/APhysPoLBSupp.5.641. (2012) (cit. on p. 25).
111. Mermin, N. D. & Wagner, H. Absence of Ferromagnetism or Antiferromagnetism in One- or Two-Dimensional Isotropic Heisenberg Models. *Phys. Rev. Lett.* **17**, 1133–1136. doi:10.1103/PhysRevLett.17.1133. (1966) (cit. on p. 26).
112. Hohenberg, P. C. Existence of Long-Range Order in One and Two Dimensions. *Phys. Rev.* **158**, 383–386. doi:10.1103/PhysRev.158.383. (1967) (cit. on p. 26).
113. Coleman, S. There Are No Goldstone Bosons in Two Dimensions. *Commun. Math. Phys.* **31**, 259–264. doi:10.1007/BF01646487. (1973) (cit. on p. 26).
114. Nielsen, H. & Chadha, S. On How to Count Goldstone Bosons. *Nucl. Phys. B* **105**, 445–453. doi:10.1016/0550-3213(76)90025-0. (1976) (cit. on p. 27).
115. Watanabe, H. & Brauner, T. On the Number of Nambu-Goldstone Bosons and Its Relation to Charge Densities. *Phys. Rev. D* **84**. doi:10.1103/PhysRevD.84.125013. (2011) (cit. on p. 27).
116. Watanabe, H. & Brauner, T. Spontaneous Breaking of Continuous Translational Invariance. *Phys. Rev. D* **85**. doi:10.1103/PhysRevD.85.085010. (2012) (cit. on p. 27).
117. Berezinskiĭ, V. L. Destruction of Long-range Order in One-dimensional and Two-dimensional Systems Having a Continuous Symmetry Group I. Classical Systems. *Soviet Journal of Experimental and Theoretical Physics* **32**, 493. (1971) (cit. on p. 27).

118. Berezinskiĭ, V. L. Destruction of Long-range Order in One-dimensional and Two-dimensional Systems Possessing a Continuous Symmetry Group. II. Quantum Systems. *Soviet Journal of Experimental and Theoretical Physics* **34**, 610. (1972) (cit. on p. 27).
119. Kosterlitz, J. M. & Thouless, D. J. Ordering, Metastability and Phase Transitions in Two-Dimensional Systems. *J. Phys. C* **6**, 1181–1203. doi:10.1088/0022-3719/6/7/010. (1973) (cit. on p. 27).
120. Landau, D. P. & Lifshitz, E. M. *Statistical Physics* (1958) (cit. on p. 27).
121. Peierls, R. in Dalitz, R. H. & Peierls, S. R. *World Scientific Series in 20th Century Physics* 137–138 (Imperial College Press and World Scientific, 1997). doi:10.1142/9789812795779\_0014. (Cit. on pp. 27, 60).
122. Mermin, N. D. Crystalline Order in Two Dimensions. *Phys. Rev.* **176**, 250–254. doi:10.1103/PhysRev.176.250. (1968) (cit. on p. 28).
123. Gasser, U. *et al.* Melting of Crystals in Two Dimensions. *ChemPhysChem* **11**, 963–970. doi:10.1002/cphc.200900755. (2010) (cit. on p. 28).
124. Thompson-Flagg, R. C., Moura, M. J. B. & Marder, M. Rippling of Graphene. *Europhys. Lett.* **85**, 46002. doi:10.1209/0295-5075/85/46002. (2009) (cit. on p. 28).
125. Piskarski, R. D., Tsvetlik, A. M. & Valgushev, S. How Transverse Thermal Fluctuations Disorder a Condensate of Chiral Spirals into a Quantum Spin Liquid. *Phys. Rev. D* **102**, 016015. doi:10/gg9n3t. (2020) (cit. on p. 28).
126. Clark, M. *AlgRemez* 2005. URL: <https://github.com/maddyscientist/AlgRemez> (visited on 2023-09-17) (cit. on pp. 31, 99).
127. Wellegehausen, B. H. *Phase Diagrams of Exceptional and Supersymmetric Lattice Gauge Theories* PhD thesis (University of Jena, Jena, 2012). (Cit. on pp. 31, 99).
128. Wellegehausen, B. H., Schmidt, D. & Wipf, A. Critical Flavor Number of the Thirring Model in Three Dimensions. *Phys. Rev. D* **96**, 094504. doi:10.1103/PhysRevD.96.094504. (2017) (cit. on pp. 32, 68, 69, 76, 96).
129. Chandrasekharan, S. The Fermion Bag Approach to Lattice Field Theories. *Phys. Rev. D* **82**. doi:10.1103/PhysRevD.82.025007. (2010) (cit. on pp. 32, 68).
130. Janssen, L. & Seifert, U. F. P. Phase Diagrams of  $SO(N)$  Majorana-Hubbard Models: Dimerization, Internal Symmetry Breaking, and Fluctuation-Induced First-Order Transitions. *Phys. Rev. B* **105**, 045120. doi:10.1103/PhysRevB.105.045120. (2022) (cit. on pp. 32, 85).
131. Liu, Z. H. *et al.* Metallic and Deconfined Quantum Criticality in Dirac Systems. *Phys. Rev. Lett.* **128**, 087201. doi:10.1103/PhysRevLett.128.087201. (2022) (cit. on pp. 32, 85).
132. Nielsen, H. & Ninomiya, M. Absence of Neutrinos on a Lattice: (I). Proof by Homotopy Theory. *Nucl. Phys. B* **185**, 20–40. doi:10.1016/0550-3213(81)90361-8. (1981) (cit. on pp. 35, 37).
133. Nielsen, H. & Ninomiya, M. Absence of Neutrinos on a Lattice: (II). Intuitive Topological Proof. *Nucl. Phys. B* **193**, 173–194. doi:10.1016/0550-3213(81)90524-1. (1981) (cit. on pp. 35, 37).
134. Cohen, Y., Elitzur, S. & Rabinovici, E. A Monte Carlo Study of the Gross-Neveu Model. *Nucl. Phys. B* **220**, 102–118. doi:10.1016/0550-3213(83)90136-0. (1983) (cit. on p. 36).
135. Becher, P. & Joos, H. The Dirac-Kähler Equation and Fermions on the Lattice. *Z. Phys. C - Particles and Fields* **15**, 343–365. doi:10.1007/BF01614426. (1982) (cit. on p. 37).
136. Hands, S. The Planar Thirring Model with Kähler-Dirac Fermions. *Symmetry* **13**, 1523. doi:10.3390/sym13081523. (2021) (cit. on pp. 37, 39, 68, 72, 80).
137. Aoki, S. & Higashijima, K. The Recovery of the Chiral Symmetry in Lattice Gross-Neveu Model. *Prog. Theo. Phys.* **76**, 521–537. doi:10.1143/PTP.76.521. (1986) (cit. on p. 37).
138. Karsten, L. H. & Smit, J. Lattice Fermions: Species Doubling, Chiral Invariance and the Triangle Anomaly. *Nucl. Phys. B* **183**, 103–140. doi:10.1016/0550-3213(81)90549-6. (1981) (cit. on pp. 37, 38).
139. Drell, S. D., Weinstein, M. & Yankielowicz, S. Strong-Coupling Field Theories. II. Fermions and Gauge Fields on a Lattice. *Phys. Rev. D* **14**, 1627–1647. doi:10.1103/physrevd.14.1627. (1976) (cit. on p. 38).
140. Drell, S. D., Weinstein, M. & Yankielowicz, S. Strong-Coupling Field Theory. I. Variational Approach to  $\phi^4$  Theory. *Phys. Rev. D* **14**, 487–516. doi:10.1103/PhysRevD.14.487. (1976) (cit. on p. 38).
141. Ullmann, D. *Anwendung der SLAC-Ableitung auf quantenmechanische Systeme* B.Sc. (University of Jena, Jena, 2012). 37 pp. (Cit. on p. 38).
142. Karsten, L. H. & Smit, J. The Vacuum Polarization with SLAC Lattice Fermions. *Phys. Lett. B* **85**, 100–102. doi:10.1016/0370-2693(79)90786-x. (1979) (cit. on pp. 38, 40).

143. Karsten, L. H. & Smit, J. Axial Symmetry in Lattice Theories. *Nucl. Phys. B* **144**, 536–546. doi:10.1016/0550-3213(78)90385-1. (1978) (cit. on pp. 38, 40).
144. Lang, T. C. & Läuchli, A. M. Quantum Monte Carlo Simulation of the Chiral Heisenberg Gross-Neveu-Yukawa Phase Transition with a Single Dirac Cone. *Phys. Rev. Lett.* **123**, 137602. doi:10.1103/PhysRevLett.123.137602. (2019) (cit. on p. 38).
145. Schmidt, D. *Three-Dimensional Four-Fermion Theories with Exact Chiral Symmetry on the Lattice* (University of Jena, Jena, 2017). (Cit. on pp. 38, 68).
146. Flore, R. *et al.* Supersymmetric Nonlinear O(3) Sigma Model on the Lattice. *J. High Energ. Phys.* **2012**, 159. doi:10.1007/JHEP11(2012)159. (2012) (cit. on p. 38).
147. Wozar, C. & Wipf, A. Supersymmetry Breaking in Low Dimensional Models. *Ann. Phys.* **327**, 774–807. doi:10.1016/j.aop.2011.11.015. (2012) (cit. on p. 38).
148. Bergner, G. *et al.* Low-Dimensional Supersymmetric Lattice Models. *Ann. Phys.* **323**, 946–988. doi:10.1016/j.aop.2007.06.010. (2008) (cit. on p. 38).
149. Kästner, T. *et al.* Two-Dimensional Wess-Zumino Models at Intermediate Couplings. *Phys. Rev. D* **78**, 095001. doi:10.1103/PhysRevD.78.095001. (2008) (cit. on p. 38).
150. Ginsparg, P. H. & Wilson, K. G. A Remnant of Chiral Symmetry on the Lattice. *Phys. Rev. D* **25**, 2649–2657. doi:10.1103/PhysRevD.25.2649. (1982) (cit. on p. 39).
151. Neuberger, H. Exactly Massless Quarks on the Lattice. *Phys. Lett. B* **417**, 141–144. doi:10.1016/S0370-2693(97)01368-3. (1998) (cit. on p. 39).
152. Bietenholz, W. & Nishimura, J. Ginsparg-Wilson Fermions in Odd Dimensions. *J. High Energy Phys.* **2001**, 015–015. doi:10.1088/1126-6708/2001/07/015. (2001) (cit. on p. 39).
153. Hernández, P., Jansen, K. & Lüscher, M. Locality Properties of Neuberger’s Lattice Dirac Operator. *Nucl. Phys. B* **552**, 363–378. doi:10.1016/S0550-3213(99)00213-8. (1999) (cit. on p. 39).
154. Hands, S., Mesiti, M. & Worthy, J. Critical Behavior in the Single Flavor Thirring Model in 2 + 1 D. *Phys. Rev. D* **102**, 094502. doi:10.1103/PhysRevD.102.094502. (2020) (cit. on pp. 39, 68, 72, 80).
155. Lüscher, M. Exact Chiral Symmetry on the Lattice and the Ginsparg-Wilson Relation. *Phys. Lett. B* **428**, 342–345. doi:10.1016/S0370-2693(98)00423-7. (1998) (cit. on p. 39).
156. Witten, E. Three Lectures On Topological Phases Of Matter. *Riv. Nuovo Cim.* **39**, 313–370. doi:10.1393/ncr/i2016-10125-3. (2016) (cit. on p. 39).
157. Hands, S. & Ostmeyer, J. Spectroscopy in the 2 + 1 D Thirring Model with N = 1 Domain Wall Fermions. *Phys. Rev. D* **107**, 014504. doi:10.1103/PhysRevD.107.014504. (2023) (cit. on pp. 39, 68, 72, 80).
158. Hands, S. Critical Flavor Number in the 2 + 1 D Thirring Model. *Phys. Rev. D* **99**, 034504. doi:10.1103/PhysRevD.99.034504. (2019) (cit. on pp. 39, 68, 72, 80).
159. Gvai, R. V. Chemical Potential on the Lattice. *Phys. Rev. D* **32**, 519–521. doi:10.1103/physrevd.32.519. (1985) (cit. on p. 40).
160. Wichmann, E. H. & Crichton, J. H. Cluster Decomposition Properties of the S Matrix. *Phys. Rev.* **132**, 2788–2799. doi:10.1103/PhysRev.132.2788. (1963) (cit. on pp. 48, 59).
161. De Forcrand, P. & Wenger, U. *New Baryon Matter in the Lattice Gross-Neveu Model 2006*. (Cit. on p. 51).
162. Chandler, D. & Percus, J. K. Introduction to Modern Statistical Mechanics. *Physics Today* **41**, 114–118. doi:10.1063/1.2811680. (1988) (cit. on p. 52).
163. Endrődi, G., Kovács, T. G. & Markó, G. Spontaneous Symmetry Breaking via Inhomogeneities and the Differential Surface Tension. *Phys. Rev. Lett.* **127**, 232002. doi:10.1103/PhysRevLett.127.232002. (2021) (cit. on p. 55).
164. Ciccone, R., Di Pietro, L. & Serone, M. Inhomogeneous Phase of the Chiral Gross-Neveu Model. *Phys. Rev. Lett.* **129**, 071603. doi:10.1103/PhysRevLett.129.071603. (2022) (cit. on p. 56).
165. Abramowitz, M. & Stegun, I. A. *Handbook of Mathematical Functions with Formulas, Graphs, and Mathematical Tables* 10th ed. *Applied Mathematics Series* **55**. 470 pp. (1964) (cit. on p. 64).
166. Furry, W. H. A Symmetry Theorem in the Positron Theory. *Phys. Rev.* **51**, 125–129. doi:10.1103/PhysRev.51.125. (1937) (cit. on p. 67).
167. Gomes, M. *et al.* Gauge Structure, Anomalies, and Mass Generation in a Three-Dimensional Thirring Model. *Phys. Rev. D* **43**, 3516–3523. doi:10.1103/PhysRevD.43.3516. (1991) (cit. on pp. 67, 70, 80).
168. Sugiura, M. Fermion Mass Generation in the D-Dimensional Thirring Model as a Gauge Theory. *Prog. Theo. Phys.* **97**, 311–326. doi:10.1143/PTP.97.311. (1997) (cit. on pp. 70, 80).

169. Hong, D. K. & Park, S. H. Large-  $N$  Analysis of the  $(2 + 1)$ -Dimensional Thirring Model. *Phys. Rev. D* **49**, 5507–5511. doi:10.1103/PhysRevD.49.5507. (1994) (cit. on pp. 70, 80).
170. Christofi, S., Hands, S. & Strouthos, C. Critical Flavor Number in the Three Dimensional Thirring Model. *Phys. Rev. D* **75**, 101701. doi:10.1103/PhysRevD.75.101701. (2007) (cit. on p. 70).
171. Hands, S. & Lucini, B. The Phase Diagram of the Three Dimensional Thirring Model. *Phys. Lett. B* **461**, 263–269. doi:10.1016/S0370-2693(99)00843-6. (1999) (cit. on p. 70).
172. Kondo, K.-I. Thirring Model as a Gauge Theory. *Nucl. Phys. B* **450**, 251–266. doi:10.1016/0550-3213(95)00316-K. (1995) (cit. on p. 73).
173. Banks, T. & Casher, A. Chiral Symmetry Breaking in Confining Theories. *Nucl. Phys. B* **169**, 103–125. doi:10.1016/0550-3213(80)90255-2. (1980) (cit. on p. 73).
174. Leutwyler, H. & Smilga, A. Spectrum of Dirac Operator and Role of Winding Number in QCD. *Phys. Rev. D* **46**, 5607–5632. doi:10.1103/PhysRevD.46.5607. (1992) (cit. on p. 74).
175. Giordano, M. Localised Dirac Eigenmodes, Chiral Symmetry Breaking, and Goldstone’s Theorem at Finite Temperature. *J. Phys. A: Math. Theor.* **54**, 37LT01. doi:10.1088/1751-8121/ac1c3a. (2021) (cit. on p. 74).
176. Chartrand, R. Numerical Differentiation of Noisy, Nonsmooth Data. *ISRN Applied Mathematics* **2011**, 1–11. doi:10.5402/2011/164564. (2011) (cit. on pp. 77, 89).
177. Binder, K. in *Current Physics—Sources and Comments* 79–100 (Elsevier, 1988). doi:10.1016/B978-0-444-87109-1.50012-1. (Cit. on p. 79).
178. Parisi, G. The Theory of Non-Renormalizable Interactions. *Nucl. Phys. B* **100**, 368–388. doi:10.1016/0550-3213(75)90624-0. (1975) (cit. on p. 80).
179. Brauner, T., Filios, G. & Kolešová, H. Anomaly-Induced Inhomogeneous Phase in Quark Matter without the Sign Problem. *Phys. Rev. Lett.* **123**, 012001. doi:10.1103/PhysRevLett.123.012001. (2019) (cit. on p. 84).
180. Khunjua, T. G., Klimenko, K. G. & Zhokhov, R. N. Hartree-Fock Approach to Dynamical Mass Generation in the Generalized  $(2+1)$ -Dimensional Thirring Model. *Phys. Rev. D* **106**, 085002. doi:10.1103/PhysRevD.106.085002. (2022) (cit. on p. 86).
181. Sturniolo, S. *Tvregdiff* version 80c3ce4. 2020. URL: <https://github.com/stur86/tvregdiff> (visited on 2023-09-17) (cit. on p. 89).
182. Athenodorou, A. *et al. Open Science in Lattice Gauge Theory Community* preprint (cit. on p. 99).
183. Gough, B. *GNU Scientific Library Reference Manual - Third Edition* 3rd (Network Theory Ltd., 2009) (cit. on p. 99).
184. Frigo, M. & Johnson, S. The Design and Implementation of FFTW3. *Proc. IEEE* **93**, 216–231. doi:10.1109/JPROC.2004.840301. (2005) (cit. on p. 99).
185. Guennebaud, G., Jacob, B., *et al. Eigen V3* 2010. URL: <http://eigen.tuxfamily.org> (cit. on p. 99).
186. Van Rossum, G. & de Boer, J. Interactively Testing Remote Servers Using the Python Programming Language. *CWI Quarterly* **4**, 283–304. (1991) (cit. on p. 99).
187. Hunter, J. D. Matplotlib: A 2D Graphics Environment. *Computing in Science Engineering* **9**, 90–95. doi:10.1109/MCSE.2007.55 (2007) (cit. on p. 99).
188. Johansson, F. *et al. Mpmath: A Python Library for Arbitrary-Precision Floating-Point Arithmetic (Version 1.2.1)* manual (2013) (cit. on p. 99).
189. Van der Walt, S., Colbert, S. C. & Varoquaux, G. The NumPy Array: A Structure for Efficient Numerical Computation. *Computing in Science Engineering* **13**, 22–30. doi:10.1109/MCSE.2011.37 (2011) (cit. on p. 99).
190. McKinney, W. Data Structures for Statistical Computing in Python. *Proceedings of the 9th Python in Science Conference*, 51–56 (2010) (cit. on p. 99).
191. Seabold, S. & Perktold, J. *Statsmodels: Econometric and Statistical Modeling with Python* in. Python in Science Conference (Austin, Texas, 2010), 92–96. doi:10.25080/Majora-92bf1922-011. (Cit. on p. 99).

# Danksagungen

An dieser Stelle geht es nun zu Ende und es ist Zeit, Dank zu sagen. Denn so sehr das unmittelbare Verfassen dieser Arbeit eine Einzelleistung war, so fand sie doch zu keiner Zeit als punktförmige, masselose Bewegung im reibungsfreien Vakuum statt – so gerne wir in der Physik diese Näherungen auch machen.

Mein erster und größter Dank gilt natürlich meiner Familie, meiner geliebten Ehefrau und meiner wunderbaren Tochter, die mich nach durchgearbeiteten Nächten ertragen haben, mir den Rücken freigehalten haben und gleichzeitig immer da waren, um mir im richtigen Moment ein Lächeln auf das Gesicht zu zaubern. Aber natürlich auch meinen Eltern, die mich zu dem gemacht haben, der ich bin, und mich von Anfang bis Ende unterstützt haben. Ohne eure Hilfe wäre diese Arbeit jetzt nicht in der Form, die sie erlangt hat, geschweige denn überhaupt jemals entstanden.

Aber natürlich ist dies vorrangig eine wissenschaftliche Schrift, deren Inhalt in wissenschaftlicher Zusammenarbeit mit vielen unglaublich klugen und netten Menschen entstanden ist. Zu vorderst möchte ich natürlich Herrn Professor Andreas Wipf danken. Für alles, was Sie mich gelehrt haben, für weise Worte und grundlegende Erkenntnisse, aber auch klitzekleine Hinweise, ohne die ich wahrscheinlich viele Tage und Wochen (mehr) gebraucht hätte, um Vorzeichen- oder Denkfehler zu finden. Für Ihren Einsatz und die finanzielle Unterstützung, die Sie für alle meine Pläne aufbringen konnten. Und natürlich für Ihre Geduld mit meiner etwas verspäteten Abgabe.

Weiterhin natürlich Björn Wellegehausen, dessen Code wahrscheinlich alleine für mein liches Haar verantwortlich ist. Trotzdem möchte ich mir nicht vorstellen, wie viel langsamer und erfolgsärmer wir vorangekommen wären, wenn wir dein Verständnis für Physik oder Software hätten missen müssen. Zusammen mit Marc Steinhauser und Michael Mandl danke ich dir natürlich auch für den vielen Spaß, den ich bei der Arbeit mit euch hatte. An letzteren geht ebenfalls mein besonderer Dank für unsere erfolgreiche Zusammenarbeit und insbesondere deine hervorragende Literaturkenntnis. Außerdem, zusammen mit Marc, habt ihr diese Arbeit beim Korrekturlesen gehörig zerpflückt und es trotzdem geschafft, dass ich beim Einarbeiten eurer Kommentare zumeist ein Lächeln auf den Lippen hatte.

Auch an alle meine anderen wissenschaftlichen Kontakte geht mein Dank für all die Eindrücke und Erkenntnisse, die ich während dieser Zeit erlangen durfte. Den "Frankfurtern", Marc Wagner und Laurin Pannullo, danke ich für die gute Zusammenarbeit und die Gastfreundschaft ebenso wie für aus- und ergiebige Diskussionen zusammen mit Marc Winstel. Ed Bennett danke ich für das herzliche Willkommen in Swansea, deine offene, verständnisvolle und verständnisstiftende Art und die neuen Perspektiven, die du mir auf unsere wissenschaftliche Arbeit eröffnet hast. Vor allem aber für deine Kulanz in Hinblick auf Arbeitszeit, die in diese Dissertationsschrift fließen durfte. Ich bin zuversichtlich, dass mich deine Deutschkenntnisse einmal mehr überraschen werden und diese Botschaft zu dir durchdringen wird.

Abschließend geht mein Dank an all die Leute drumherum, die mir die Arbeit und das Leben in dieser Phase etwas angenehmer und einfacher gemacht haben: Die Physiker-Clique, die Mitglieder des Graduiertenkollegs – insbesondere Holger Gies –, Lisann Schmidt und Katrin Kanter. Ich habe mich bemüht, aber ich werde sicherlich jemanden völlig zu unrecht in dieser Liste vergessen haben. Auch an dich, nicht-genannte Person, geht mein Dank, denn es gibt natürlich noch viel mehr Personen, die große oder kleine Sachen im Umfeld dieser Arbeit geleistet haben.

I have been supported by the Deutsche Forschungsgemeinschaft (DFG) under Grant No. 406116891 within the Research Training Group RTG 2522/1 as an associated member as well as by the UKRI Science and Technology Facilities Council (STFC) Research Software Engineering Fellowship EP/V052489/1 and by the Supercomputing Wales project, which is part-funded by the European Regional Development Fund (ERDF) via Welsh Government. The simulations were performed on resources of the Friedrich Schiller University in Jena supported in part by the DFG Grants INST 275/334-1 FUGG and INST 275/363-1 FUGG. Calculations on the GOETHE-HLR and on the FUCHS-CSC high-performance computers of the Frankfurt University were conducted for this research.

# Ehrenwörtliche Erklärung

gemäß § 5 Satz 2 Nr. 3 PromO

Hiermit erkläre ich ehrenwörtlich,

1. dass mir die geltende Promotionsordnung bekannt ist;
2. dass ich die Dissertation selbst angefertigt habe, keine Textabschnitte eines Dritten oder eigener Prüfungsarbeiten ohne Kennzeichnung übernommen und alle von mir benutzten Hilfsmittel, persönlichen Mitteilungen und Quellen in meiner Arbeit angegeben habe;
3. dass bei der Auswahl und Auswertung folgenden Materials mich die nachstehend aufgeführten Personen in der jeweils beschriebenen Weise unterstützt haben:
  - Prof. Andreas Wipf als betreuender Hochschullehrer
  - Dr. Björn Wellegehausen durch die Bereitstellung des Simulationscodes
  - alle Autoren meiner bisherigen Veröffentlichungen [37, 38, 42, 43, 64–69, 87, 96] im üblichen Sinne einer wissenschaftlichen Kollaboration
4. dass die Hilfe einer kommerziellen Promotionsvermittlerin/eines kommerziellen Promotionsvermittlers nicht in Anspruch genommen wurde und dass Dritte weder unmittelbar noch mittelbar geldwerte Leistungen für Arbeiten erhalten haben, die im Zusammenhang mit dem Inhalt der vorgelegten Dissertation stehen;
5. dass die Dissertation noch nicht als Prüfungsarbeit für eine staatliche oder andere wissenschaftliche Prüfung eingereicht wurde;
6. dass eine gleiche, eine in wesentlichen Teilen ähnliche oder eine andere Abhandlung bei einer anderen Hochschule als Dissertation nicht eingereicht wurde.

---

Ort und Datum

---

Julian Johannes Lenz